

MEMS resonators in dissipative media

Towards the detection of biomolecules

Guilherme Ricardo Mendes da Silva Barreto de Figueiredo

Thesis to obtain the Master of Science Degree in

Bioengineering and Nanosystems

Supervisors: Dr. João Pedro Estrela Rodrigues Conde; Dr. Virginia Chu

Examination Committee

Chairperson: Prof. Luís Joaquim Pina da Fonseca

Supervisor: Dr. João Pedro Estrela Rodrigues Conde

Member of the Committee: Prof. Luís Humberto Viseu Melo

November 2014

Acknowledgements

I would like to acknowledge my advisor Prof. João Pedro Conde for all of the support, guidance and motivation necessary for me to successfully complete this thesis. His will to gladly share his knowledge with others should serve as an example for everyone. A special thanks to my co-advisor Dr. Virginia Chu for always being available to help, providing fast and effective solutions.

To all of my colleagues at INESC-MN I thank for all of the help given to me, in moments when I was a bit lost. I wish you all an immense success.

I acknowledge my mentor João Mouro for everything I learned from him. His expertise in several situations helped me evolve and he was a major help to successfully accomplish the desired results. Thank you.

I am thankful to all of the INESC-MN staff for all of the assistance during the fabrication of the devices used in this work. I could not have done it without them.

I am grateful to my girlfriend for all of her support and for always being there for me. Thank you for all of the nights that you did not sleep just to be on the couch closer to me while I wrote this work. I love you.

I thank my friends for all of their friendship throughout these years, and for helping me in this work when I had doubts in their fields of expertise. You guys are the best!

At last, I thank my mother and my grandparents for their unconditional love, for supporting me and for making me who I am.

Abstract

MEMS resonators can operate as mass sensors for biological applications due to their label free, small size and low power consumption properties. The principle is based on the addition of analyte molecules that bind to the surface of the structures, inducing a resonance frequency shift. MEMS should be measurable at atmospheric pressure and liquid media to enable the detection of biomolecules.

For this work several hydrogenated amorphous silicon microbridges were fabricated on glass substrates at temperatures below 200 °C. The structures were electrostatically actuated and optically measured at $\sim 10^{-2}$ Torr, with resonance frequencies in the range of MHz and quality factors (Q-factors) of ~ 1000 , for structures between 40 μm and 200 μm in length.

To assess if MEMS devices are suitable for biological detection, several dissipation mechanisms were tested. To verify the hypothesis that molecules at the surface of the structures can affect the Q-factors, *annealing* temperatures up to 250 °C were applied. It was demonstrated that the Q-factors improved on all of the samples.

The structures were also measured at atmospheric pressure and immersed in DI water. These media considerably affects the operability of the structures, which is confirmed by the large decrease of the Q-factors, where the highest value in liquid medium is 17.

Keywords: MEMS, Resonance Frequency, Quality Factor, *Annealing*, Dissipative Media, DI water

Resumo

Devido ao seu tamanho reduzido, baixo consumo e capacidade de detecção sem recorrer a marcadores, ressoadores MEMS podem ser usados como sensores de massa para várias aplicações biológicas. Para tal, as estruturas são funcionalizadas para detectar moléculas que causam um desvio mensurável na frequência de ressonância. De modo a possibilitarem a detecção de biomoléculas, os ressoadores MEMS devem funcionar em meios líquidos e a pressão atmosférica.

Micropontes de silício amorfo hidrogenado foram fabricadas em substratos de vidro a temperaturas inferiores a 200 °C. Estas estruturas foram actuadas electrostaticamente e medidas opticamente a uma pressão de $\sim 10^{-2}$ Torr. As suas frequências de ressonância são na ordem dos MHz e os factores de qualidade ~ 1000 , para estruturas com comprimentos entre 40 μm e 200 μm .

Vários mecanismos de dissipação foram testados de modo a verificar se os ressoadores MEMS são viáveis para detecção biológica. Os factores de qualidade podem ser afectados pela presença de moléculas na superfície das estruturas. Para testar esta hipótese sujeitaram-se os ressoadores MEMS a aumentos de temperatura até 250 °C. Verificou-se que ao longo dos passos de *annealing* os factores de qualidade melhoraram em todas as amostras.

As estruturas foram também medidas a pressão atmosférica e em água desionizada, sendo que estes meios afectam consideravelmente o funcionamento das micropontes, confirmado pela diminuição dos factores de qualidade onde o maior valor é de 17 para o meio aquoso.

Palavras Chave: MEMS, Frequência de Ressonância, Factor de Qualidade, *Annealing*, Meios Dissipativos, Água Desionizada

Table of Contents

Acknowledgements	i
Abstract.....	ii
Resumo	iii
List of abbreviations.....	vi
List of Figures	vii
List of Graphics.....	viii
List of Tables	x
Chapter 1 – Introduction	1
1.1. Overview.....	1
1.2. Microelectromechanical Systems (MEMS).....	2
1.3. Amorphous Silicon (a-Si) MEMS	6
1.4. MEMS Applications	9
Chapter 2 – Methods	11
2.1. Microfabrication	11
2.2. Characterization	17
Chapter 3 – Experimental Results.....	23
3.1. Vacuum Characterization	23
3.2. Vibrational Modes	26
3.3. Voltage Bias Sweep	29
Chapter 4 – Annealing Measurements.....	37
4.1. Introduction	37
4.2. Annealing Characterization	37
4.3. Annealing Results.....	38
4.4. Aging of MEMS.....	47
Chapter 5 – MEMS Dissipation in air	50
5.1. Introduction	50
5.2. Pressure Characterization	50
5.3. Squeeze Film Damping	58
Chapter 6 – MEMS Dissipation in water.....	60
6.1. Introduction	60

6.2. Experimental Setup	60
6.3. Water Characterization	66
Chapter 7 – Conclusion	73
7.1. Main Results	73
7.2. Future Perspectives	74
Appendix A	75
A. Runsheet Example	75
Bibliography	82

List of abbreviations

AC	Alternating Current
AFM	Atomic Force Microscopy
Al	Aluminum
a-Si	Amorphous Silicon
a-Si:H	Hydrogenated Amorphous Silicon
Co	Cobalt
DC	Direct Current
DI water	Deionized Water
DWL	Direct Write Laser
Fe	Iron
Fres	Resonance Frequency
H₂	Hydrogen
IC	Integrated Circuits
IPA	Isopropyl alcohol
LCD	Liquid Crystal Displays
MEMS	Microelectromechanical Systems
Ni	Nickel
P_c	Critical Pressure
PDMS	Polydimethylsiloxane
PECVD	Plasma Enhanced Chemical Vapor Deposition
PH₃	Phosphine
PVC	Polyvinyl chloride
PZT	Lead Zirconate Titanate
Q-factor	Quality Factor
RF-PECVD	Radio Frequency Plasma Enhanced Chemical Vapor Deposition
RIE	Reactive Ion Etch
SEM	Scanning Electron Microscope
Si	Silicon
SiC	Silicon Carbide
SiH₄	Silane
TiW	Titanium Tungsten

List of Figures

Figure 1 - MEMS as a Microactuator [5].....	4
Figure 2 - MEMS as a Microsensor [5].....	4
Figure 3 - SEM micrograph of disk plate resonator [6].....	5
Figure 4 - SEM micrograph of a cantilever [12].....	5
Figure 5 - SEM micrograph of a fixed bridge.....	6
Figure 6 – Atomic structure model of a-Si:H illustrating the bonding disorder and the presence of hydrogen. Large disks represent Si atoms and small disks are hydrogen [15].....	7
Figure 7 - PECVD Machine	8
Figure 8 - SEM micrographs showing visual effects of stress in several structures [12]	9
Figure 9 - Micrograph of single gate die after RIE	12
Figure 10 - Micrograph of die with two (left) and four (right) gates	12
Figure 11 - Micrographs of different gates covered with an Al layer	13
Figure 12 - Plasma Energy Source during a deposition process	14
Figure 13- Single gate structures after last lithography and RIE.....	15
Figure 14 - two and four gates structures after last lithography and RIE	15
Figure 15 - Cutting of the dies in Disco DAD 321	16
Figure 16 - Micrographs of several structures after their release.....	17
Figure 17 - Optical setup vacuum chamber	18
Figure 18 - Spectrum Analyzer.....	18
Figure 19 - Schematic diagram of the measurement setup in vacuum. Measuring the deviation of the reflected laser beam with a photodetector monitors the resulting vibration [31]	23
Figure 20 - Fundamental and Harmonics Modes [31].....	26
Figure 21 - Frequency conditions for cantilever, supported and fixed-fixed bridges with different boundary conditions [31]	27
Figure 22 – Memmert heating oven and chip inside oven	38
Figure 23 - Squeeze film air damping; a) cross-sectional view; b) the damping pressure [46]	58
Figure 24 - Wire bonded devices protected with Silicone	61
Figure 25 - Schematic illustration of the resonance frequency measurements in DI water [1].....	62
Figure 26 - DI water drop trapped on Silicone well	62
Figure 27 - Example of mask with the main structures close to the edges of the die	63
Figure 28 - Laser deflection due to proximity of the Silicone wall to the structures	64
Figure 29 - Example of mask with the main structures closer to the center of the die	65

List of Graphics

Graphic 1 - Resonance Frequency as a function of Length. $E = 150 \text{ GPa}$; $\rho = 2330 \text{ Kg/m}^3$; Pressure $\approx 10^{-2} \text{ Torr}$	24
Graphic 2 - Q-factor as a function of Length. $E = 150 \text{ GPa}$; $\rho = 2330 \text{ Kg/m}^3$; Pressure $\approx 10^{-2} \text{ Torr}$	25
Graphic 3 - Resonance frequencies and Q-factors extracted from the Lorentzian curve adjusted to the peaks. a) $150 \mu\text{m}$ fixed bridge; b) $90 \mu\text{m}$ fixed bridge; c) $80 \mu\text{m}$ fixed bridge. $E = 150 \text{ GPa}$; $\rho = 2330 \text{ Kg/m}^3$; Pressure $\approx 10^{-2} \text{ Torr}$	26
Graphic 4 - Resonance Frequency as a function of Length. $E = 150 \text{ GPa}$; $\rho = 2330 \text{ Kg/m}^3$; Pressure $\approx 10^{-2} \text{ Torr}$	28
Graphic 5 – Q-Factor as a Function of Length. $E = 150 \text{ GPa}$; $\rho = 2330 \text{ Kg/m}^3$; Pressure $\approx 10^{-2} \text{ Torr}$	29
Graphic 6 – Electrical softening representation on an $80 \mu\text{m}$ bridge. $E = 150 \text{ GPa}$; $\rho = 2330 \text{ Kg/m}^3$; Pressure $\approx 10^{-2} \text{ Torr}$	30
Graphic 7 – Mechanical stiffening representation on a $120 \mu\text{m}$ bridge. $E = 150 \text{ GPa}$; $\rho = 2330 \text{ Kg/m}^3$; Pressure $\approx 10^{-2} \text{ Torr}$	31
Graphic 8 – Intermediate effect representation on a $150 \mu\text{m}$ bridge. $E = 150 \text{ GPa}$; $\rho = 2330 \text{ Kg/m}^3$; Pressure $\approx 10^{-2} \text{ Torr}$	32
Graphic 9 - Comparison of vibrational modes with applied voltage, of a $120 \mu\text{m}$ bridge. $E = 150 \text{ GPa}$; $\rho = 2330 \text{ Kg/m}^3$; Pressure $\approx 10^{-2} \text{ Torr}$	33
Graphic 10 - Peak Amplitude as a function of Voltage. a) $80 \mu\text{m}$ bridge; b) $120 \mu\text{m}$ bridge; c) $150 \mu\text{m}$ bridge	34
Graphic 11 - Peak Position as a function of Voltage. a) $80 \mu\text{m}$ bridge; b) $120 \mu\text{m}$ bridge; c) $150 \mu\text{m}$ bridge	35
Graphic 12 - Resonance Frequency as a function of a) Temperature and b) Length	39
Graphic 13 - Quality Factor as a Function of the Annealing Temperature	39
Graphic 14 - Resonance Peaks affected by Temperature for a $60 \mu\text{m}$ bridge	40
Graphic 15 - Annealing Temperature comparison of the Quality Factor as a function of Length	41
Graphic 16 - Resonance Frequency as a Function of temperature for the first, third and fifth vibrational modes	42
Graphic 17 - Quality Factor as a function of Temperature for the first, third and fifth vibrational modes	43
Graphic 18 - Annealing Temperature comparison of the Quality Factor as a function of Length for the fundamental mode	44
Graphic 19 - Annealing Temperature comparison of the Quality Factor as a function of Length for the third vibrational mode	45
Graphic 20 - Annealing Temperature comparison of the Quality Factor as a function of Length for the fifth vibrational mode	46
Graphic 21 - Demonstration of the Resonance Frequency as a function of the Length of the structures for a period of around 5 months	48
Graphic 22 - Demonstration of the Quality Factor as a function of the Length of the structures for a period of around 5 months	49

Graphic 23 - Resonance Frequency as a function of Pressure. $E = 150 \text{ GPa}$; $\rho = 2330 \text{ Kg/m}^3$	52
Graphic 24 - Quality Factor as a function of Pressure. $E = 150 \text{ GPa}$; $\rho = 2330 \text{ Kg/m}^3$	53
Graphic 25 - Quality Factors measured in atmospheric pressure as a function of their Resonance Frequency.....	55
Graphic 26 - Quality Factors measured in air as a function of the Quality Factors measured in vacuum	56
Graphic 27 - Critical Pressures as a function of the Resonance Frequency for all of the vibrational modes.....	57
Graphic 28 - Example of Resonance Frequency shifts as a function of Pressure with squeeze film damping [6] (left) and Resonance Frequency as a function of Pressure for the measured structures with no squeeze film damping (right).....	59
Graphic 29 - Resonance Frequency as a Function of the Length of the structures for the different dissipative media	67
Graphic 30 - Quality Factor as a Function of the Length of the structures for the different dissipative media	68
Graphic 31 - Representation of the Frequency peaks of a $150 \text{ }\mu\text{m}$ bridge, at different dissipative media	69
Graphic 32 - Representation of the Quality Factors as a function of the length of the structures, in an aqueous environment, with the correspondent frequency peaks	70
Graphic 33 - Representation of the Resonance Peak of an $80 \text{ }\mu\text{m}$ bridge in Vacuum	71
Graphic 34 - Representation of the Resonance Peak of an $80 \text{ }\mu\text{m}$ bridge in Water	72

List of Tables

Table 1 - Dimensions and masses in perspective [4].....	2
Table 2 - Common transduction mechanisms used in MEMS [9]	3
Table 3 - Correspondence between features of the atomic structure and the resulting electronic properties [17].....	7
Table 4 - Market Industries and Applications for MEMS [5] [8]	10
Table 5 - Liquids used for release of the structures, immersion time and surface tension	16
Table 6 - Information obtainable by using high-speed visualization [27]	22
Table 7 - Experimental ratio values	28

Chapter 1 – Introduction

1.1. Overview

The growing need to develop new point-of-care portable devices that can detect specific biomolecules in liquid media, led to an increase in the investigations of Microelectromechanical Systems (MEMS), focused on medical and public health applications. In order to create sensors to be used directly with body fluids for these fields, more compact, low power consumption and label-free devices that can also be integrated with electronics should be designed. For this, MEMS sensors are in the lead of systems with those built-in properties, which can be integrated for the use in the applications mentioned above, with added advantages of providing rapid measurement times and good performances.

For biosensing, it is imperative to have quantitative, real-time and *in situ* measurements since many biological reactions and biomolecules need aqueous environments in order to maintain the majority of their functionalities [1].

Even though the integration of MEMS in miniaturized systems for biodetection is appealing, it is not free of some major drawbacks that for sure affect the structures performance. The ones that have the biggest impact are the damping effects of liquid environments, which cause considerable quality factor (Q-factor) reduction meaning that liquid-phase measurements become a complex challenge [2]. This reduction of Q-factor can be quite extensive, depending on the properties of the structures, and can range from 1000-10000 down to 1-10, also accompanied by a loss of sensitivity. One of the goals of this work is to bypass this reduction since the minimal detectable mass for this type of sensors will be dependent on the Q-factor of the structures.

Despite the current existence of methods for liquid-phase measurements involving measuring samples in air, after treating the structures with target molecules and drying them, the appeal for point-of-care applications diminishes, due to several issues that present themselves as hard to solve, such as the loss of ability to work with microprobes, decrease of affinity, stress, or even wetting issues or stiffness caused by surface adhesion [2].

It is not possible to detect some type of biomolecule simply by adding a droplet with the analyte of study to a MEMS structure. There is a need to functionalize the surface of the structures that are going to be used as sensors, thus allowing the target molecule to bind to the structures surface. These interactions induce slight shifts in the resonance frequency of the structures that can be explained by mass loading.

In order to use MEMS devices for biodetection, one should increase its detection sensitivity, which can be achieved by playing with several parameters and characteristics of the structures including the optimization of the damping effects that can be done by operating the devices at higher order vibrational modes, the selection of specific materials that induce higher Q-factors, the reduction of the structures thickness during the microfabrication process, and also the selection of a more suitable geometry for both the structure itself or even the actuating gates [2] [3].

During this work, several measurements in different media such as vacuum, air and DI water were performed, along with pressure experiments to detect the critical pressures at which Q-factor

values begin to decrease and annealing experiments in an attempt to increase the initial Q-factors of the structures.

1.2. Microelectromechanical Systems (MEMS)

MEMS are systems containing micro scale structures that can be fabricated containing several components with a range of 1 to 100 μm (micrometers) in size. As the name implies, these systems are composed by an electric component in a form of an external power supply used for both actuation and detection. The term mechanical comes from its ability to perform vertical or lateral mechanical motions or actions, depending on the type of structure, and how it is being actuated.

Since the 1960's, researchers were able to complement non-lithographic processes with new advances in lithographic processes such as surface micromachining, in order to fabricate a wide variety of miniaturized systems, including the now fairly common Silicon (Si) based devices or chemical and biological sensors and actuators [4].

Besides the applications that are the focus of this work, there is also a vast range of activity fields in which MEMS can be useful, for instance automotive, aerospace, construction, telecommunications and consumer products industries [5]. The reasons why MEMS have the ability to be useful in so many areas of expertise relates to the fact that it is possible to produce multiple devices at the same time, their miniature size, and the fact that many of the manufacturing techniques are low-cost. It was this reduction in costs that drove the introduction of MEMS in such a diversity of industries [4].

Dimensions in Perspective	
NEMS characteristic length	<1,000 nm
MEMS characteristic length	< 1mm and > 1 μm
Individual atoms	Typically fraction of a nm in diameter
DNA molecules	~ 2,5 nm wide
Molecular gear	~ 50 nm
Biological cells	Thousands of nm in diameter
Human hair	~ 75,000 nm in diameter
Masses in Perspective	
NEMS built with cross sections of about 10 nm	As low as 10 ⁻²⁰ N
Micro machine silicon structure	As low as 1 nN
Water droplet	~ 10 μN
Eyelash	~ 100 nN

Table 1 - Dimensions and masses in perspective [4]

It is well known that small components enhance the capabilities of these devices, so there is a great interest in increasing miniaturization, since small systems tend to move faster due to its smaller mass, thus lowering the mechanical inertia of the whole structure. By reducing the dimensions the

response to changes of thermal condition is faster, which turns the systems more effective [5]. It is also documented that some of the MEMS properties such as structure dimensions, electrical and mechanical properties of the structural materials, level of humidity, temperature, and pressure can influence the dynamic response of these devices [6].

The growing injection of MEMS onto new and diverse fields can also be related to the inclusion of novel materials. Though Si is widely used it can also have some limitations that can be avoided by the selection of different materials, since their specific properties can be able to expand the functionalities of microfabricated devices. This can expand the range of areas for future applications as well as new fabrication techniques. Bulk substrates and thin films are the most common top-down approaches used in the fabrication of these devices, but with the incorporation of new materials bottom-up approaches can also become conventional techniques for the fabrication of structures that cannot be made using top-down approaches [4].

Due to the electronic and/or mechanical capabilities of MEMS, they can act as actuators, sensors, or even passive structures [7]. The role of actuators and sensors can be compared to the human body if considered that an actuator is the extensions of our hands and fingers while a sensor is comparable to our faculties such as vision, smell, touch or hearing [8]. One can define an actuator as a mechanical apparatus used to move and control something. Since they are designed to induce motion driven by a power source, it is possible to identify various means used for that induction. Some of those are:

- Thermal Forces
- Shape Memory Alloys
- Piezoelectric Crystals
- Electrostatic Forces

The most common method to induce motion to actuators is through electrostatic forces via an input voltage from a direct-current (DC) source. A transduction unit is typically present in a MEMS actuator, to convert the energy input. It consists on a physical effect that converts one form of energy such as electrical, magnetic, mechanical, thermal, chemical or radiative, into a different form [9].

Table 2 demonstrates the most typical transduction mechanisms.

To / From	Electrical	Magnetic	Mechanical	Thermal	Chemical	Radiative
Electrical		Ampere's Law	Electrostatics, Electrophoresis	Resistive Heating	Electrolysis, Ionization	EM transmission
Magnetic	Hall Effect, Mag. Resistance		Magnetostatics, Magnetostriction	Eddy Currents, Hysteretic Loss	Magnetic Separation	Magneto-optics
Mechanical	Variable Cap. Piezoresistance Piezoelectricity	Magnetostriction		Friction	Phase Change	Tribo-luminescence
Thermal	Thermoelectric	Curie Point	Thermal Expansion		Reaction Rate Ignition	Thermal Radiation
Chemical	Electrochemical Potential	Chemomagnetic	Phase Change	Combustion		Chemo-luminescence
Radiative	Photoconductor, EM Receiving	Magneto-optics	Radiation Hardening	Photothermal	Photochemical	

Table 2 - Common transduction mechanisms used in MEMS [9]

That unit functions as the actuating element. Figure 1 shows the relation between the elements of a MEMS actuator.

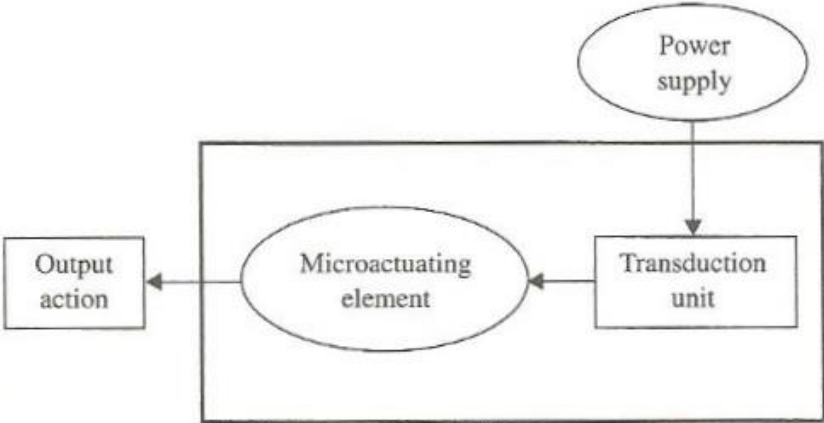


Figure 1 - MEMS as a Microactuator [5]

It is possible to incorporate MEMS technology into sensing systems in order to improve its properties such as size, cost and performance. It is for this reason that the majority of MEMS developed to this day are microsensors [9]. The most common sensors used nowadays include:

- Biosensors
- Chemical Sensors
- Optical Sensors
- Thermal Sensors
- Pressure Sensors
- Mass Sensors

Sensors are highly sensitive and accurate, and allow the testing of small amounts of samples. They are able to sense both presence and intensity of any given quantity, that can be biological, chemical or physical, for instance temperature, mass, light emission, depending on the function that the device is made for [5]. Figure 2 shows the relation between the elements of a MEMS sensor.

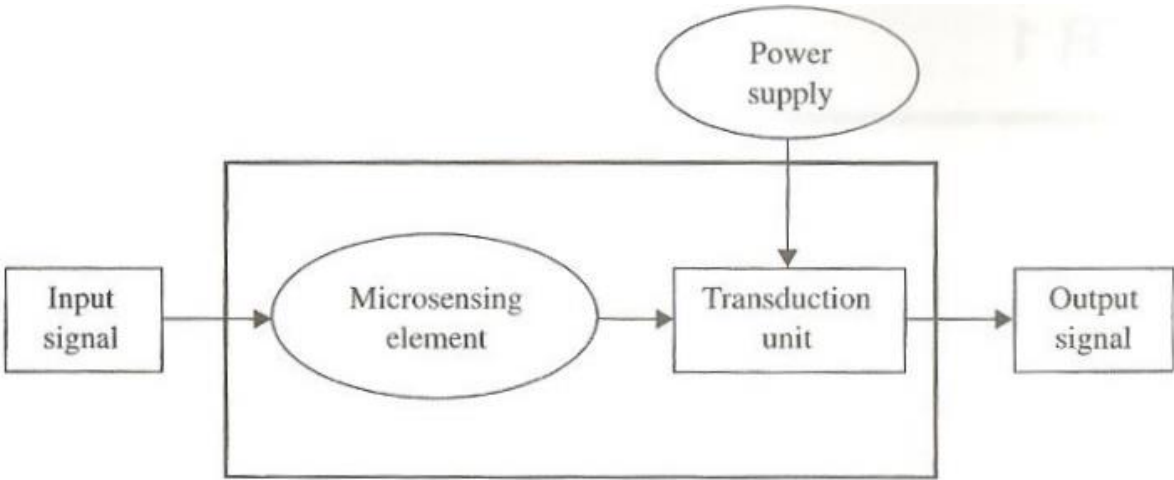


Figure 2 - MEMS as a Microsensor [5]

Microsensors are the most widely used MEMS devices nowadays. One could define sensor as a structure able to convert one energy type into another, which provides the user an energy output in response to a measurable input. Microsensors are the main elements in applications using bioMEMS. Biomedical Sensors and Biosensors are the two main types of sensors used in this field. Biomedical Sensors are used to detect biological substances whereas Biosensors include any measuring device containing a biological element.

To integrate these systems for biological applications it is necessary to address some technical issues, including their functionality, adaptability, compatibility and controllability [5].

MEMS structures can have several types of designs, depending on what they are used for. Some of those designs include disk plates (Figure 3), cantilevers (Figure 4) or bridges (Figure 5), and can be used as accelerometers, pressure, gas and mass sensors, or temperature sensors [6] [7] [10] [11]. Several structures with different aspects and lengths can be design in the same die and several dies can be fabricated on the same wafer. The total number of final structures depends mainly on the initial design of the masks, and the size of the wafers used for the process.

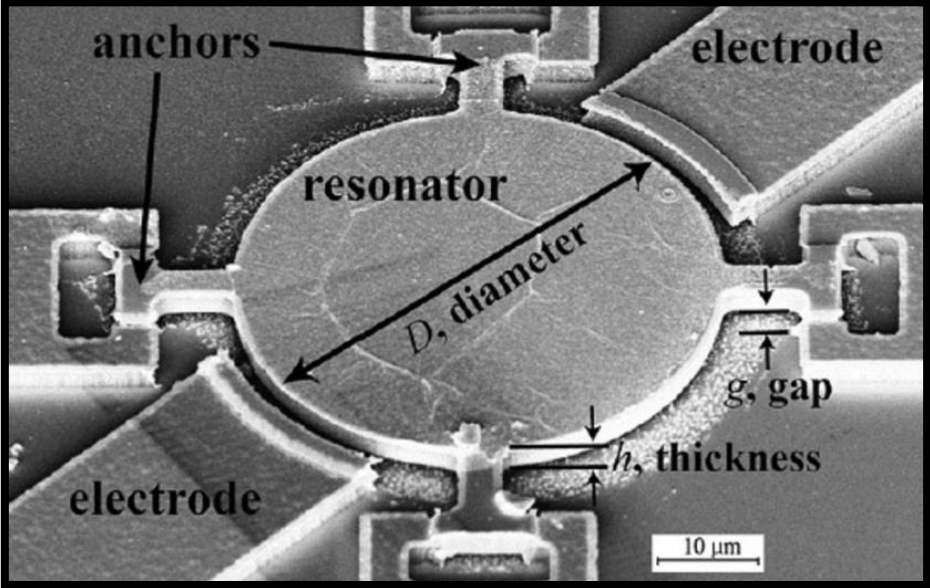


Figure 3 - SEM micrograph of disk plate resonator [6]

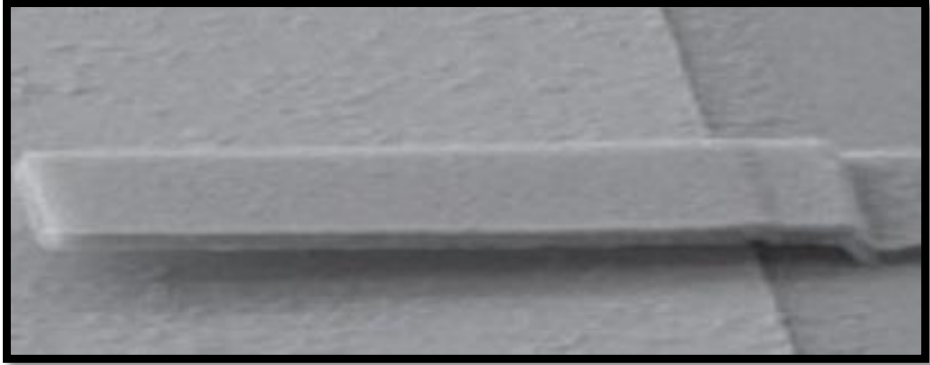


Figure 4 - SEM micrograph of a cantilever [12]

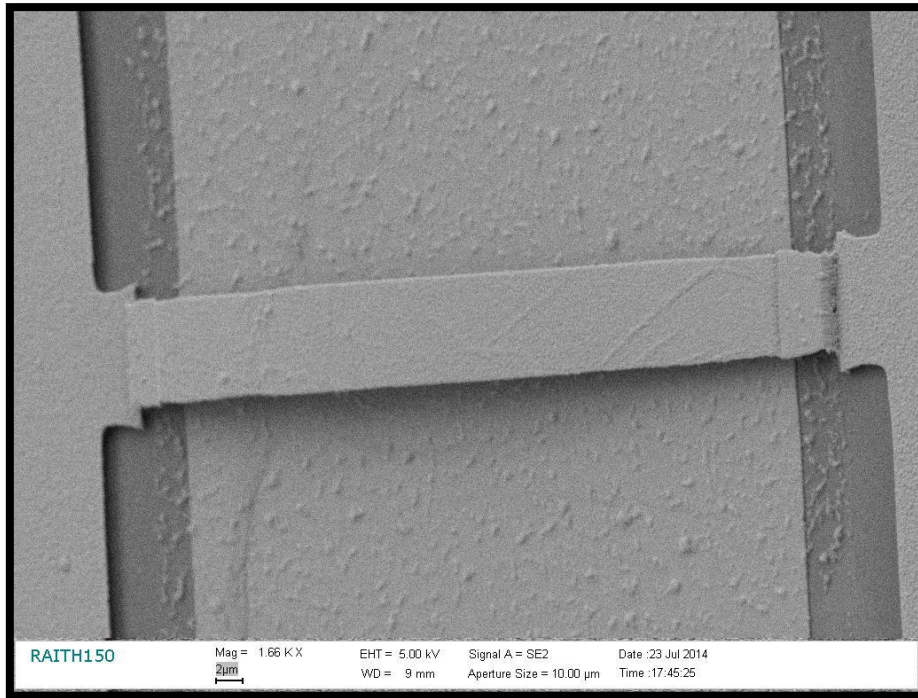


Figure 5 - SEM micrograph of a fixed bridge

The way that these structures can be used for biodetection is simple, theoretically speaking. When actuated they present a certain resonance frequency (F_{res}). If a given biomolecule is positioned on top of the structure, a shift in the F_{res} will indicate the presence of such molecule. The range of that shift can give information about its properties, since it is directly proportional to the mass of the biomolecules of study [1].

1.3. Amorphous Silicon (a-Si) MEMS

The large number of different materials used for the design and fabrication of complex MEMS devices boosted the success of MEMS as a state of the art technology. Due to the reduced scale of these devices, it is possible to experiment with materials that typically are not suitable for large scale devices, while profiting from some scale dependent properties such as yield or fracture strength [13].

Some of the materials, as well as microfabrication techniques used in the production of MEMS came from the integrated circuits (IC) industry such as Silicon and some of its derivatives including silicon dioxide and silicon nitride, and aluminum. Other materials used for MEMS production are piezoelectric films (PZT), magnetic films (Ni, Fe, Co), high-temperature materials (SiC) aluminum alloys, stainless steel, platinum, gold, sheet glass, plastics (PVC and PDMS) [9] and diamond.

Amorphous Silicon can be defined as Silicon that lacks a preferred crystalline orientation, which usually consists of fine grains each measuring a few nanometers [14]. The initial applications for amorphous silicon were photovoltaic solar cells in the early 1980's [15].

Hydrogenated amorphous silicon (a-Si:H) is nowadays considered an omnipresent materials system in large-area electronics used in a large variety of applications, that can range from Liquid-

crystal displays (LCD) to medical imaging [16]. At first, it was considered that a-Si:H was a derivative of crystalline silicon, where the disorder of the atomic structure distorted the electronic properties of the material. The increase of the interest in a-Si:H came from the clearance of this idea. It is now known that the disorder of the atomic structure combined with the presence of hydrogen result in localized band tail states that are characteristic of amorphous materials, which positively affect the optical, transport and recombination properties. The incorporation of hydrogen in the atomic structure provides particular defect, doping and metastability effects.

Structure		Electronic Properties
Bonding Disorder	➔	Band tails, localization, scattering
Structural Defects	➔	Electronic states in the band gap
Alternative Bonding Configurations	➔	Electronically induced metastable states

Table 3 - Correspondence between features of the atomic structure and the resulting electronic properties [17]

A-Si without the presence of the hydrogen molecules tends to have a very high defect density which disables several handy characteristics present on a useful semiconductor such as doping or photoconductivity. Due to this unhydrogenation of a-Si in the past, electronic measurements were focused only on the investigation of conduction through the defect states.

The disorder of the atomic structure (Figure 6) mentioned before, can be considered as one of the key features that differentiates amorphous from crystalline materials and it is more meaningful in semiconductors due to importance of the periodicity of the atomic structure in the theory of crystalline semiconductors [17].

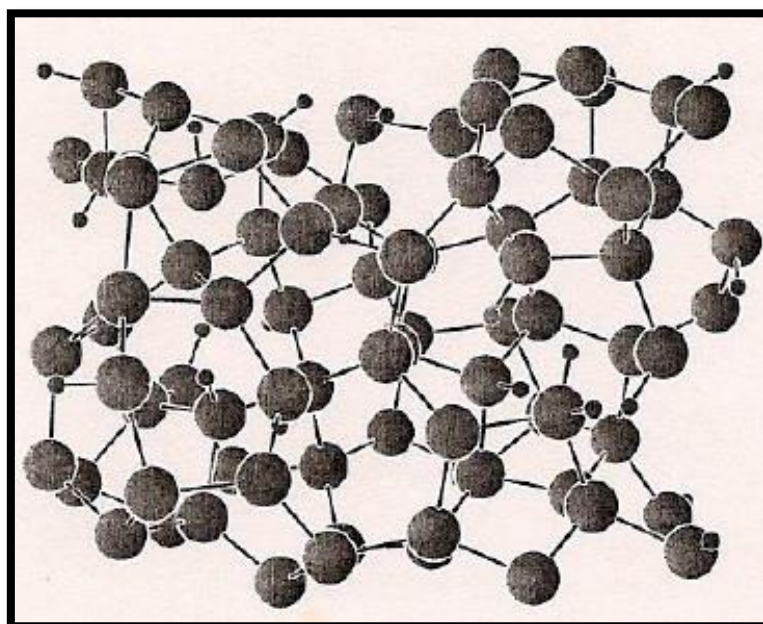


Figure 6 – Atomic structure model of a-Si:H illustrating the bonding disorder and the presence of hydrogen. Large disks represent Si atoms and small disks are hydrogen [15]

In order to grow films of a-Si:H, this material is deposited using a Plasma Enhanced Chemical Vapor Deposition (PECVD) machine shown in Figure 7, through the decomposition of several gases such as silane (SiH_4), hydrogen (H_2) and phosphine (PH_3). SiH_4 decomposes when exposed to temperatures above $450\text{ }^\circ\text{C}$ in the absence of plasma. Even though this condition allows the growth of amorphous films if the temperature is lower than $550\text{ }^\circ\text{C}$, the films have very low quality since these high temperatures do not permit the hydrogen molecules to stay linked to the structure of a-Si. In order to deposit films at lower temperatures, some energy source must be used to dissociate the SiH_4 , hence the use of PECVD, where the plasma serves as that energy source.

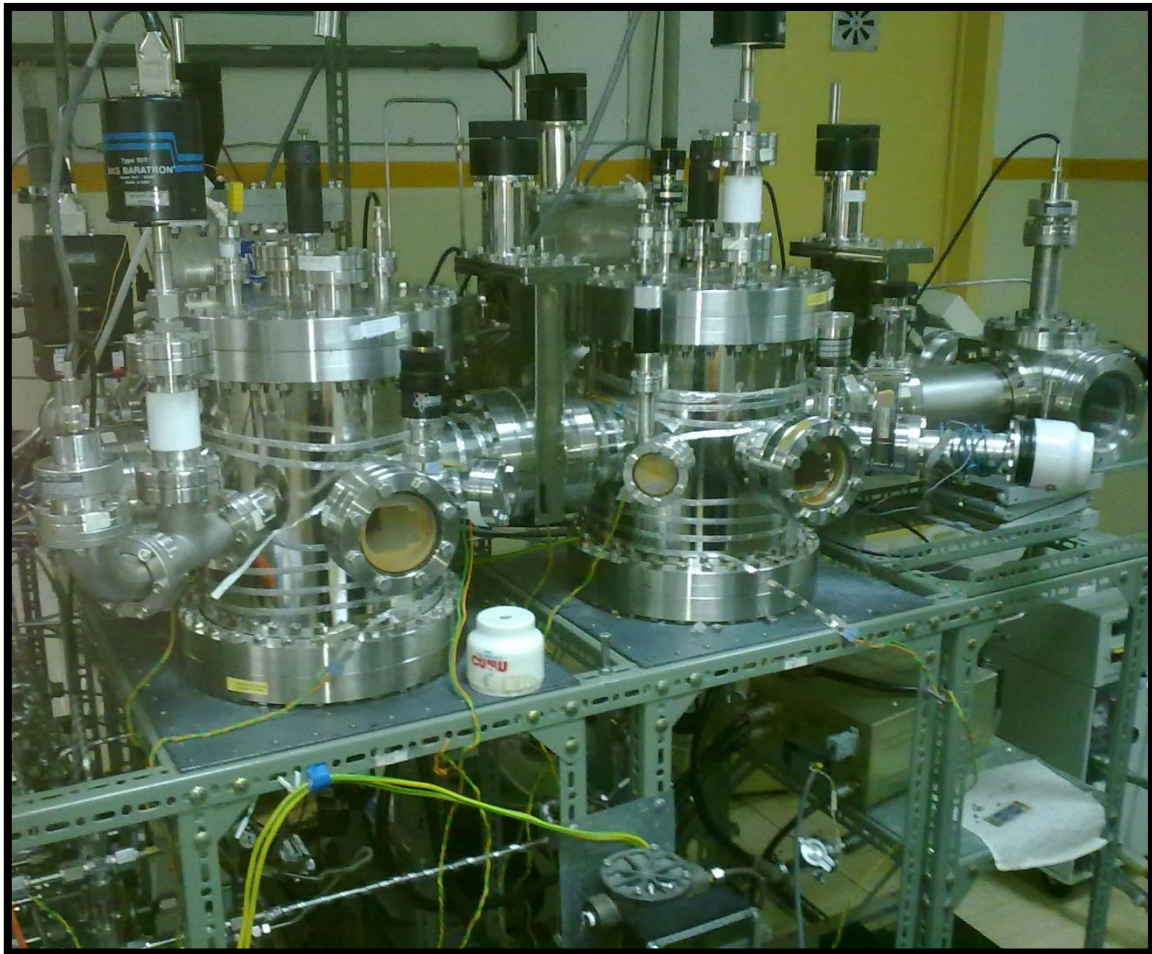


Figure 7 - PECVD Machine

Glass is the most common substrate to be used in this type of deposition, but any kind of material that can withstand these high temperatures is suitable for this purpose [17] [12] [15].

One of the film properties to be considered when using a-Si:H for MEMS applications is mechanical stress [12]. It is possible to induce different types of stresses into a structure, during the microfabrication process of MEMS devices.

Both compressive and tensile stress can be generated by altering the H_2 content in the chamber during the deposition process. For instance, an 83% content of H_2 will induce compressive stress, that creates a visible buckling effect on a bridge like structure, as if two forces were pushing

the bridge, one at each side, while a 33% content will have the opposite effect inducing tensile stress, as if those forces were now pulling to different and opposite direction, stretching the structure.

Figure 8 demonstrates several stress effects on different structures.

This ability to control stress during the microfabrication process is considered one of the major issues in MEMS development, since high stress can cause large defects on the devices causing fatal failures.

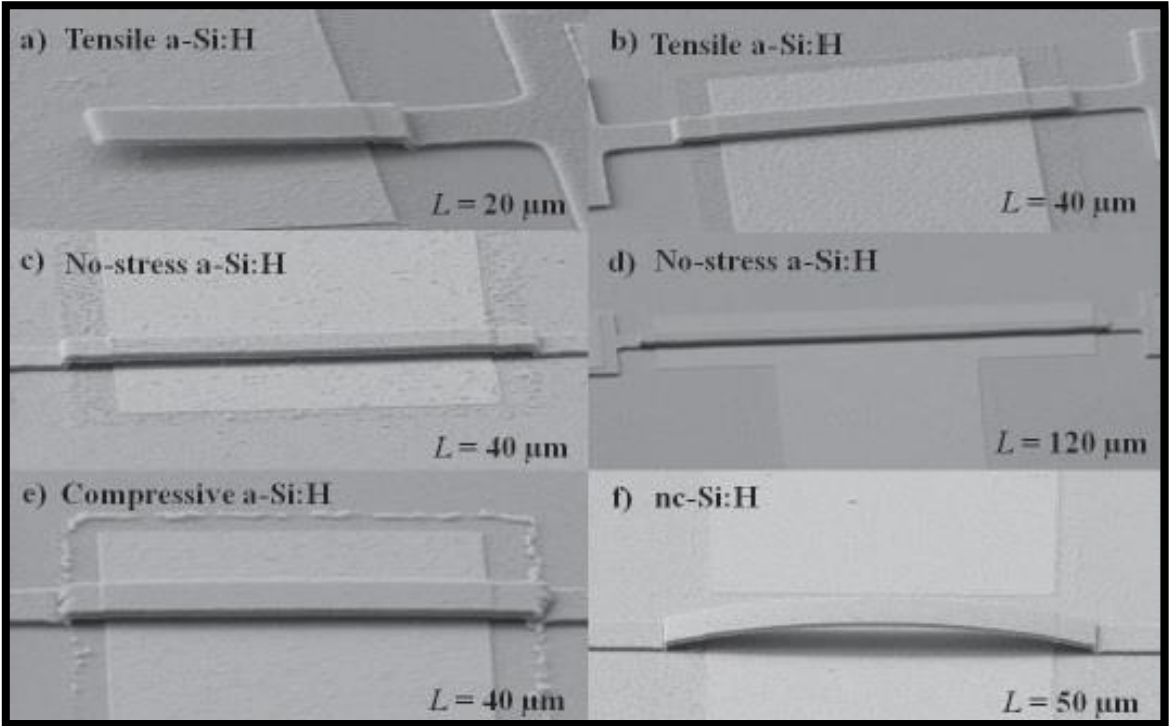


Figure 8 - SEM micrographs showing visual effects of stress in several structures [12]

1.4. MEMS Applications

One can consider that there is a fictitious line separating both typical IC applications and markets, from MEMS applications and markets. MEMS fabrication and technologies have the possibility to provide means to interlink the analog world with digital electronics.

Since the number of signals from the analog physical world is extremely vast, transduction mechanisms must be used as mentioned before, in order to transduce those signals to electrical signals (sensors), as well as transducing electrical to physical signals (actuators).

Since the market for MEMS applications is extensive, there is an inherent difficulty in defining it, due to its diversity. There are different definitions of MEMS that can be used which can lead to a disparity in the predicted values of sales that can vary in several billion dollars [9].

Despite this, some of the markets in which MEMS devices are most commonly applied are well defined, as it can be seen on Table 4.

Markets						
Applications	<i>Automotive Industry</i>	<i>Health Care Industry</i>	<i>Aerospace Industry</i>	<i>Industrial Products</i>	<i>Consumer Products</i>	<i>Tele-communications</i>
	Tire Pressure	Disposable Blood Pressure Transducer	Cockpit Instrumentation	Hydraulic Systems	Smart Toys	Optical Switches
	Brake Oil Pressure	Intrauterine Pressure Sensors	Sensors for Fuel Efficiency	Water-level Control	Bicycle Computers	Fiber-optic Couplings
	Engine Oil Pressure, Level and Quality	Angioplasty Pressure Sensors	Wind Tunnel Instrumentation	Agricultural Irrigations	Scuba Diving Watches	Radio Frequency MEMS in Wireless Systems
	Engine Coolant Temperature and Quality	Infusion Pump Pressure Sensors	Microgyroscope and Microsatellites	Refrigeration Systems	Vacuum Cleaners	Tunable Resonators

Table 4 - Market Industries and Applications for MEMS [5] [8]

As it is expected, the applications mentioned above are just a fragment, since the global range of those applications is extremely vast.

This work is focus mainly on the applications and descriptions of microresonators and actuators. Some of those applications can include small force detectors that are used in atomic force microscopy (AFM), biochemical sensors and ultrasensitive mass detectors, low-loss frequency filters, and mixers and switches for telecommunication applications [18].

There are several factors that should be taken into account when discussing the goals for MEMS applications in the future:

- The use of MEMS in large scale applications, to establish mass markets, in order to reduce costs, raise yield and efficiency;
- The creation of MEMS networks. There is a need to create many different functional systems and many similar functional systems working together to perform big tasks;
- The discovery of new materials;
- Exploration of new frontiers such as biological research and medical instruments, micro-energy sources, radio frequency and optical communication, environmental monitoring and protection, oceanographic studies, and of course nano-micro-mixed technologies [19].

Chapter 2 – Methods

2.1. Microfabrication

During this work, several runs were developed to fabricate the desired MEMS structures to be characterized, along with older devices previously fabricated. Since the fabrication process of the majority of the devices is similar, it will be described here the last microfabrication sequence performed.

Since the substrate used for the development of the devices mentioned above is glass, two Corning 1737 glass slides of 50x25 mm and 0.7 mm of thickness were selected, cleaned in an Alconox solution for 30 minutes to 1 hour, depending on the dust and dirt particles initially present on the substrate, and placed in a bath with ultrasounds and a temperature of about 65 °C. After this process, the slides were washed with deionized (DI) water and then blow dried using a compressed air gun.

After the preparation of the substrates, they are suitable to enter the clean room environment to start the microfabrication process. One layer of titanium tungsten (TiW) with 100 nm of thickness was deposited using a Nordiko 7000 machine. This machine functions by sputtering which is a deposition technique involving the shooting of energetic particles against a target of a specific material, TiW in this case, causing the release of particles from the target that are going to be deposited in the substrates. This procedure requires no pre-treatment.

The next step was the first lithography. After a pre-treatment that consisted on a coating with a photoresist, a mask previously designed in AutoCad, where the first layer mask, corresponding to the gates was used to pattern the TiW, in the DWL machine. DWL stands for Direct Write Laser, and it is a patterning machine that uses a laser beam to scan a sample that was coated with a photoresist. This machine is connected to a computer that has specific AutoCad designs which are transferred to the samples, creating the desired pattern. In this specific case a positive photoresist was used, meaning that the area that is exposed to the laser becomes soluble to the developer that is used to remove the excess photoresist, at the end of the process.

The following process was performed in LAM machine, consisting on a reactive ion etch (RIE) which was used to remove the excess TiW around the gates. For these samples the process took around 450 seconds. It is important to start with shorter time frames and then visual inspect to see if the excess TiW was removed, because too much etching time will start to etch the gates itself.

RIE is an etching technology that uses reactive plasma to remove thin film atoms through the reaction from the ions in the plasma and the sample, creating volatile compounds. After etching, the samples were immersed in a solution of Microstrip in order to remove the excess photoresist left from the lithography process. The samples were then removed, washed with acetone and H₂O, and dried with a compressed air gun. This run included structures with different lengths and also with different number of gates *per* structure (one, two and four). Figures 9 and 10 demonstrate the final aspect of those gates after this sequence of steps.

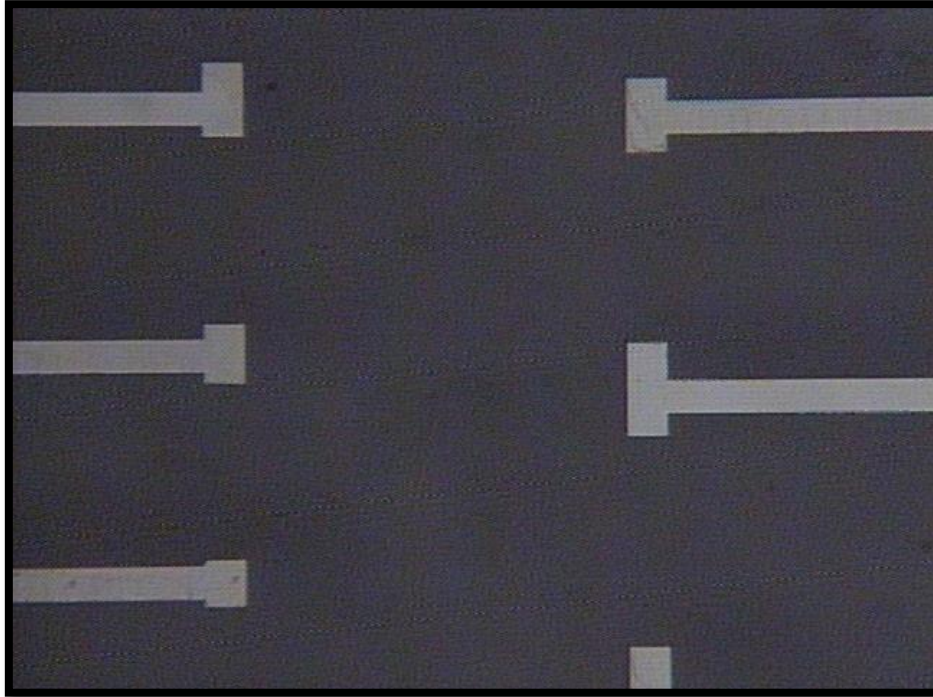


Figure 9 - Micrograph of single gate die after RIE

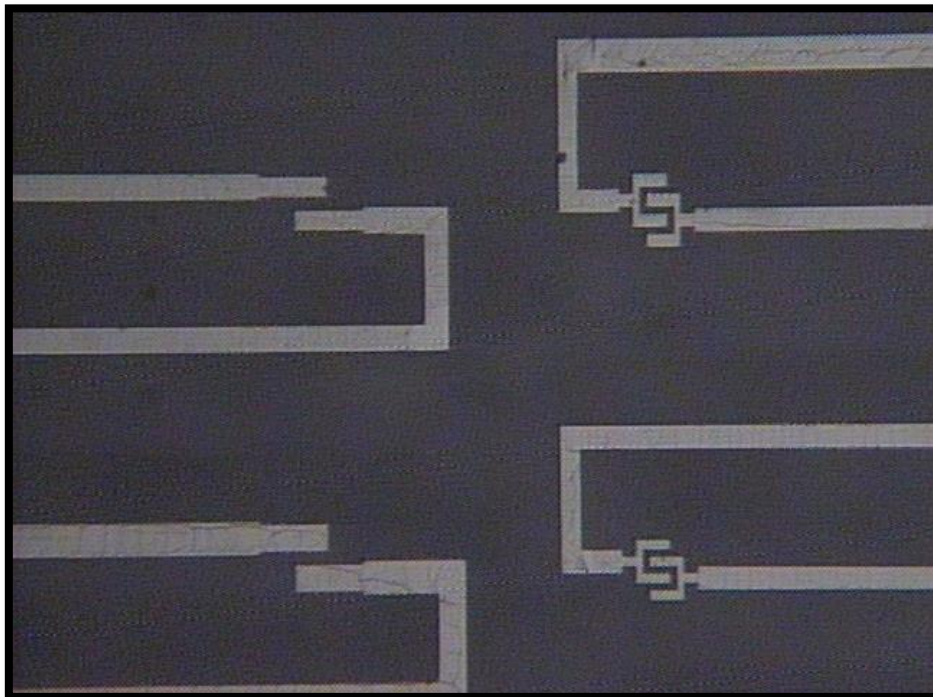


Figure 10 - Micrograph of die with two (left) and four (right) gates

Nordiko 7000 machine was used again in order to deposit 1 μm of Aluminum (Al) that served as the sacrificial layer, that is the layer that will be between the gates and the structures itself that later was removed leaving the structures suspended.

The process is equal to the one mentioned above except that the target is different, so the particles deposited on the samples are from Al instead of TiW.

The second lithography was the next step. The pre-treatment was equal to the first one and the second layer mask corresponding to the sacrificial layer was used to pattern the samples. Since it was the second layer, it was fundamental to use the alignment marks present in each layer, to make sure that the consequent layer is perfectly aligned with the previous one.

The consequent etching process was a wet etch where a chemical solution containing acids, bases or alcohols is used. For this case an Al etchant was used which is an acid solution to selectively remove Al. This procedure took between 10 and 15 minutes. The samples were then submersed in H₂O and dried with a compressed air gun. Then the excess photoresist from the lithography was removed using Microstrip, washed with acetone and H₂O and dried again.

Figure 11 shows the final aspect after the wet etch where a layer of Al is visible covering the gates that served as the sacrificial layer.

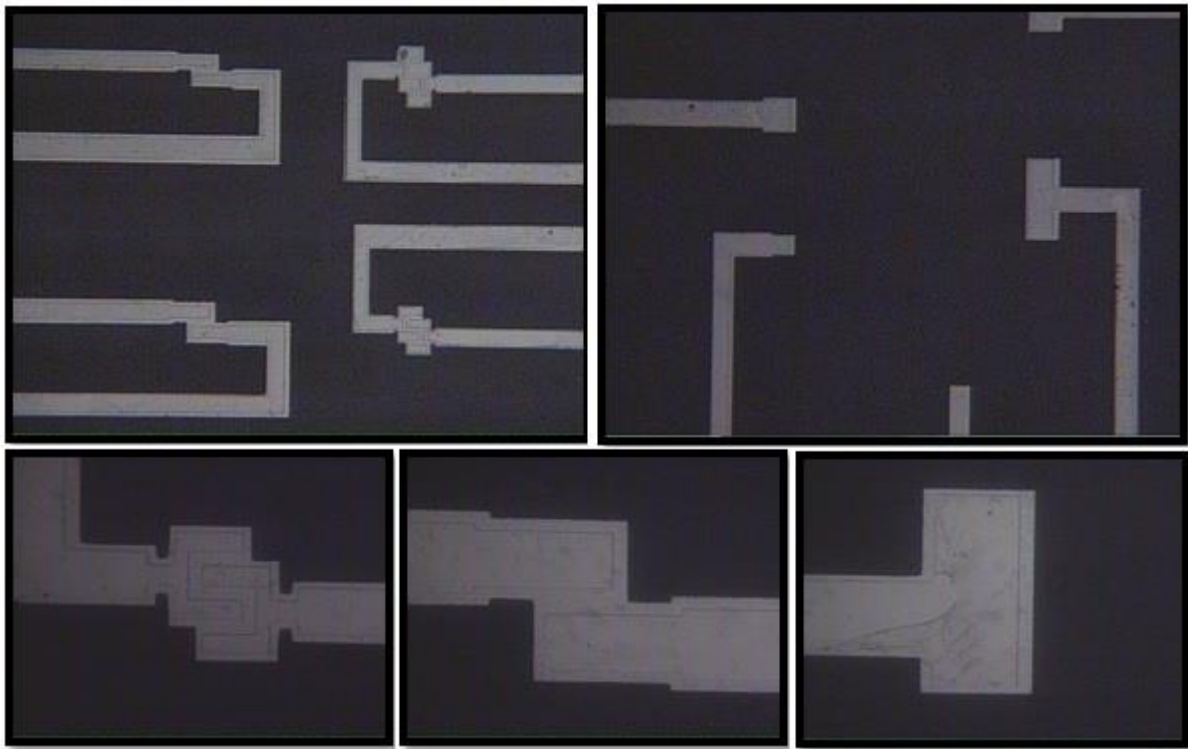


Figure 11 - Micrographs of different gates covered with an Al layer

The structural layer of the structures is made of a-Si:H which was deposited by RF-PECVD. Plasma Enhanced Chemical Vapor Deposition is a process that deposits thin films from a vapor state to a solid state on the samples using plasma as energy source, as it can be seen on Figure 12. By adjusting the H₂ content it is possible to deposit films inducing different levels of stress.

For these samples, low stress was induced, by using a H₂ content of 73%. 1 μm of a-Si:H was deposited to create the structural layer, with a deposition time of 1 hour.

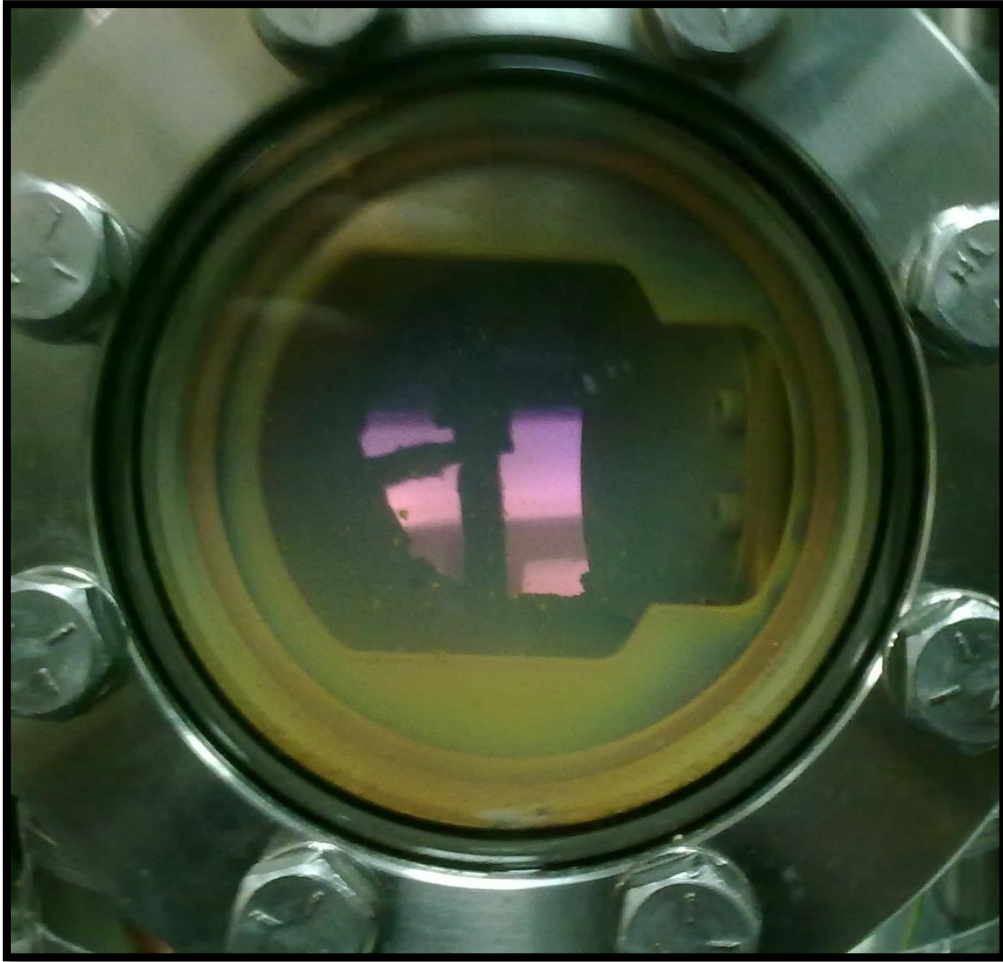


Figure 12 - Plasma Energy Source during a deposition process

In Nordiko 7000, 100 nm of TiW was then deposited on top of the a-Si:H, in order to create a metallic conductive surface on top of the structures. This also allowed skipping an additional lithography step to do the bridges and the pads separately, since the etching process could be done on both of the materials simultaneously.

The last lithography step was made, in the same manner of the previous ones, including the coating, the alignment of the third layer mask, and the development.

Another RIE was then made in LAM in order to etch both a-Si:H and TiW. It was made in two runs, first during 300 seconds and a second one during 150 seconds, separated by a visual inspection to guarantee that there was no over etching.

After this step, the samples were submersed in Microstrip to remove the excess photoresist, washed with acetone and H₂O, and dried (Figures 13 and 14).

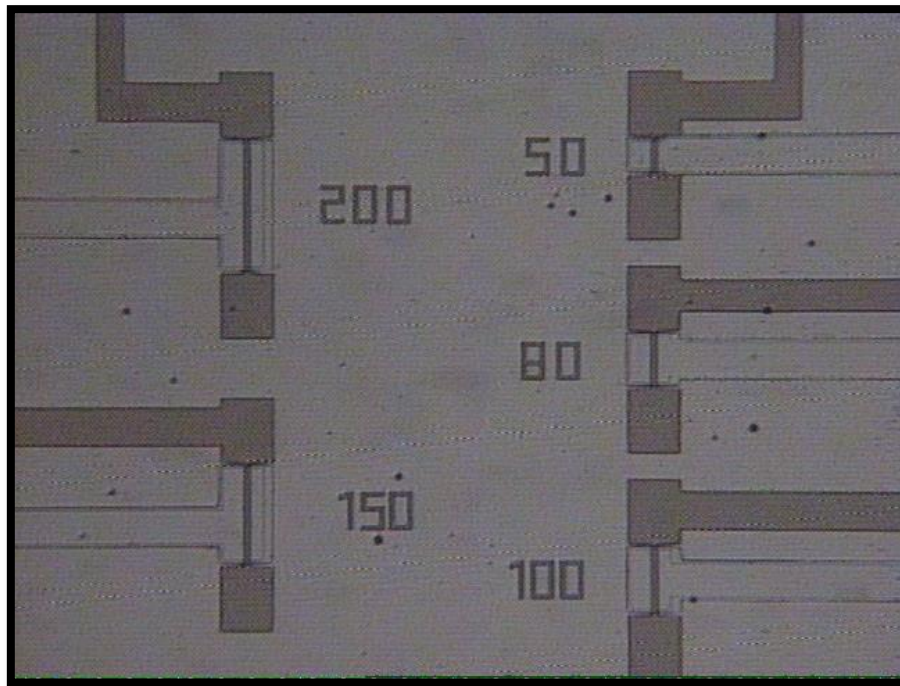


Figure 13- Single gate structures after last lithography and RIE

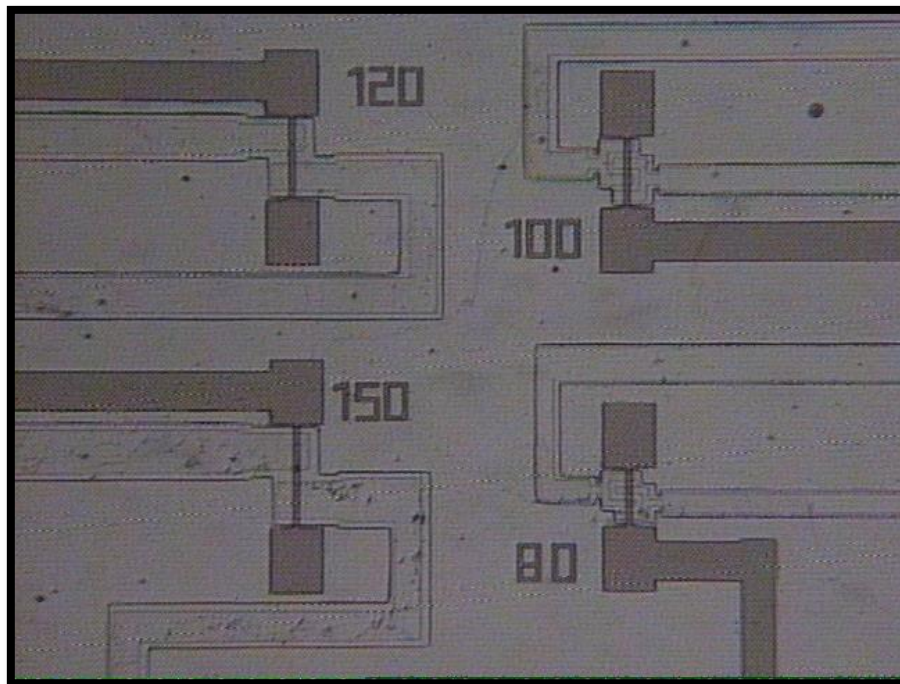


Figure 14 - two and four gates structures after last lithography and RIE

After this process was finished, the samples were covered with photoresist, which will function as a protective layer, so the structures will not be destroyed during the cutting of the individual dies.

Since the dies were all fabricated on the same samples, Disco DAD 321 machine was used to separate the dies from each other (Figure 15). This machine did 6.5 mm by 6.5 mm cuts for this case. To finish, the samples were exposed to UV light.

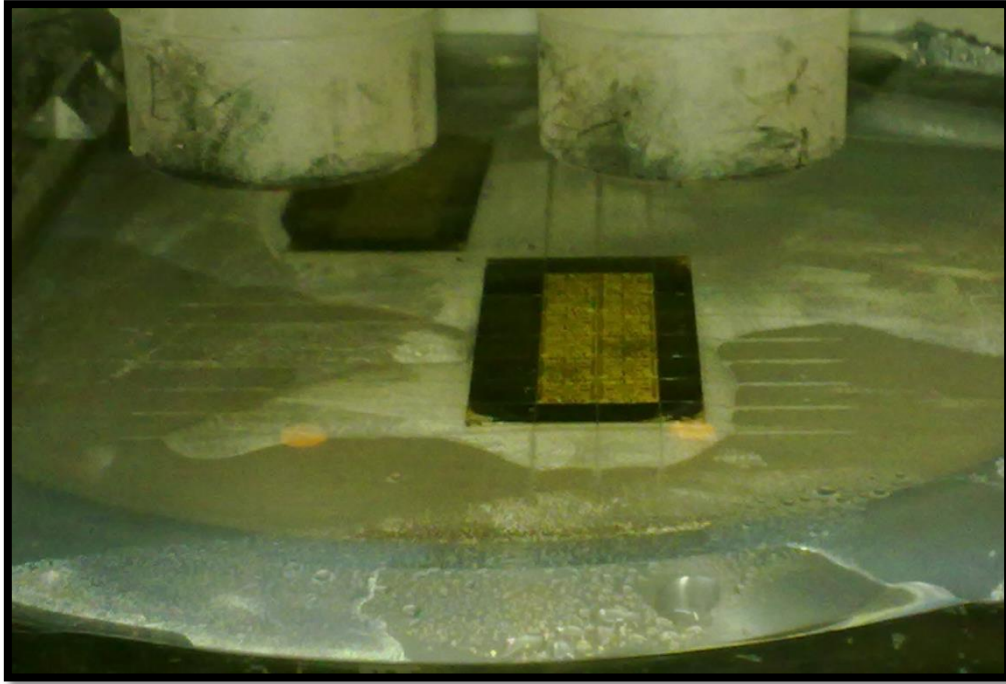


Figure 15 - Cutting of the dies in Disco DAD 321

Subsequently the dies were separated, and the last process to be done was the release of the structures, by removing the Al sacrificial layer present between the gates and the bridges. The photoresist used to protect the samples during the cutting was removed with Microstrip, washed with acetone and H₂O and dried. This wet etching process involves four liquids with different surface tensions, and the samples were submersed sequentially from the higher surface tension to the lower. This is done so the structures do not collapse or get stuck to the substrate. The liquids are Al etchant, H₂O, Isopropyl alcohol (IPA) and n-hexane. Table 5 shows the time that the structures were submersed in a given liquid, along with their surface tensions.

Liquid	Immersion Time	Surface Tension
Al etchant	3 hours	75 mN/m
H ₂ O	3 minutes	73 mN/m
IPA	3 minutes	23 mN/m
n-hexane	3 minutes	18 mN/m

Table 5 - Liquids used for release of the structures, immersion time and surface tension

Figure 16 shows the final results after the complete microfabrication process. It is possible to observe that the sacrificial layer was removed, and the structures are suspended. In amplification, bridges of 50 μm , 80 μm and 150 μm with one, two and four gates can be seen.

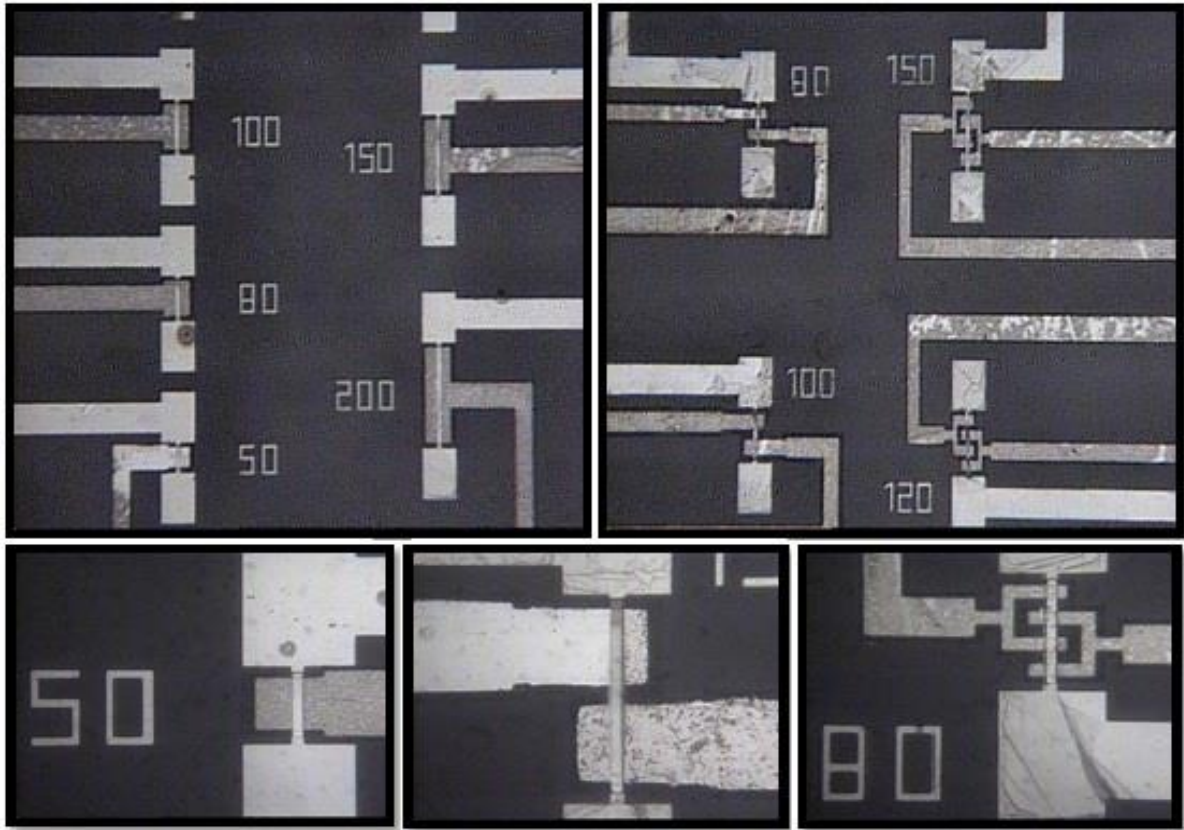


Figure 16 - Micrographs of several structures after their release

For this process as it was mentioned before, two glass substrates were used. For each of the substrates, two rows of six dies were fabricated, one row containing dies with single gate structures while the second row has structures with both two and four gates, in a total of twenty four devices, twelve with one gate, and twelve with two and four gates.

In order to get the devices ready to be optically characterized, the dies were glued onto chip carriers containing several pins that can be fitted in a special socket to allow for the passage of current into the structures.

To connect the chip carriers to the dies, one last step before any measurement can be done must be performed. That process is called wire bonding and consists on a special machine that is used to connect small thin aluminum wires from the chip carrier to the die, to allow the passage of current from an external source to the structures, which will induce the vibration of the structures. After this, the chips are ready to be used for any kind of measurements.

The structures fabricated in this process range from 50 μm to 200 μm , depending on the design of the masks, and all of them have a width of 10 μm .

2.2. Characterization

After the fabrication of the devices, they were optically characterized, to measure the resonance frequency and to perform the extraction of the Q-factors of the structures. To do this, the

chips were placed individually in a vacuum chamber (Figure 17) on a specially designed socket, at a pressure of around 10^{-2} Torr. This chamber will decrease the air damping effects thus allowing measuring the Q-factors at their maximum values.

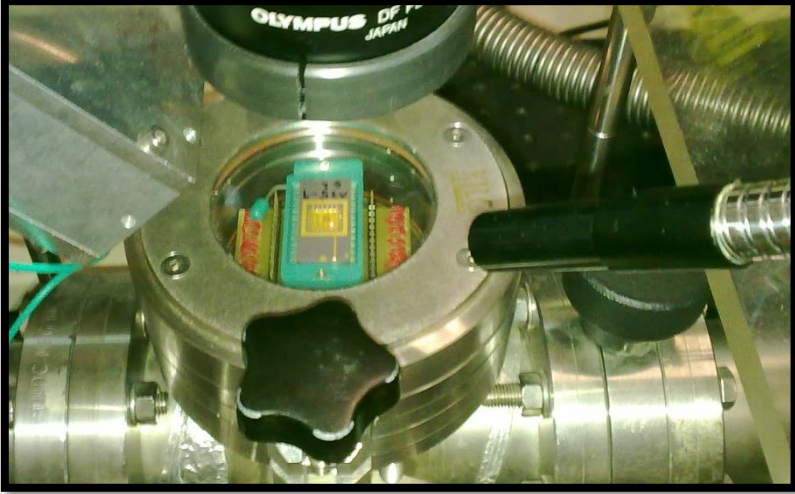


Figure 17 - Optical setup vacuum chamber

In the chamber, the structures were electrostatically actuated, and using a red laser diode with a wavelength of 658 nm focused on the surface of the chip which is then reflected on a photodetector integrated with an amplifier, it is possible to detect the deflection of the actuated structure since it causes changes in the output signal of the photodetector [12]. An Olympus SZX12 research stereo microscope was used to visualize the devices to facilitate the positioning of the laser beam directly on top of the structures.

An HP 4195A network analyzer was used to sweep the excitation frequency of each structure, by varying the AC and DC components the output of the photodetector is measured as an amplitude spectrum thus creating a *Fres* peak detected by the network analyzer (Figure 18).

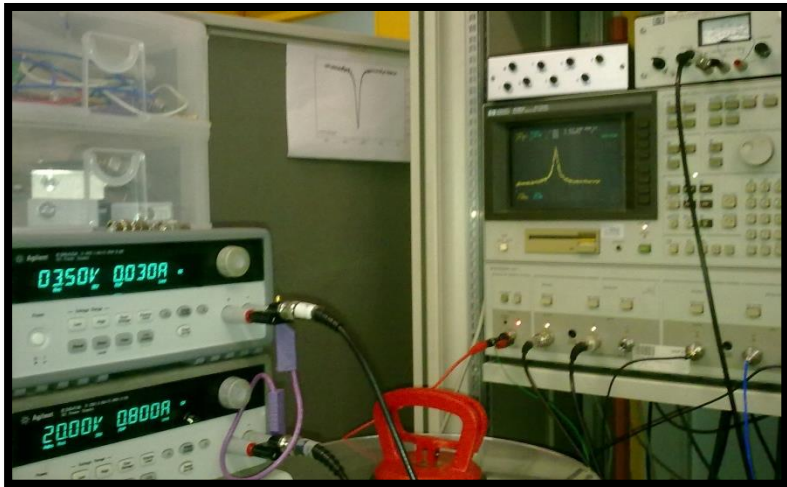


Figure 18 - Spectrum Analyzer

One can define F_{res} as an ability of a given system to oscillate or vibrate with certain amplitudes, at different frequencies. These systems store vibrational energy leading to large amplitude oscillations. As mentioned above, when measuring a certain structure with a network analyzer, several peaks can be detected at certain frequencies, when specific AC and DC currents are applied. Those peaks occur when there is a match between the excitation frequency and the resonance frequency of the structure that is being tested [20].

Several models can be used to predict the F_{res} of structures. The values that are extracted from those models serve as comparison terms against the real values measured by the user. One of the models used for this work to determine the theoretical values of F_{res} is presented in Equation 1.

$$F_{res} (Hz) = \left(\frac{t}{l^2}\right) \times \sqrt{\frac{E}{\rho}}$$

Equation 1 - Theoretical Model for Resonance Frequency calculation

Where:

- t – thickness [m]
- l - length [m]
- E - Young's Modulus [Pa]
- ρ – density [Kg/m^3]

This model is suitable for bridge like structures.

Since this work focuses on biosensing, it is also important to take into account some theoretical models for F_{res} calculation both in air as in water, since there is a shift in F_{res} when exposing the devices to different media such as air or water. Equation 2 demonstrates that relation.

$$F_{res_{water/air}} (Hz) \cong \sqrt{\frac{\rho_{bridge} \times t}{\frac{\pi}{4} a w \rho_{water/air} + \rho_{bridge} \times t}} \times F_{res_{vac}}$$

Equation 2 – Theoretical Model for Resonance Frequency calculation in air and water [1]

Where:

- a – 1.05 (numerical parameter for a thin rectangular beam);
- t – thickness [m]
- w – width [m]
- $\rho_{water/air}$ – density of the fluid (water or air respectively) [Kg/m^3]
- ρ_{bridge} – density of the structure [Kg/m^3]
- F_{res} – resonance frequency [Hz]

Another important key factor when determining the F_{res} of a given structure for biodetection is the way that a mass will affect the shift in the frequency when applied on top of the resonator. For this, one can calculate the changes in F_{res} using Equation 3.

$$\Delta F_{res} = -\frac{1}{2} \frac{\Delta m}{m} F_{res_i}$$

Equation 3 - Resonance Frequency shift when a mass is added [21]

Where:

- ΔF_{res} – resonance frequency shift [Hz]
- Δm – added mass on top of structure [Kg]
- m – mass of the structure without any mass on top [Kg]
- F_{res_i} – initial resonance frequency of the structure before the addition of extra mass [Hz]

As it is known, the Q-factor determines the minimum detectable F_{res} shift (ΔF_{res}) after loading-mass (Δm) adsorption. Given that, it is safe to say that Equation 3 is directly proportional to $1/Q$ [22].

From the network analyzer it is possible to extract the Q-factor of the structures using a computational program, to analyze the spectrum from the output of the photodetector. The Q-factor of any kind of MEMS device is considered a dimensionless parameter that measures the energy loss of a given structure. It can also be defined as a ratio between the total energy of the system and its average energy loss [23]. Given that, it is possible to enhance the Q-factor by reducing the total energy loss of a system. That relation is demonstrated in Equation 4.

$$Q = (2 \times \pi) \times \left(\frac{E}{\Delta E} \right)$$

Equation 4 - Quality Factor energy ratio

Where:

- E - total system energy [Kg · m²/s²] or [J]
- ΔE - average energy loss in one radian [Kg · m²/s²] or [J]

In MEMS, energy dissipations come from a large number of sources as expected. Hence, one can also use Equation 5 to determine the Q-factor of a given structure.

$$\frac{1}{Q} = \frac{1}{Q_{air}} + \frac{1}{Q_{anchor}} + \frac{1}{Q_{TED}} + \frac{1}{Q_{other}}$$

Equation 5 - Quality Factor calculation using energy losses terms

Where:

- Q_{air} - air damping;
- Q_{anchor} - losses in the anchor area;
- Q_{TED} - thermo-elastic dissipation;
- Q_{other} - intrinsic material losses.

As Equation 5 demonstrates, the Q-factor can be defined as the sum of all of the energy losses components. Despite that, Q-factor is ultimately defined by the properties of the device itself, due to the fact that most of the energy losses can be controlled [24].

For values close to the resonance of a structure, and for small damping ratios, the deflection of the F_{res} peak can be approximated by a Lorentzian curve [12].

The Q-factor can be extracted directly from the F_{res} peak representation, by knowing both the F_{res} and the full width at half maximum (FWHM) that represents the difference between the extreme values of the independent variable which is the frequency, at which the dependent variable corresponding to the spectrum amplitude is equal to half of its height. With these parameters the Q-factor can be extracted by Equation 6.

$$Q = \frac{F_{res}}{FWHM}$$

Equation 6 - Quality Factor calculation using FWHM

Where:

- F_{res} - resonance frequency [Hz]
- $FWHM$ - full width at half maximum of the resonance intensity spectrum [Hz]

That extraction of the Q-factor can also be extracted from the resonance frequency peak using Equation 7.

$$Q = \frac{F_{res}}{\Delta F_{-3dB}}$$

Equation 7 - Quality Factor extraction [12]

Where:

- F_{res} – resonance frequency [Hz]
- ΔF_{-3dB} – width of the resonance peak 3 dB below (~70% of) its maximum value [Hz]

MEMS can be characterized regarding its dynamic behavior, which aims to the definition of the devices behavior in working conditions, and how they perform regarding its *Fres*, selectivity, noise and Q-Factor [25].

Advanced testing of the dynamic behavior of MEMS is a key issue to perform in order to develop reliability or marketability of the devices [26]. This dynamic testing when supported by high-speed visualization can also comprise vast information on operability, durability, shock sensitivity, and failure, as demonstrated on Table 6 [27].

Information obtainable by the dynamic testing of MEMS devices	
1	Testing of the operability of the actuator
2	Verification of a coordinated action within complex multiple devices
3	Provision of relevant physical data (kinematic, temperature, materials data, etc)
4	Revelation of unwanted vibrations (resonance modes)
5	Testing of mechanical cross-talk effects within multiple arrays of devices
6	Maximization of conversion efficiency
7	Minimization of detrimental heating ('hot spots')
8	Verification of a proper response with the macroscopic world
9	Study of the response in a harsh environment
10	Investigation of reasons for a premature failure

Table 6 - Information obtainable by using high-speed visualization [27]

This dynamic response of MEMS can also change when varying the amplitude and frequency of the exciting voltages. Other key aspects are the effects of air damping that can induce significant changes in the dynamic behavior of the devices [28].

The microfabrication processes and material characteristics limitations can restrict this dynamic behavior. Due to this, there is a need to overcome some intrinsic limitations inherent to MEMS devices, by using reliable, cost effective and non-contact testing systems.

This is very important due to the micro scale size of MEMS structures, since any kind of aggressive contact testing may damage the structures, since they are extremely fragile and thin. The dynamic behavior is crucial to understand in order to enable the successful use of MEMS devices as sensors or actuators [29].

Chapter 3 – Experimental Results

3.1. Vacuum Characterization

The first goal to fulfill in this project is to obtain a reliable vacuum characterization. Due to the absence of air damping effects, the available structures will have an optimized operation in a vacuum environment when actuated at their mechanical F_{res} [30]. The Q-factors are at their maximum value in vacuum, decreasing when dissipation occurs.

As mentioned in the previous chapter the devices were electrostatically actuated in a vacuum chamber, with coaxial feedthroughs for electrical connections and a glass window allowing the access of a red laser diode, where its deflection was measured with an optical setup shown in Figure 19 [31]. For these early measurements, the devices were submitted to pressures of $\sim 10^{-2}$ Torr.

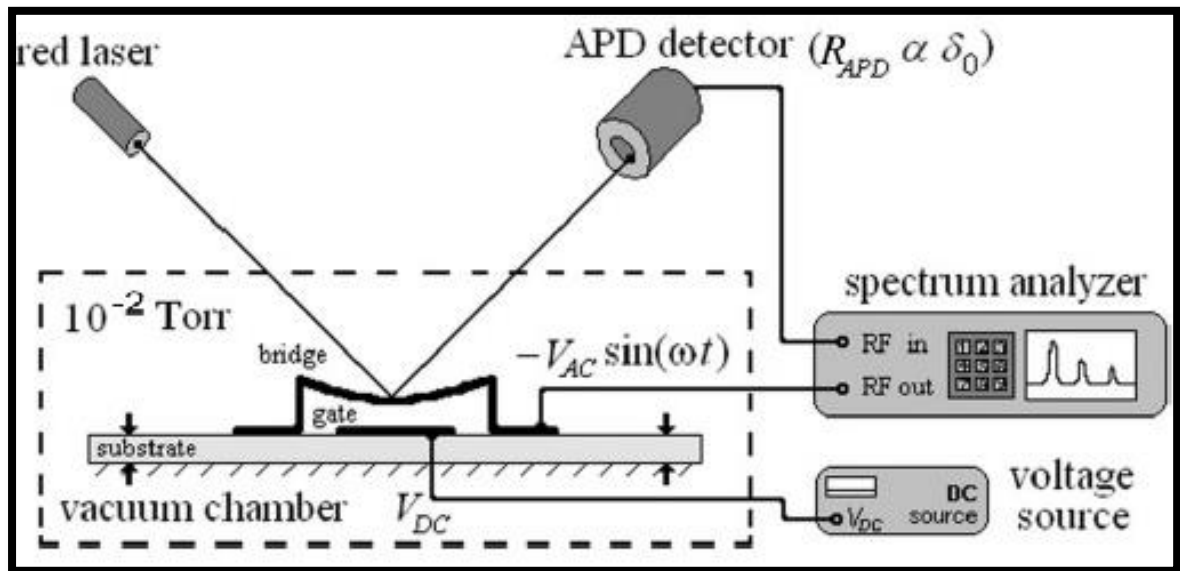


Figure 19 - Schematic diagram of the measurement setup in vacuum. Measuring the deviation of the reflected laser beam with a photodetector monitors the resulting vibration [31]

Due to the application of a voltage, the structure will vibrate as a result of an electrostatic force. That voltage V_G , has an AC and DC components, as demonstrated in Equation 8.

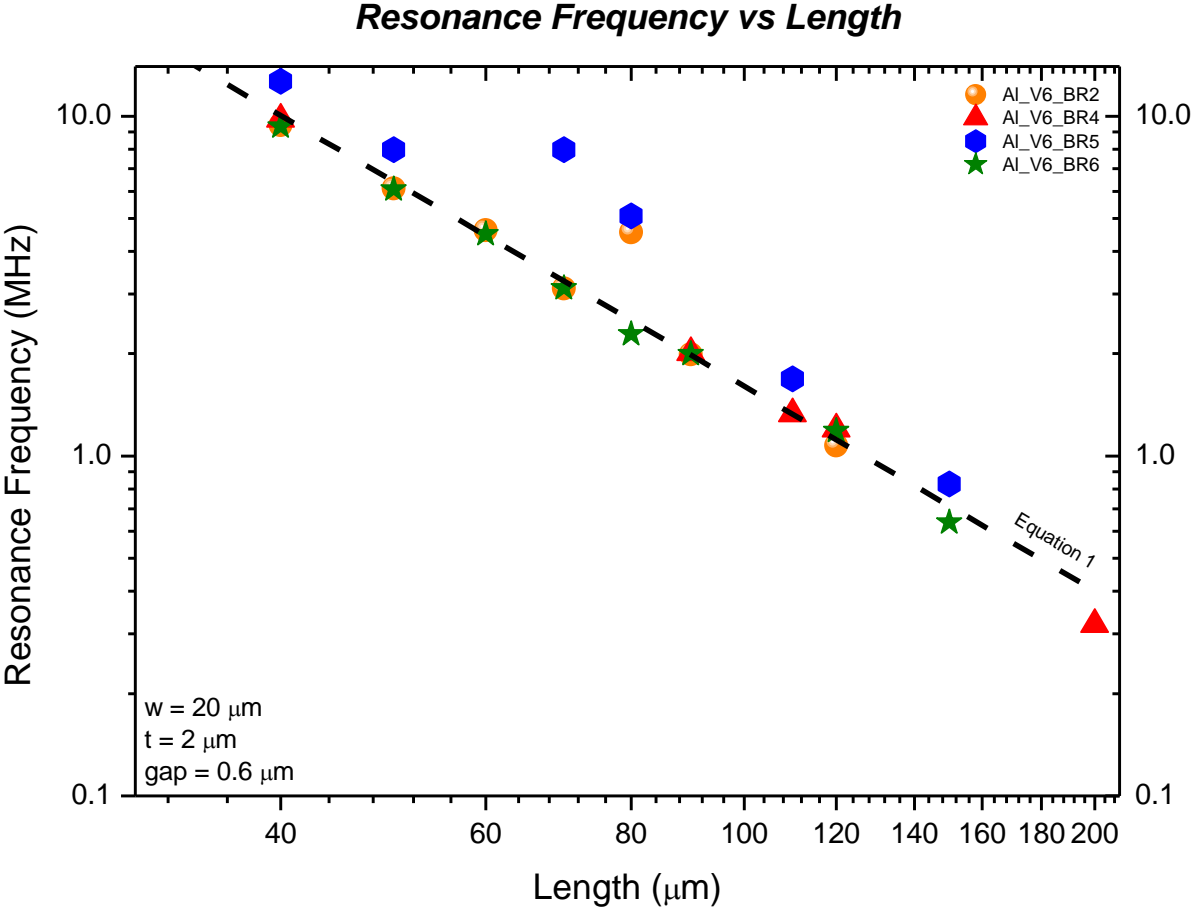
$$V_G(t) = V_{dc} + V_{ac} \sin(2\pi ft)$$

Equation 8 - Applied voltage with AC and DC components [31]

Where:

- V_{dc} – amplitude of the DC component [V]
- V_{ac} – amplitude of the AC component [V]
- f – excitation frequency [Hz]

Some of the early vacuum measurements were performed to bridge like structures with 40 μm to 200 μm in length, 20 μm of width and 2 μm of thickness. The gap between the bridges and the gates is 0.6 μm , and the sacrificial layer used in the microfabrication process was Al, for these specific devices. Graphic 1 represents the *Fres* of several bridges from different devices as a function of their length. Those frequencies range from ~0.5 MHz to 10 MHz. The higher frequencies correspond to the shorter structures, while the lower correspond to the longer structures.

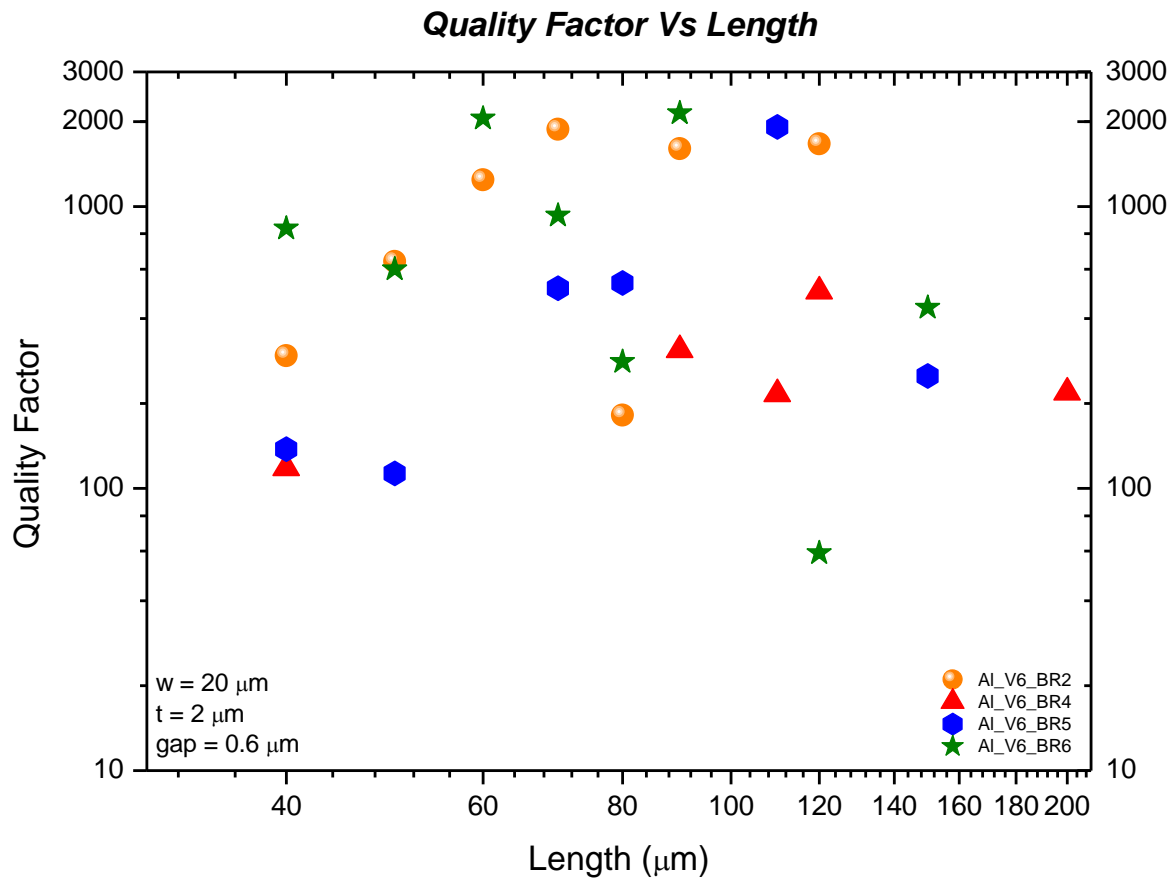


Graphic 1 - Resonance Frequency as a function of Length. $E = 150 \text{ GPa}$; $\rho = 2330 \text{ Kg/m}^3$; Pressure $\approx 10^{-2} \text{ Torr}$

Some of the data points presented above are slightly off the theoretical line which can be explained by several hypotheses such as the destruction of the bridges that can now be operating as cantilevers.

The bridges anchors may break during actuation transforming the structures into long cantilevers, or the structures can be fractured somewhere in the middle creating two cantilevers. In this case, if the smaller cantilever is very short, and it is the one that is being detected, its *Fres* will be similar to the one from a bridge. Some over-etching in specific places or not having a homogeneous deposition of structural material during the microfabrication that can lead to different thicknesses for different devices is also a valid conclusion. The data points that are shown further away from the theoretical line correspond to higher frequency modes, which will be explained later.

From the resonance frequency peaks of these measured devices, the Q-factors were also extracted as represented in Graphic 2.

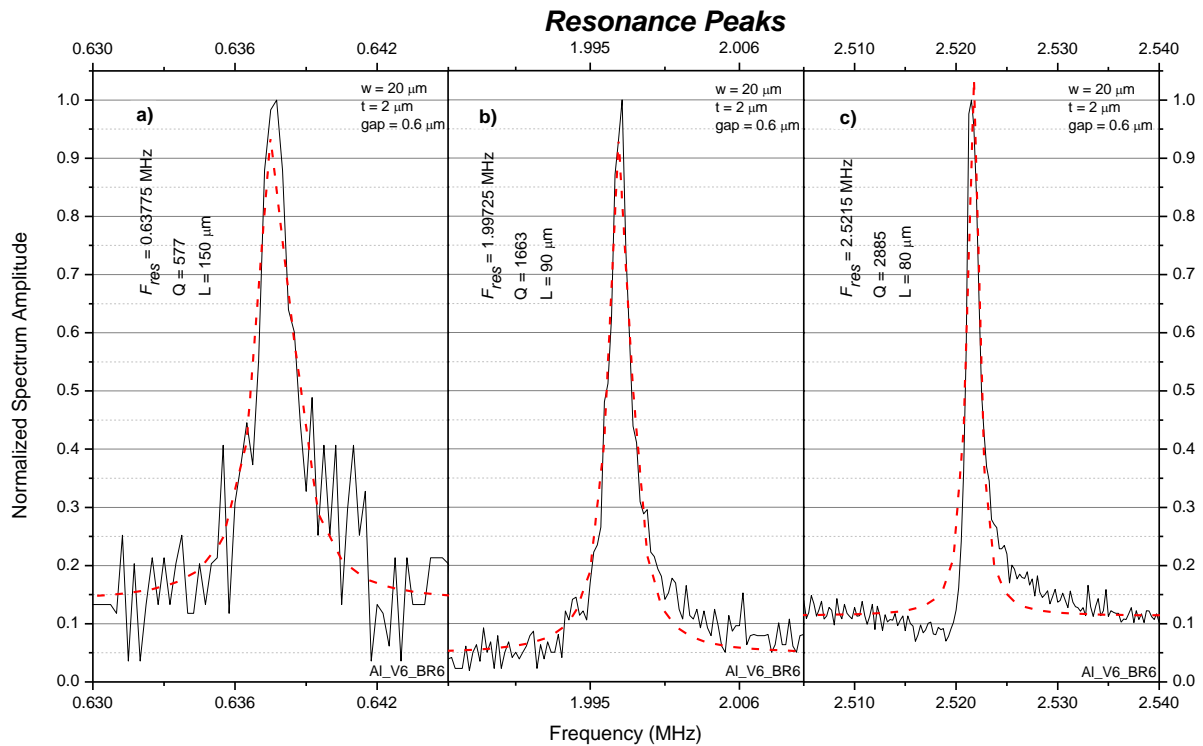


Graphic 2 - Q-factor as a function of Length. $E = 150 \text{ GPa}$; $\rho = 2330 \text{ Kg/m}^3$; Pressure $\approx 10^{-2} \text{ Torr}$.

For these devices, the Q-factors in vacuum range from ~ 100 to 3000 and appear to be independent from the length of the structures for lengths above $70 \mu\text{m}$. For smaller lengths the Q-factors may have a tendency to increase with length which may indicate that clamping losses dominate the energy dissipation when the length of the structures is closer to its width and to the dimensions of their supports [32].

Even though this conclusion is fairly accepted, it cannot be considered as a rule since the Q-factor is going to depend on the properties of each individual structure whether they are shorter or longer.

Graphic 3 represents the F_{res} and Q-factors extracted from an adjustment with a Lorentzian curve to the resonance peaks of three structures with $150, 90$ and $80 \mu\text{m}$, and it demonstrates the real aspect of measured resonance peaks, where it is possible to see that for lower Q-factors, the aspect of the peak is wider as shown in Graphic 3 a), when compared with a peak with higher Q-factor, where the peak is much more thinner as demonstrated in Graphic 3 c), which is consistent with Equation 6.



Graphic 3 - Resonance frequencies and Q-factors extracted from the Lorentzian curve adjusted to the peaks. a) 150 μm fixed bridge; b) 90 μm fixed bridge; c) 80 μm fixed bridge. $E = 150 \text{ GPa}$; $\rho = 2330 \text{ Kg/m}^3$; Pressure $\approx 10^{-2} \text{ Torr}$.

3.2. Vibrational Modes

When excited, MEMS devices vibrate at certain frequencies. Each structure can vibrate at different frequencies where the lowest vibrational frequency is defined as fundamental and the following are called harmonics. Those vibrations cause wave like deformations on the structures that are referred as modes. As explained earlier, the F_{res} can be extracted from Equation 1, which corresponds to the fundamental vibrational mode ($n=1$). So, by multiplying Equation 1 by n , where n stands for the desired mode, it is possible to extract the theoretical values of any given harmonic.

Figure 20 shows the mechanical deformations on a given bridge like structure corresponding to the first five modes.

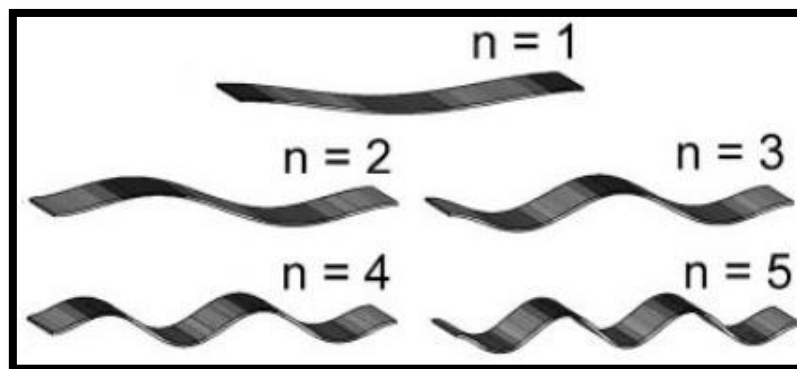


Figure 20 - Fundamental and Harmonics Modes [31]

As it is shown in Figure 20, for any n mode, the flexural movement of a given structure contains $n-1$ nodes and n antinodes.

The boundary conditions of these fixed structures can also be extracted, by calculating the ratio of the F_{res} of both the fundamental mode and its harmonics, according to Equation 9 [31].

$$r_i = \frac{f_{res}(n = i)}{f_{res}(n = 1)}$$

Equation 9 - Boundary condition extraction from frequencies ratio [31]

In Figure 21 it is shown that different types of structures have distinct conditions.



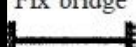
Beam	Boundary conditions	Frequency condition	Frequency condition, $\sigma_0 \rightarrow 0$	a_n coefficients
	$\delta_Y(0) = \delta_Y^{(1)}(0) = 0$ $\delta_Y^{(2)}(L) = \delta_Y^{(3)}(L) = 0$	$\frac{1}{2} \left(\frac{\lambda_+}{\lambda_-} - \frac{\lambda_-}{\lambda_+} \right) \sin\left(\frac{L}{\lambda_-}\right) \sinh\left(\frac{L}{\lambda_+}\right)$ $+ \cos\left(\frac{L}{\lambda_-}\right) \cosh\left(\frac{L}{\lambda_+}\right) + \frac{1}{2} \left(\frac{\lambda_+^2}{\lambda_-^2} + \frac{\lambda_-^2}{\lambda_+^2} \right) = 0$	$\cos(\sqrt{\beta}L) \cosh(\sqrt{\beta}L) + 1 = 0$	$a_1 \cong 0.096\ 86$ $a_2 \cong 0.99\ 418$ $a_3 \cong 2.000\ 25$ $a_{n \geq 4} \cong n - 1$
	$\delta_Y(0) = \delta_Y(L) = 0$ $\delta_Y^{(2)}(0) = \delta_Y^{(2)}(L) = 0$	$\sin(L/\lambda_-) = 0$	$\sin(\sqrt{\beta}L) = 0$	$a_{n \geq 1} = n - 1/2$
	$\delta_Y(0) = \delta_Y(L) = 0$ $\delta_Y^{(1)}(0) = \delta_Y^{(1)}(L) = 0$	$\frac{1}{2} \left(\frac{\lambda_+}{\lambda_-} - \frac{\lambda_-}{\lambda_+} \right) \sin\left(\frac{L}{\lambda_-}\right) \sinh\left(\frac{L}{\lambda_+}\right)$ $+ \cos\left(\frac{L}{\lambda_-}\right) \cosh\left(\frac{L}{\lambda_+}\right) - 1 = 0$	$\cos(\sqrt{\beta}L) \cosh(\sqrt{\beta}L) - 1 = 0$	$a_1 \cong 1.005\ 62$ $a_2 \cong 1.999\ 75$ $a_3 \cong 3.000\ 01$ $a_{n \geq 4} \cong n$

Figure 21 - Frequency conditions for cantilever, supported and fixed-fixed bridges with different boundary conditions [31]

By recovering Equation 1 and adding the extracted values of that ratio it is possible to calculate the F_{res} of the vibrational modes, as shown in Equation 10.

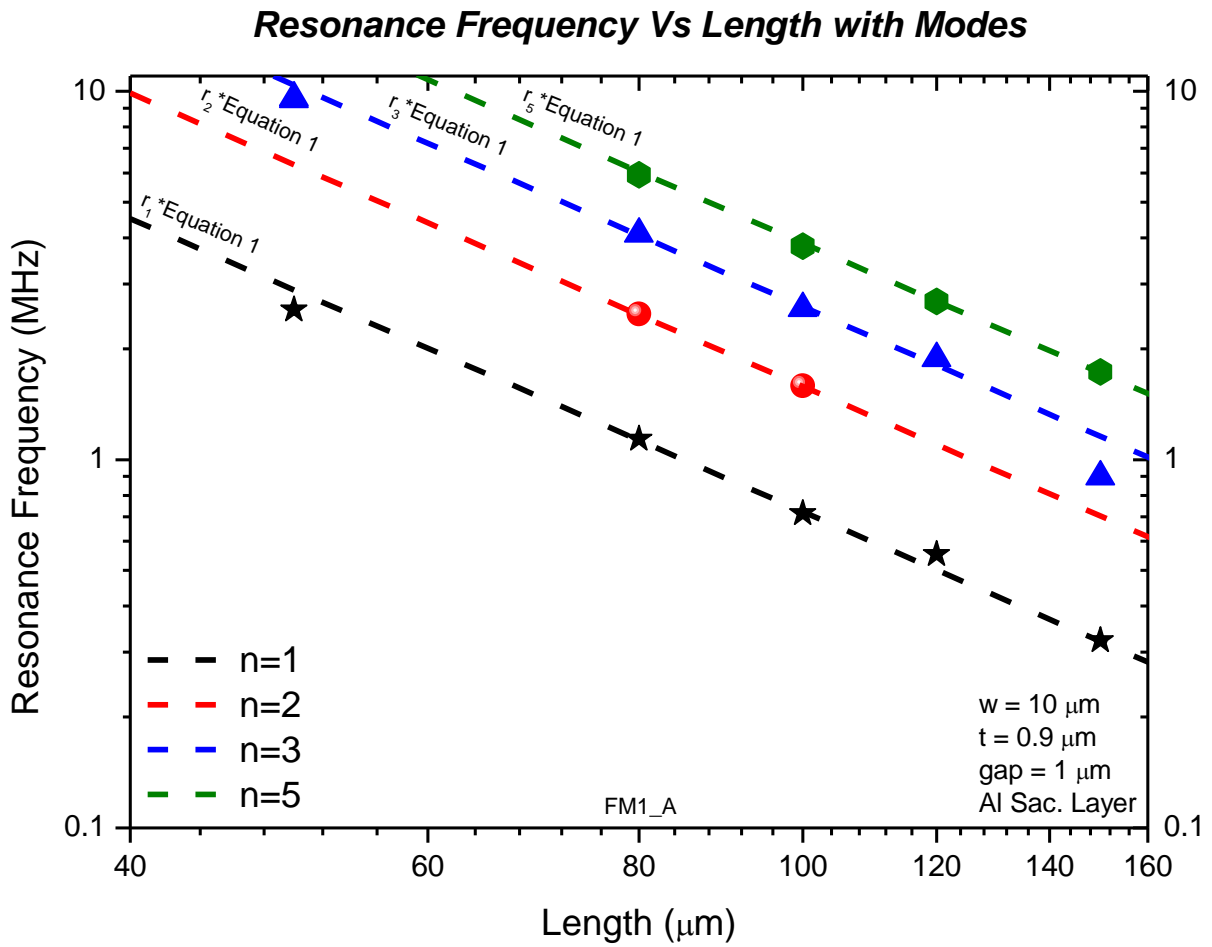
$$F_{res} (Hz) = r_i \left(\frac{t}{l^2} \right) \times \sqrt{\frac{E}{\rho}}$$

Equation 10 - Theoretical Resonance Frequency calculation using a_n coefficients

A device with several working structures with 50 μm to 150 μm in length, 10 μm of width, 0.9 μm of thickness and a gap of 1 μm between the gates and the bridges were measured. The sacrificial layer used was also Al. Graphic 4 shows the representation of the F_{res} as a function of the structures lengths, with the correspondent vibrational modes that were experimentally observed.

By analyzing this Graphic it is confirmed that the F_{res} of the structures demonstrates dependence with the square of their length. The ratios also are in agreement with the theoretical

results from [31], since these values are compatible with fixed bridges, for the structures measured in this work.



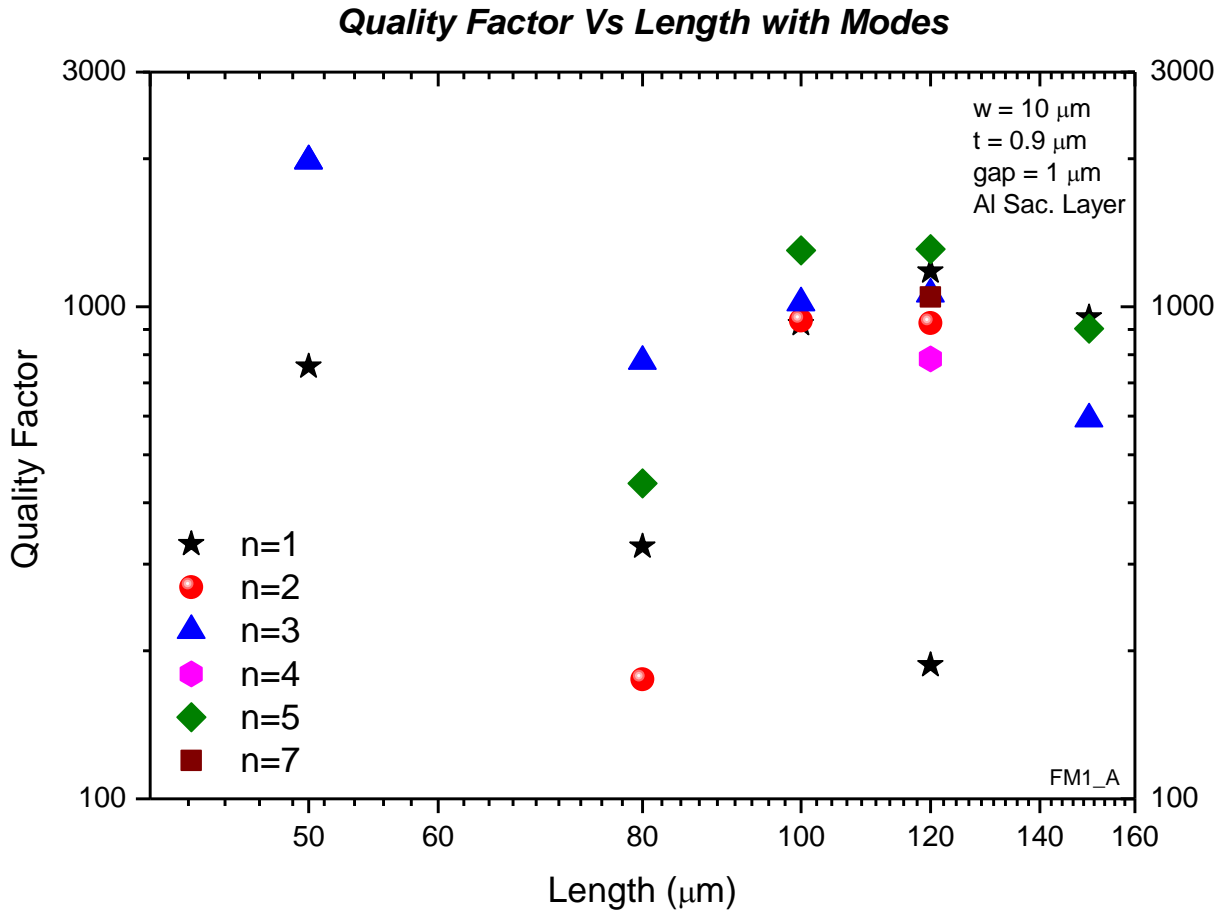
Graphic 4 - Resonance Frequency as a function of Length. $E = 150 \text{ GPa}$; $\rho = 2330 \text{ Kg/m}^3$; Pressure $\approx 10^{-2} \text{ Torr}$.

Table 7 shows the extracted ratio values for the structures measured in Graphic 4. The discrepancies in the values for different size structures are explain by experimental errors. The assumed ratio values used in Graphic 4 were from the 80 μm bridge.

		Length (μm)				
		50	80	100	120	150
Ratios	r_1	1	1	1	1	1
	r_2	-	2.19	2.22	-	-
	r_3	3.76	3.61	3.60	3.40	2.78
	r_5	-	5.22	5.31	4.86	5.36

Table 7 - Experimental ratio values

For those structures, the Q-factor was also extracted for the different modes, as demonstrated in Graphic 5.



Graphic 5 – Q-Factor as a Function of Length. $E = 150 \text{ GPa}$; $\rho = 2330 \text{ Kg/m}^3$; Pressure $\approx 10^{-2} \text{ Torr}$.

For this example, there is no apparent relation between the intrinsic Q-factor and the increase of the modes.

For the bridge of $120 \mu\text{m}$ which is the structure with the highest number of experimentally measured modes, it is visible that there are no major changes in the Q-factors corresponding to the different modes. With the exception of the bridge with $50 \mu\text{m}$ of length, the Q-factors seem to be higher for structures longer than $80 \mu\text{m}$ of length.

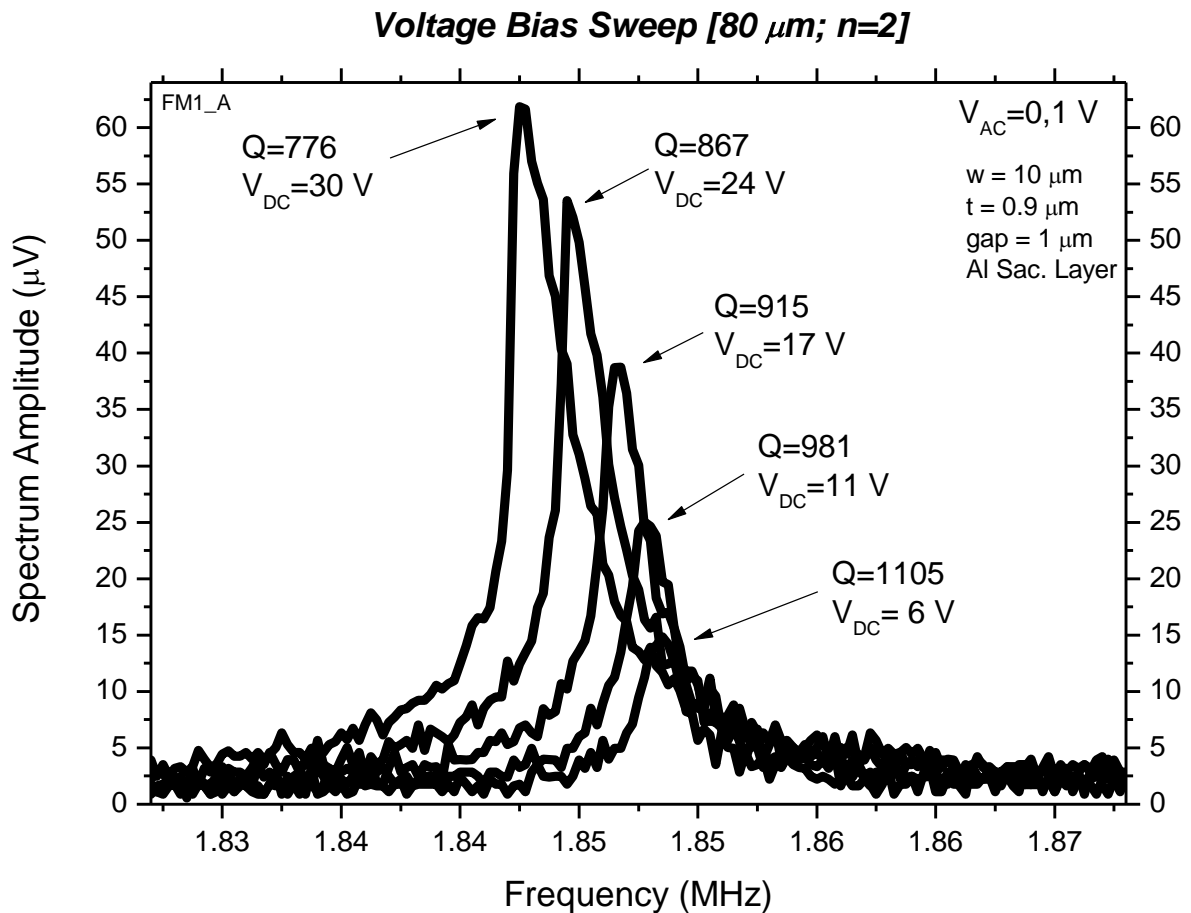
There are some advantages in investigating higher vibrational modes, due to their higher frequencies, which will be explained further on.

3.3. Voltage Bias Sweep

In order to characterize the nonlinearities of these MEMS devices, another set of measurements were made to several structures. The concept of voltage bias sweep consists on increasing the DC voltage applied to a given structure while maintaining a steady AC voltage, in order to understand the voltage limit to avoid nonlinearity regimes.

Due to the small size of MEMS devices, there is an inherent limitation on the stored energy and signal-to-noise ratio, which can impact the frequency stability of MEMS. In order to avoid this limitation of the output power it is possible to drive resonators into higher vibration amplitudes, which may cause the structures to operate in a nonlinear regime. The source of those nonlinearities can be classified as mechanical or electrical [33].

Graphic 6 shows a voltage bias measurement of the second vibrational mode of a bridge with 80 μm in length, 10 μm of width, 0.9 μm of thickness and a gap of 1 μm between the gate and the bridge. The sacrificial layer was Al.

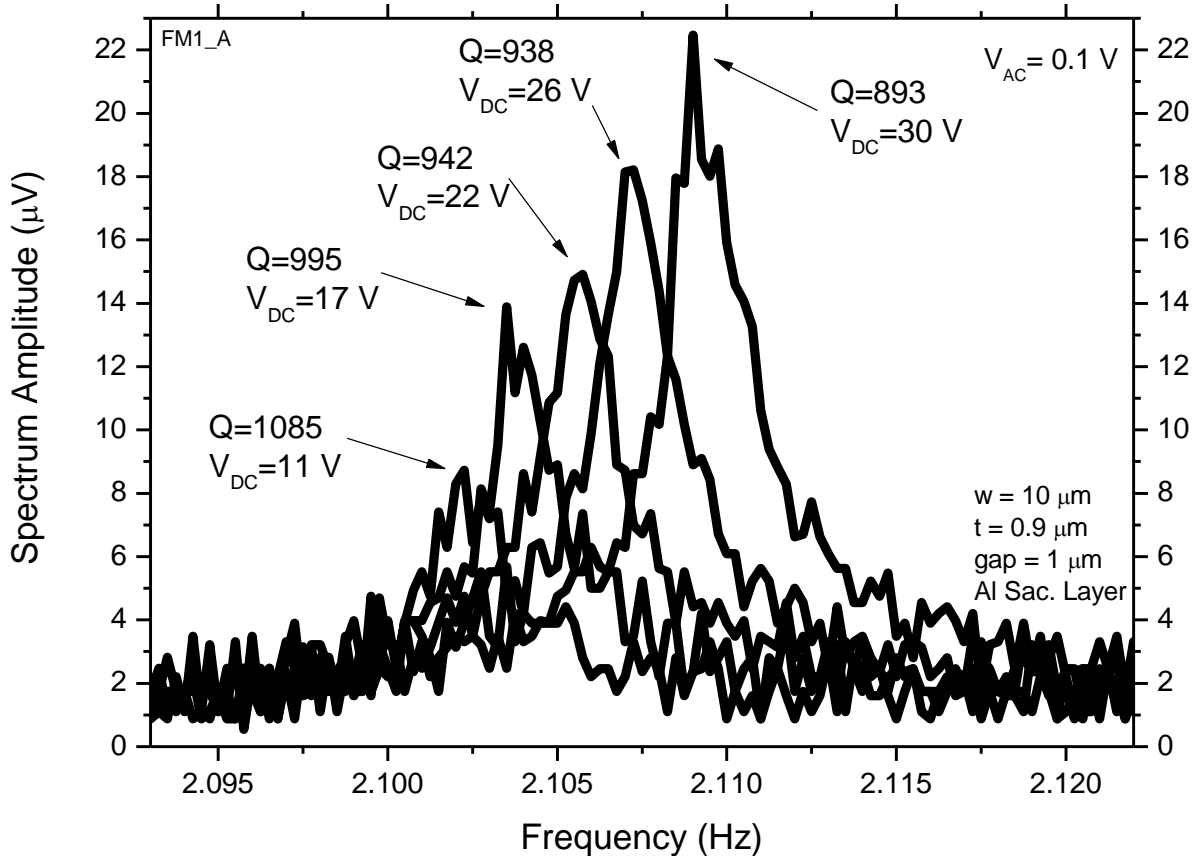


Graphic 6 – Electrical softening representation on an 80 μm bridge. $E = 150 \text{ GPa}$; $\rho = 2330 \text{ Kg/m}^3$; Pressure $\approx 10^{-2} \text{ Torr}$.

For this situation, the effective stiffness of the structure is smaller at high amplitudes due to electrical softening, causing a specific response of the structure leading it to progressively bend towards the lower frequency side, as the applied DC voltage increases [34].

Graphic 7 shows a voltage bias sweep measurement of the fourth vibrational mode of a bridge with 120 μm in length, 10 μm of width, 0.9 μm of thickness and a gap of 1 μm between the gate and the bridge. The sacrificial layer was Al.

Voltage Bias Sweep [120 μm ; $n=4$]



Graphic 7 – Mechanical stiffening representation on a 120 μm bridge. $E = 150 \text{ GPa}$; $\rho = 2330 \text{ Kg/m}^3$; Pressure $\approx 10^{-2} \text{ Torr}$.

For this structure, the extracted peaks bend towards higher frequency values as the DC voltage increases, due to the mechanical stiffening of the effective spring constant at higher amplitudes.

An intermediate effect combining the electrical softening and the mechanical stiffening discussed above can also be visible as shown in Graphic 8.

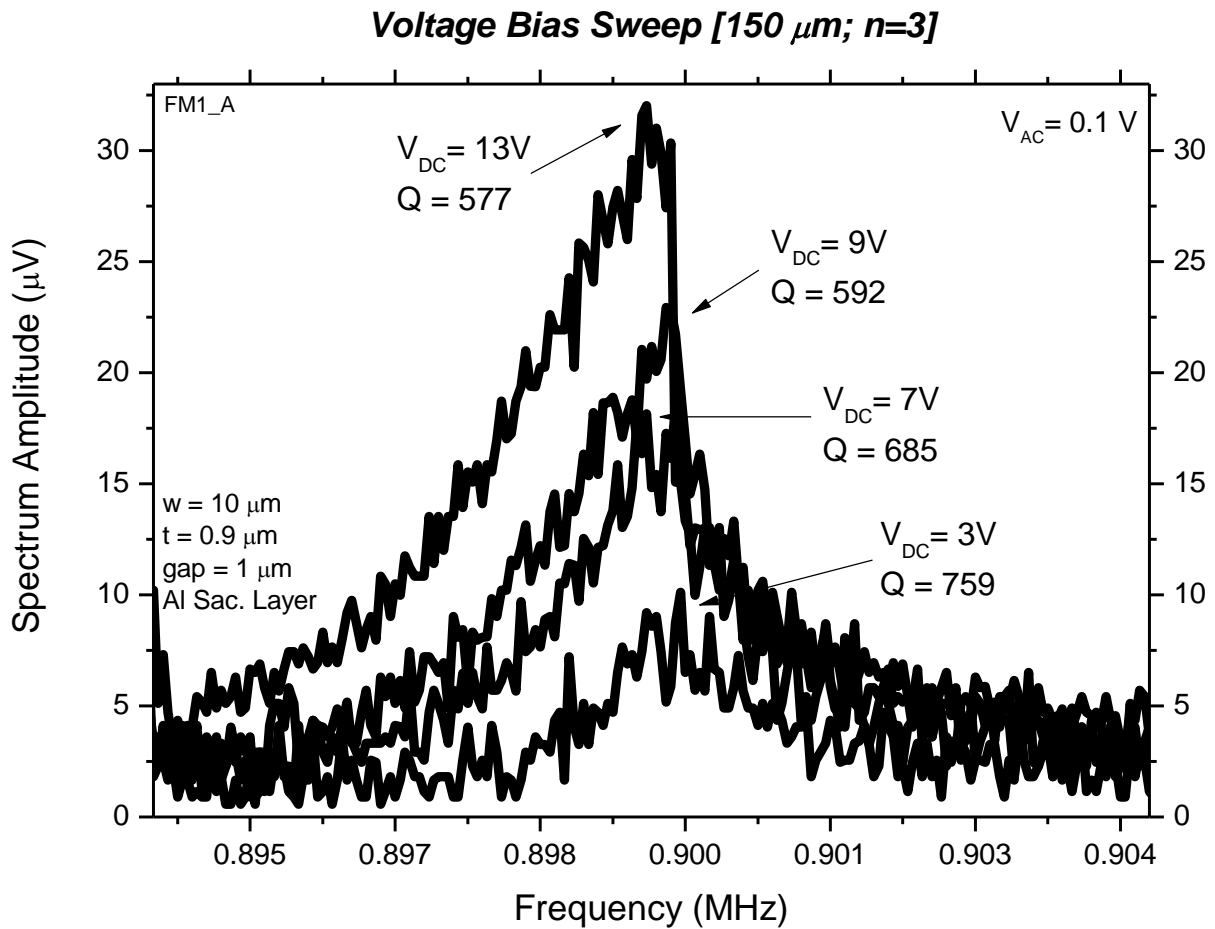
For intermediate voltages a combination between the mechanical and electrical effects can occur. For this particular structure, as amplitude increases, an electrical softening effect is visible to a certain point, followed by a mechanical stiffening effect, crossing a point at which their forces are balanced and cancel each other out.

Due to this alteration of the mentioned effects, some amplitudes of oscillation are present where the frequency dependence for small amplitude perturbations can be neglected [34].

Graphic 8 shows a voltage bias sweep measurement of the third vibrational mode of a bridge with 150 μm in length, 10 μm of width, 0.9 μm of thickness and a gap of 1 μm between the gate and the bridge. The sacrificial layer was Al.

For this structure, the voltage applied was considerably lower, since the resonance peak started to create a nonlinear aspect at 9 V. That effect is much clearer at 13 V, where the right side of the peak is not symmetric to the left side.

To avoid the destruction of the structure, the voltage bias sweep was stopped at that voltage.

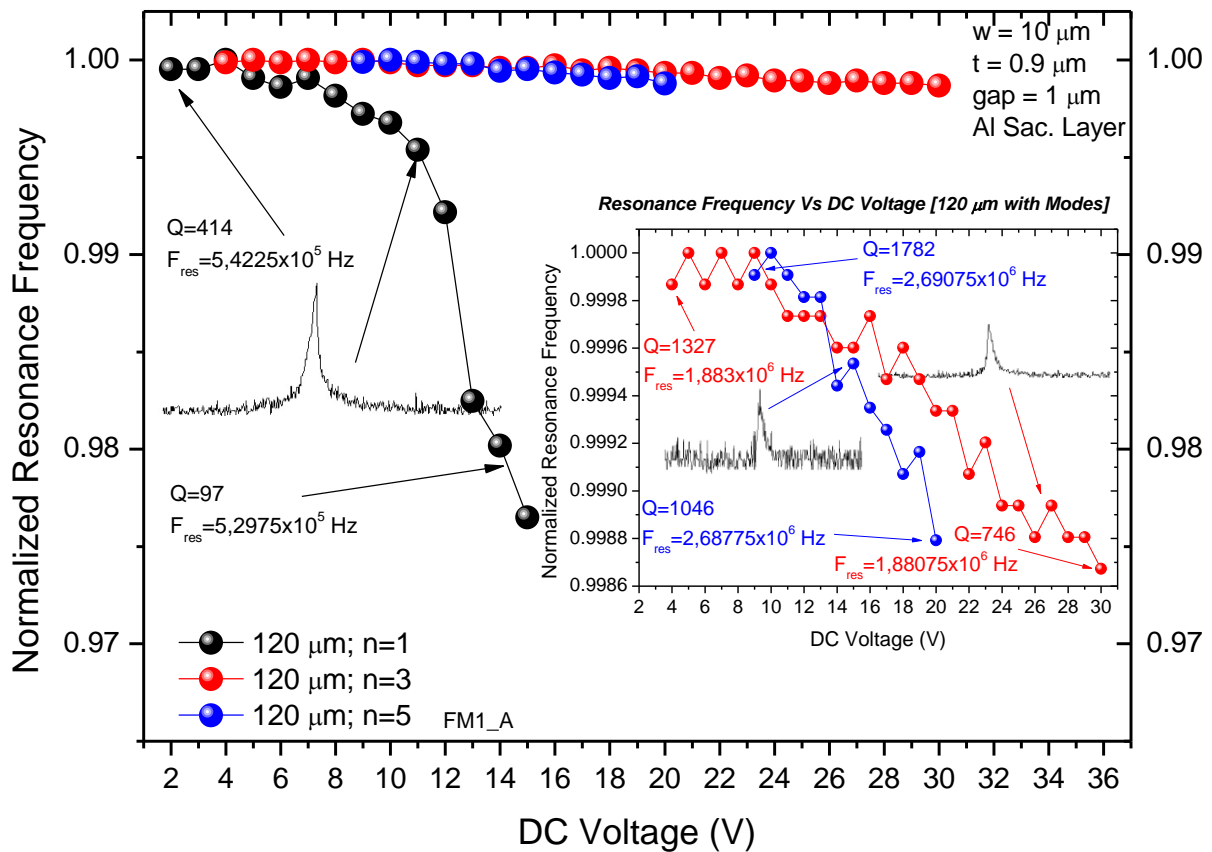


Graphic 8 – Intermediate effect representation on a 150 μm bridge. $E = 150 \text{ GPa}$; $\rho = 2330 \text{ Kg/m}^3$; Pressure $\approx 10^{-2} \text{ Torr}$

When comparing the voltage bias sweep measurements for different vibrational modes of the same structure, it is possible to conclude that, for the majority of the structures, with the increase of DC voltage a general mechanical stiffening effect can be considered for the whole range of applied voltages, meaning that the F_{res} will shift to higher values, even though there could be some electrical softening at certain voltages.

It also appears that there is no relation between the increase of voltage and the higher vibrational modes of a same structure. For example, for a vibrational mode between $n=1$ and $n=5$, it does not necessarily needs an applied voltage between the values used for the vibrational modes $n=1$ and $n=5$ in order to induce a F_{res} shift value that will be between the shifts of the vibrational modes $n=1$ and $n=5$, despite the practical analysis indicating that less DC voltage is needed only in the fundamental mode to induce a higher shift in the F_{res} of the structure, as it is demonstrated on Graphic 9. This represents the first, third and fifth vibrational modes of a structure with 120 μm in length, 10 μm of width, 0.9 μm of thickness and a gap of 1 μm between the gate and the bridge. It consists on the normalized by the maximum F_{res} as a function of the applied voltage.

Resonance Frequency Vs DC Voltage [120 μm with Modes]



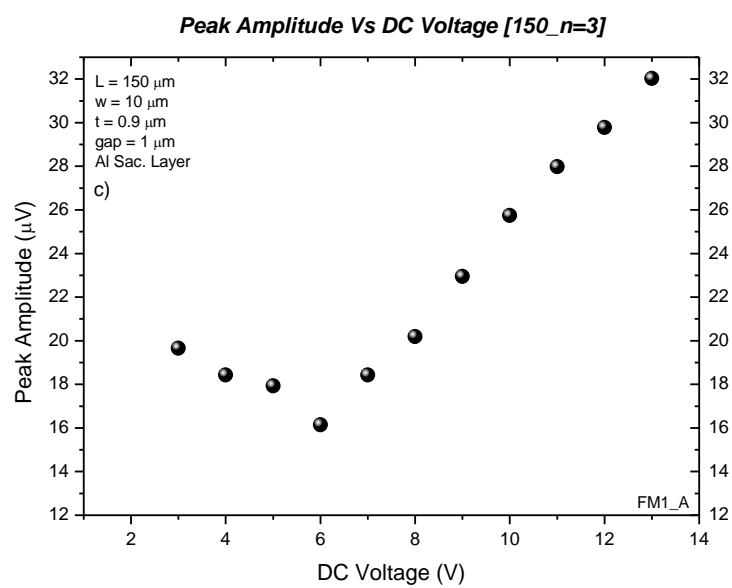
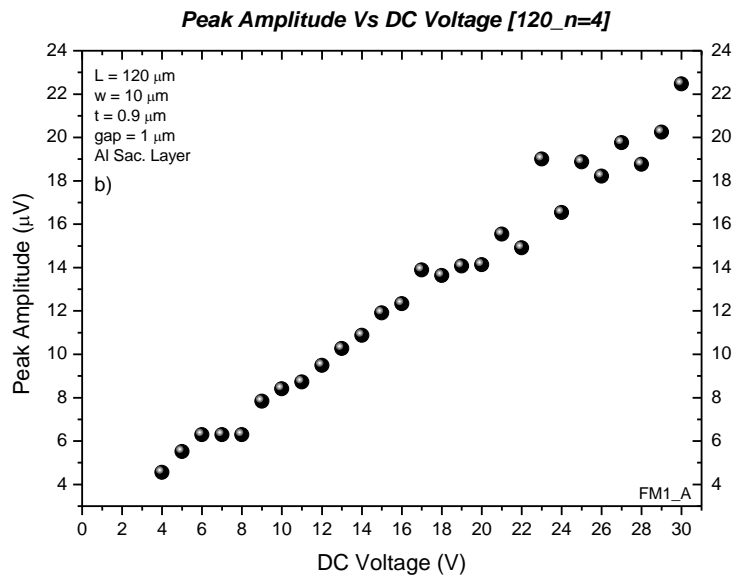
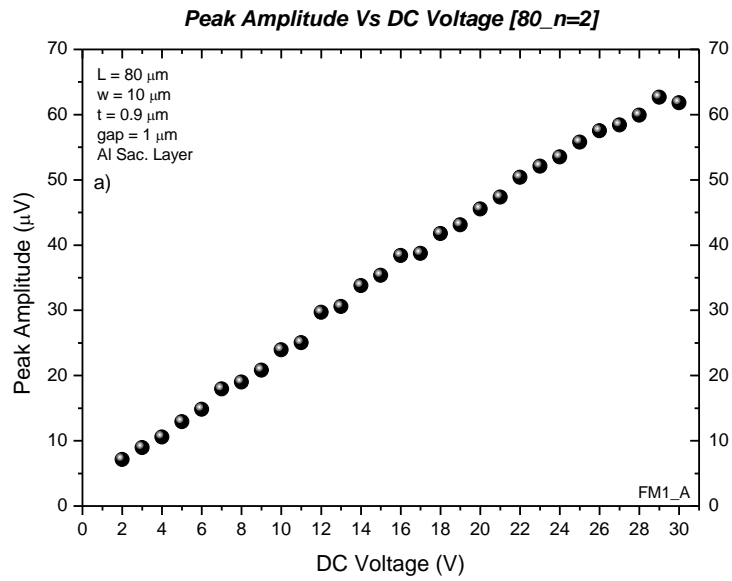
Graphic 9 - Comparison of vibrational modes with applied voltage, of a 120 μm bridge. $E = 150 \text{ GPa}$; $\rho = 2330 \text{ Kg/m}^3$; Pressure $\approx 10^{-2} \text{ Torr}$

Despite Graphics 6, 7 and 8 represent only a few resonance peaks at certain voltages, these measurements were performed with a range of applied voltages starting from the minimal DC voltage possible to extract a resonance peak, with an increase of 1 V for each measurement, reaching 30 V or until a visible nonlinearity of the resonance peak became visible.

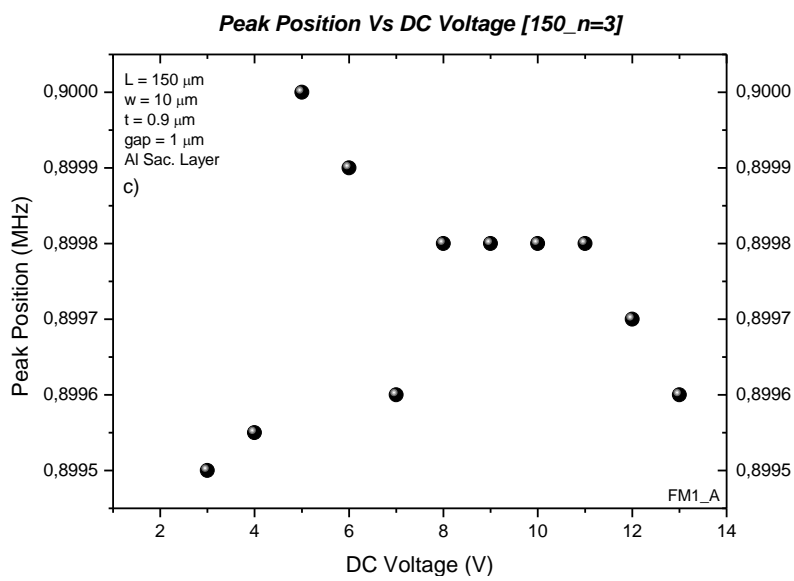
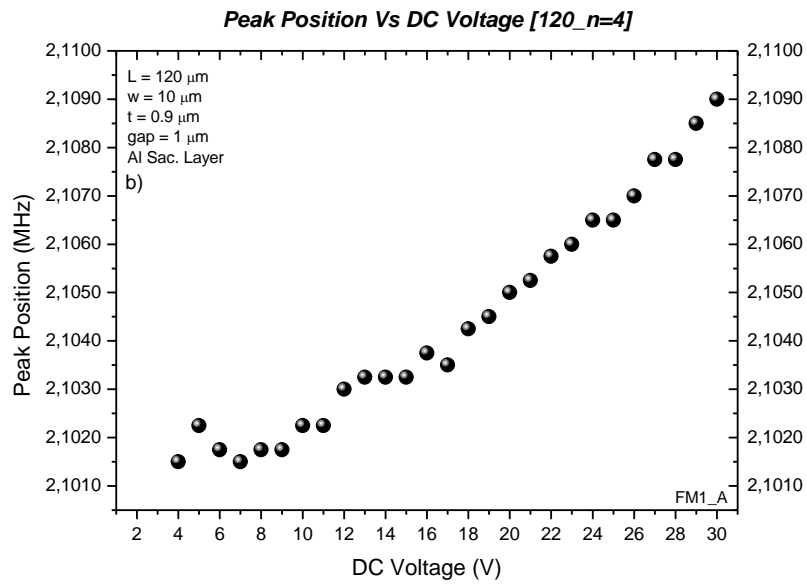
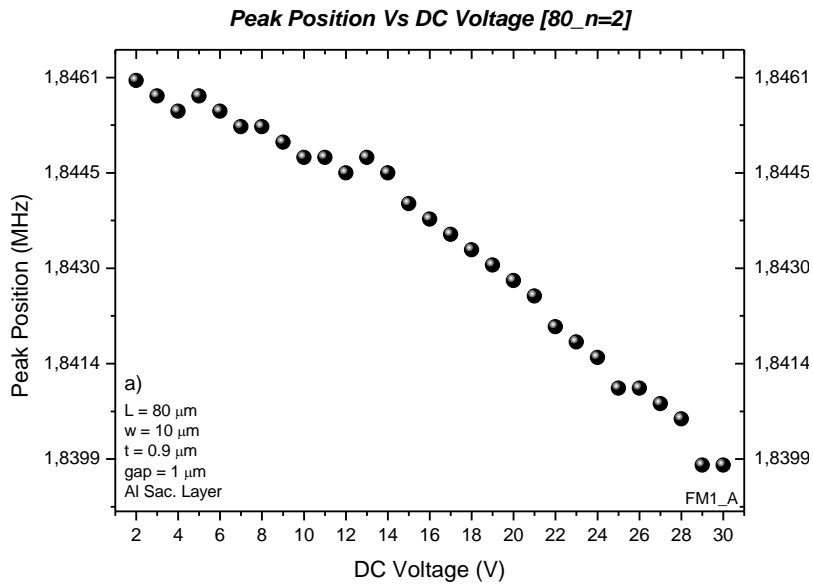
Graphic 10 represents the peak amplitudes as a function of the applied DC voltage demonstrating that by increasing that voltage the height of the peaks will generally increase thus decreasing the Q-factor of the structures.

Graphic 11 represents the position of the resonance peaks as a function of the applied DC voltage and represents three different effects, mechanical stiffening, electrical softening and an intermediate effect as discussed above. The 80 μm bridge presents electrical softening as its resonance peak shifts to lower frequencies (Graphic 11 a).

The 120 μm bridge is affected by mechanical stiffening since its resonance peak shifts to the higher frequencies (Graphic 11 b), while the 150 μm presents an intermediate effect since first electrical softening is visible and then mechanical stiffening is present as the applied voltage increases (Graphic 11 c).



Graphic 10 - Peak Amplitude as a function of Voltage. a) 80 μm bridge; b) 120 μm bridge; c) 150 μm bridge



Graphic 11 - Peak Position as a function of Voltage. a) 80 μm bridge; b) 120 μm bridge; c) 150 μm bridge

These conclusions are consistent with theoretical results from the damping free harmonic oscillator model, as it can be seen by solving Equation 11.

$$F_{res} = \sqrt{\frac{k}{m}}$$

Equation 11 - Theoretical Resonance Frequency calculation, using the spring constant [6]

Where:

- F_{res} – Resonance Frequency [Hz]
- k – Effective spring constant
- m – mass of the structure [Kg]

And:

$$k = k_{elast} + k_{elect} + k_{comp}$$

Equation 12 - Effective Spring Constant [31]

Where:

- k_{elast} – Elastic spring constant
- k_{elect} – deviation of the spring constant arising from the application of electrostatic forces
- k_{comp} – possible contribution of squeeze film air-damping compressive forces

Using these Equations, it is easy to verify that when the effective spring constant increases, the F_{res} of the structures also rises, meaning that we are in the presence of mechanical stiffening. The opposite is also true, if the effective spring constant decreases, so does the F_{res} , causing electrical softening. This is confirmed, by analyzing the results from Graphic 7 and 8.

Chapter 4 – Annealing Measurements

4.1. Introduction

One of the most ignored properties of the Q-factors of MEMS devices is their temperature dependence, despite the wide range of practical applications that may arise from an intense study focused on how temperature affects these devices. For instance, several applications for MEMS resonators such as mass sensors, frequency references or accelerometers, can be quite sensitive to temperature induced frequency shifts that can induce errors into their output frequency [35].

This study can be advantageous since the operating temperature of MEMS resonators for real applications can vary quite extensively as discussed in [36], where a local heater is used to achieve temperature control, and operating temperatures much higher than room temperature are suggested. Given that, it is important to confirm that high Q-factors will be available at elevated temperatures since it can be used as a direct measure of a resonators temperature if that Q-factor has strong dependence on temperature. This property can provide a direct measurement with minimum delay that can be for example an excellent sensor for closed-loop temperature control or even using the Q-factors as an absolute intrinsic thermometer for temperature compensation in MEMS [35].

Some of the known energy loss mechanisms in microscale resonators are losses due to chemical impurities, surface quality, intentional or unintentional surface coating, hydration and surface losses, which can be improved or avoided after the fabrication manufacturing processes [35] [37].

The effect of surface losses becomes more significant as the resonators are miniaturized and the surface to volume ratio increases. The surface of these resonators can have several lattice defects or imperfections, impurities or adsorbates that can induce energy dissipations. Some surface treatments, for instance annealing treatments, can minimize surface imperfections or impurities, thus dramatically increasing the Q-factor of the structures [35].

4.2. Annealing Characterization

These post-fabrication annealing measurements were performed to chips previously used for different experiments mentioned above containing structures with 40 to 200 μm in length, 20 μm of width, 2 μm of thickness and a gap of 0.6 μm between the gate and the bridge.

A Memmert Modell 400 heating oven was used to apply a temperature gradient to the chips, as demonstrated on Figure 21, in order to study the effects of that temperature in the Q-factor and F_{res} of the devices.

The chips were exposed to a range of temperatures from 100 $^{\circ}\text{C}$ to 250 $^{\circ}\text{C}$, with an increase of 25 $^{\circ}\text{C}$ for each cycle of temperature exposure, during a period of 30 minutes *per cycle*, so these chips were exposed to 7 different annealing temperatures, 100 $^{\circ}\text{C}$, 125 $^{\circ}\text{C}$, 150 $^{\circ}\text{C}$, 175 $^{\circ}\text{C}$, 200 $^{\circ}\text{C}$, 225 $^{\circ}\text{C}$ and 250 $^{\circ}\text{C}$. The room temperature was assumed to be 25 $^{\circ}\text{C}$ and the maximum temperature

of 250 °C was selected after some measurements reaching 275 °C showed that the structures were destroyed or the chips were badly burned.

Between each cycle, the chips were measured in vacuum according to chapter 3.1, after a 10 minutes period of cooling at room temperature.



Figure 22 – Memmert heating oven and chip inside oven

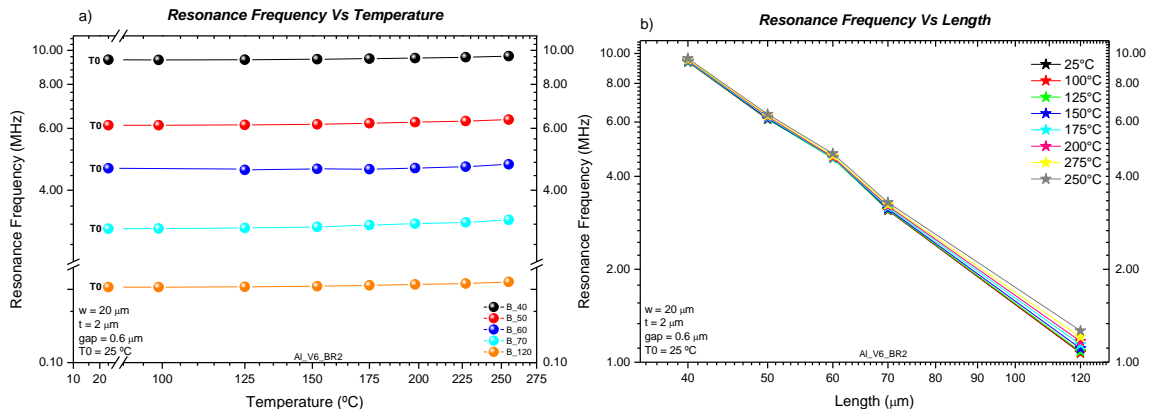
4.3. Annealing Results

The run of devices fabricated for the annealing experiments mentioned in Chapter 4.2 included several chips. One of the chips after being subjected to the annealing temperatures was characterized for the fundamental mode and regarding the F_{res} of its structures, it can be observed that there are no major shifts in those frequencies.

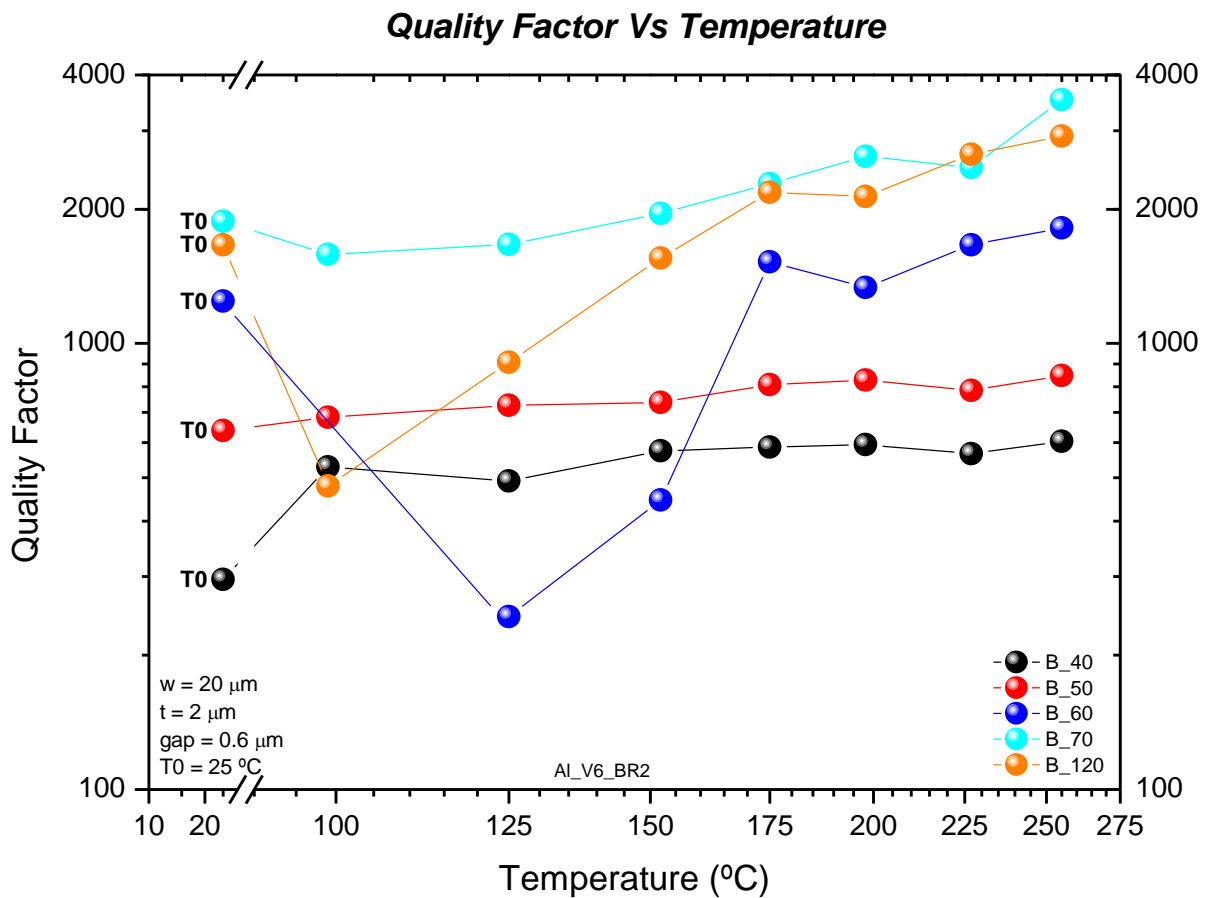
Graphic 12 a) demonstrates the F_{res} of the working structures as a function of the annealing temperature, while Graphic 12 b) the F_{res} of the working structures as a function of their length for the different annealing temperatures.

Despite the shift in the frequency of the structures being small, it appears to increase as the temperature rises for longer structures, as it can be seen in Graphic 12 b) for the bridge with 120 μm , which may indicate that for much higher annealing temperatures and longer structures, that shift may also increase significantly.

The Q-factor was also extracted for the fundamental mode of these structures and it is represented in Graphic 13.



Graphic 12 - Resonance Frequency as a function of a) Temperature and b) Length



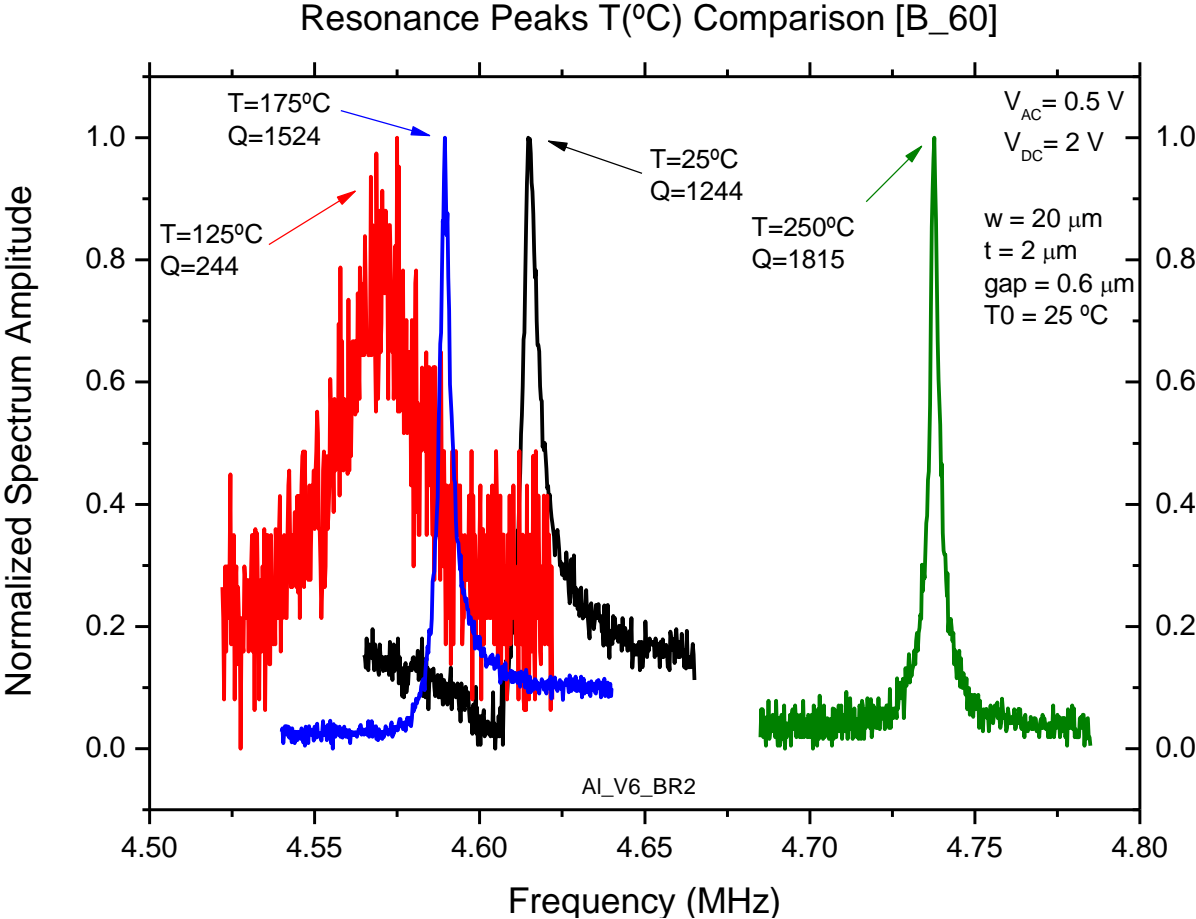
Graphic 13 - Quality Factor as a Function of the Annealing Temperature

After analyzing these preliminary annealing affected Q-factor results, it is clear that temperature significantly improves its value, thus reducing energy losses [37].

One could also reach a conclusion that, by looking at these results, there may be a certain threshold (for the results of Graphic 13, and merely speculative, $Q=1000$), where the Q-factors in the fundamental vibrational mode of the structures significantly decreases at lower annealing temperatures for initial Q-factors higher than 1000, and then significantly increases for higher

annealing temperatures, as opposed to structures with lower initial Q-factors were there are slight increases in their values for lower annealing temperatures, and the values for higher annealing temperatures are not that high when compared to what they initially were.

In Graphic 14 it is demonstrated the mentioned initial decrease of the Q-factor of a structure with 60 μm in length, where the black peak represents room temperature, and the red peak the behavior of the structure at a lower annealing temperature, followed by a gradual increase of the Q-factor value with the increase of temperature, shown by the blue peak, at 175 $^{\circ}\text{C}$ and then the green peak representing the last annealing step, corresponding to 250 $^{\circ}\text{C}$ reaching the highest Q-factor for this structure during this process. A shift in the F_{res} of the structure is visible however the major increase can only be considered significant, from much higher temperatures, hence the need to control the maximum temperature applied, to avoid the destruction of the structures.

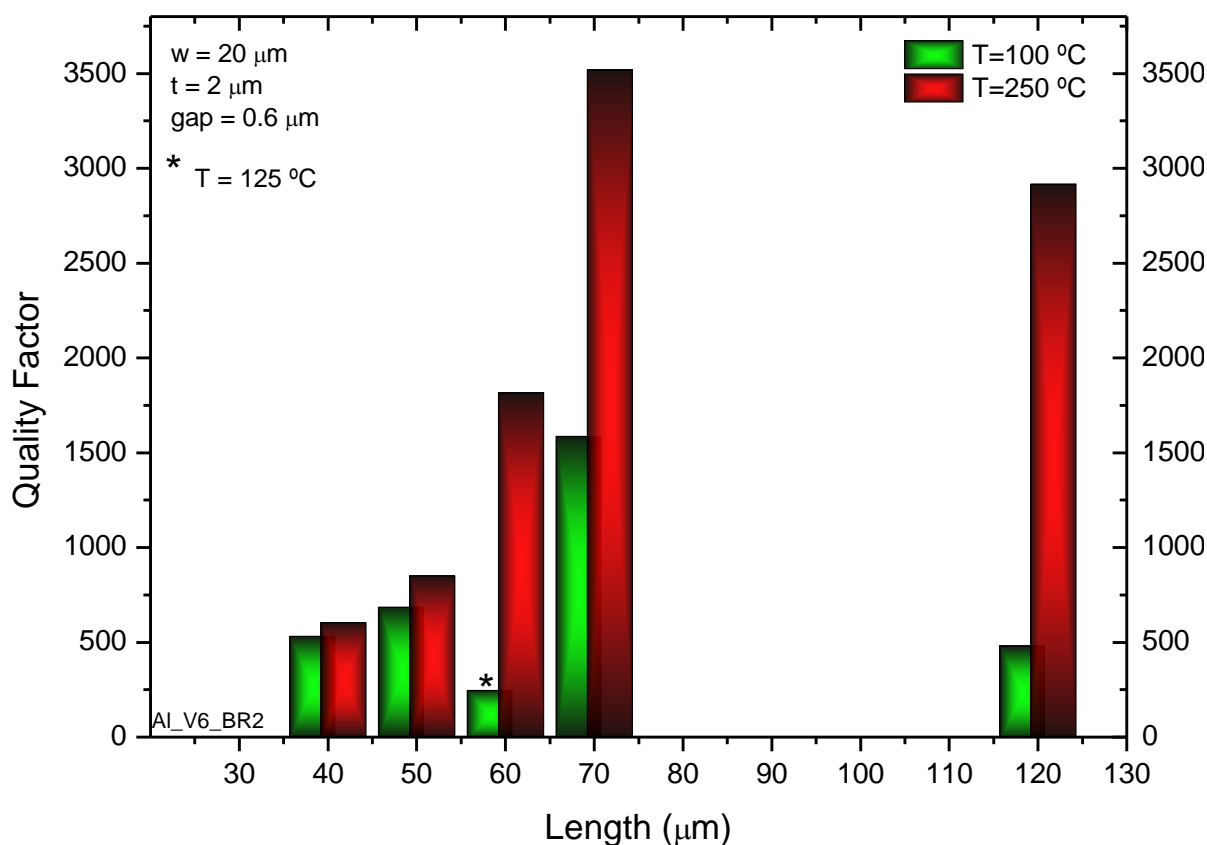


Graphic 14 - Resonance Peaks affected by Temperature for a 60 μm bridge

This hypothesis could also be considered for the length of the structures, were the shorter structures will be below this hypothetical threshold, while the longer structures will be above it.

Graphic 15 demonstrates in a more appealing manner this relation that the Q-factor has with the lower and higher annealing temperatures. The 40 μm and 50 μm bridges present lower increases in their Q-factors while the longer structures tend to significantly improve them.

Quality Factor Vs Length (T ($^{\circ}\text{C}$) Comparison)



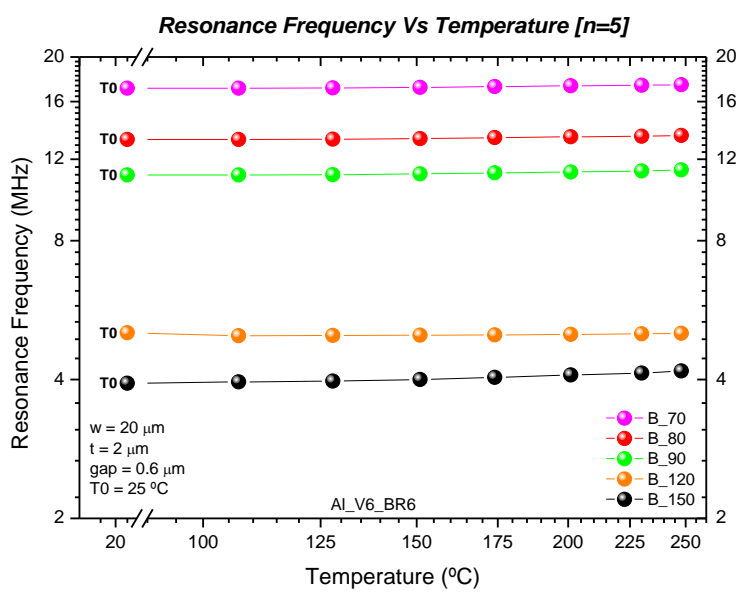
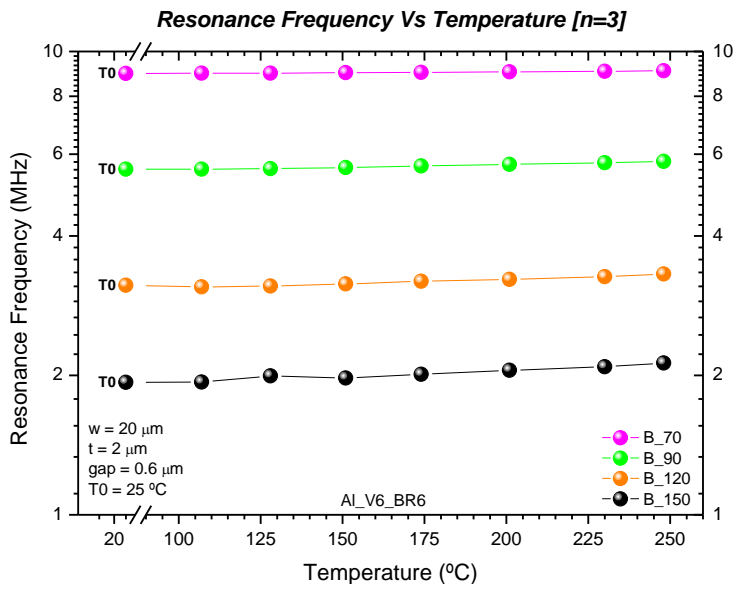
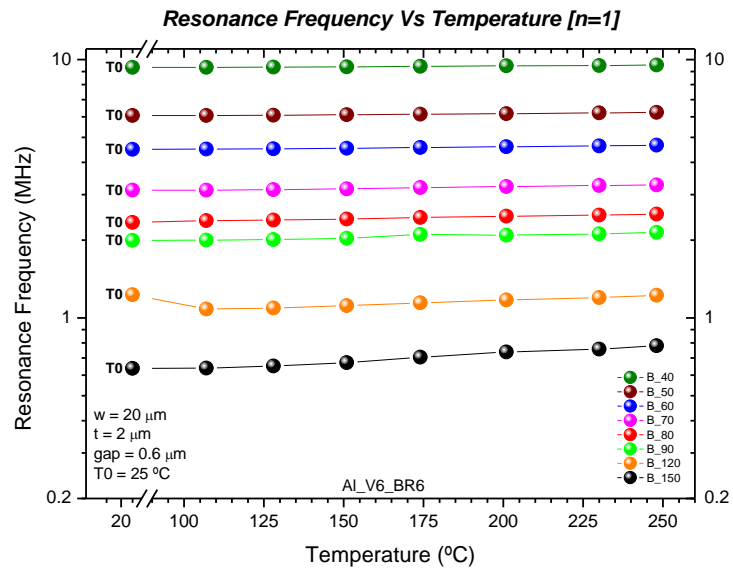
Graphic 15 - Annealing Temperature comparison of the Quality Factor as a function of Length

Another device from the same run with the same dimensions was also used for the annealing experiments in order to serve as a comparison with the previous device, and was also tested for different vibrational modes.

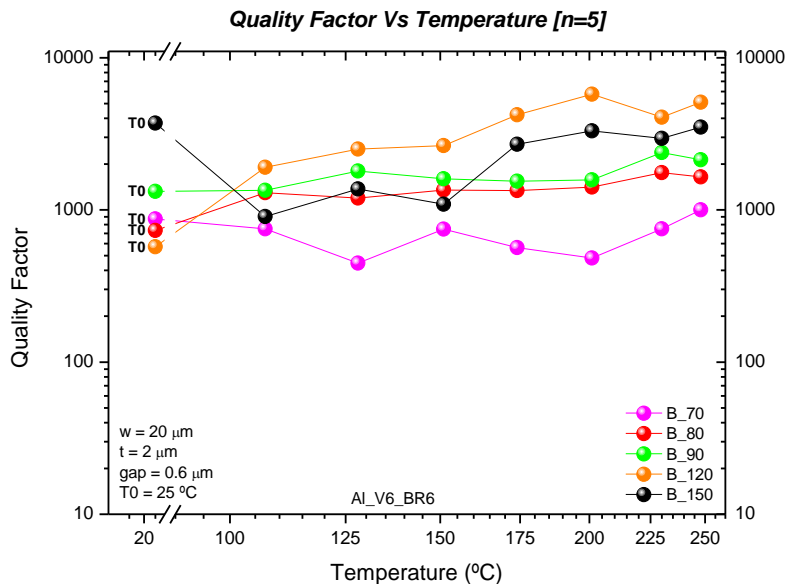
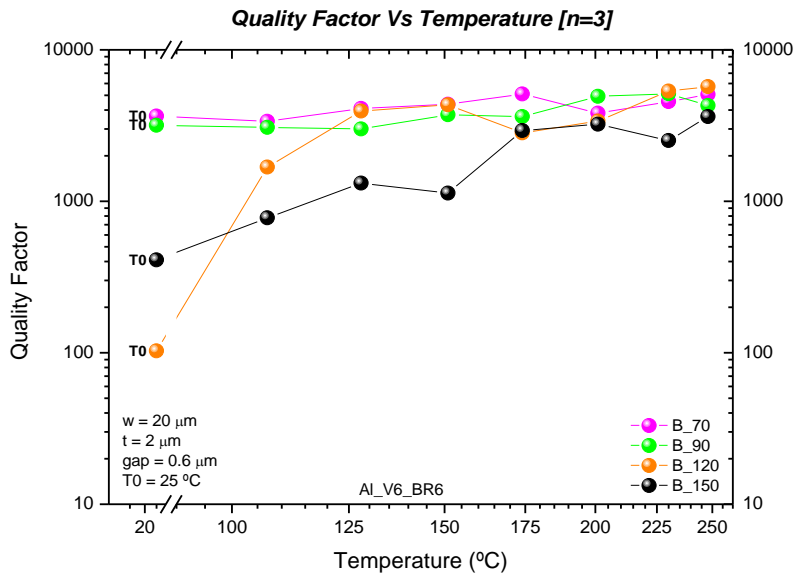
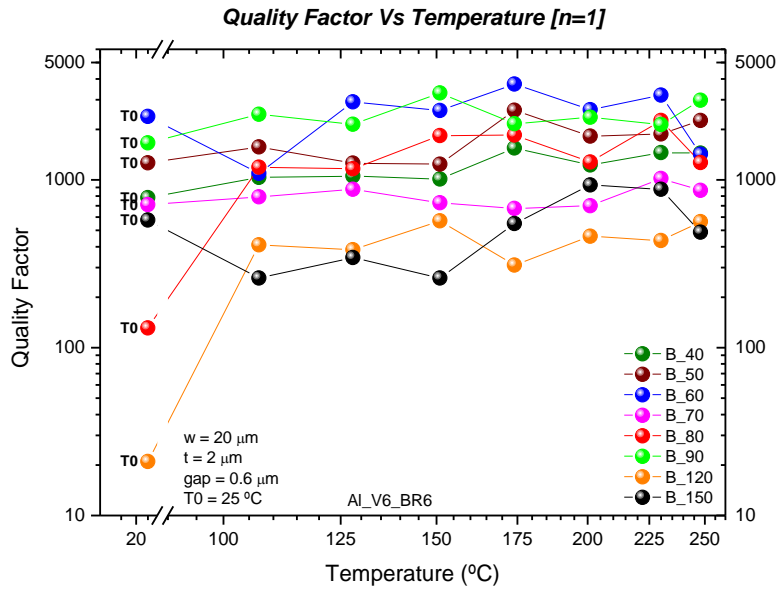
Graphic 16 shows the F_{res} of the working structures as a function of the applied annealing temperature and it demonstrates, just as the previous device did, that those frequencies do not present any accentuated shifts, whether the structures are shorter or longer. The same behavior is also truthful for both the third and fifth vibrational modes.

The Q-factor of the structures for the mentioned vibrational modes is represented in Graphic 17. Despite the Q-factor of some of the structures demonstrates the same behavior of the previous device regarding an initial decrease at lower annealing temperatures followed by an increase at higher temperatures, that behavior appears to be somewhat random thus compromising the idea of a threshold, mainly for the fundamental vibrational mode shown in Graphic 17.

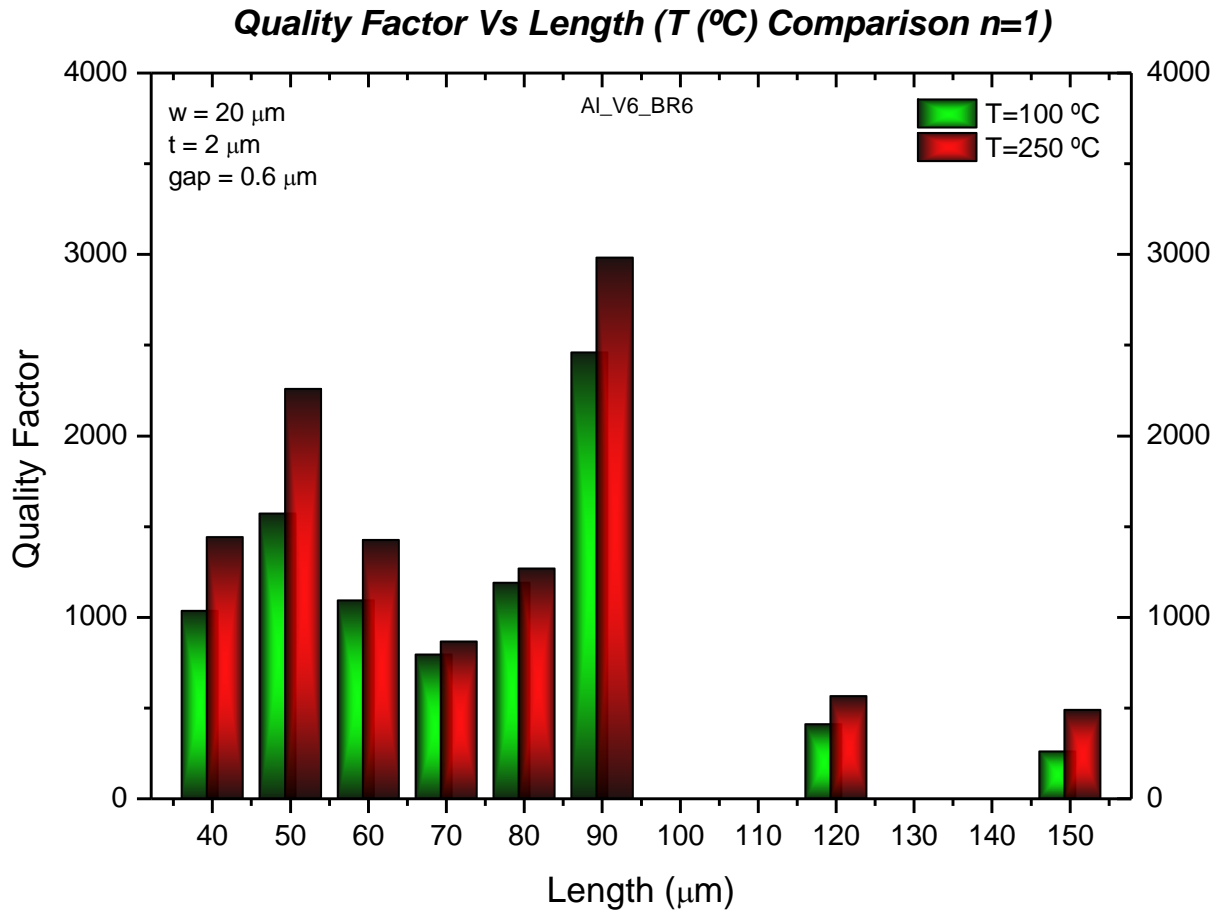
Graphics 17 and 18 show that the $60 \mu\text{m}$ and $150 \mu\text{m}$ bridges present that same initial behavior but their initial Q-factor values are considerably distant when compared to each other and their final values do not increase significantly. Nonetheless, these results lead to some interesting doubts that deserve a more extensive analysis and extra experiments to ascertain if there are any kind of unknown properties that Q-factors demonstrate when affected by temperature.



Graphic 16 - Resonance Frequency as a Function of temperature for the first, third and fifth vibrational modes



Graphic 17 - Quality Factor as a function of Temperature for the first, third and fifth vibrational modes



Graphic 18 - Annealing Temperature comparison of the Quality Factor as a function of Length for the fundamental mode

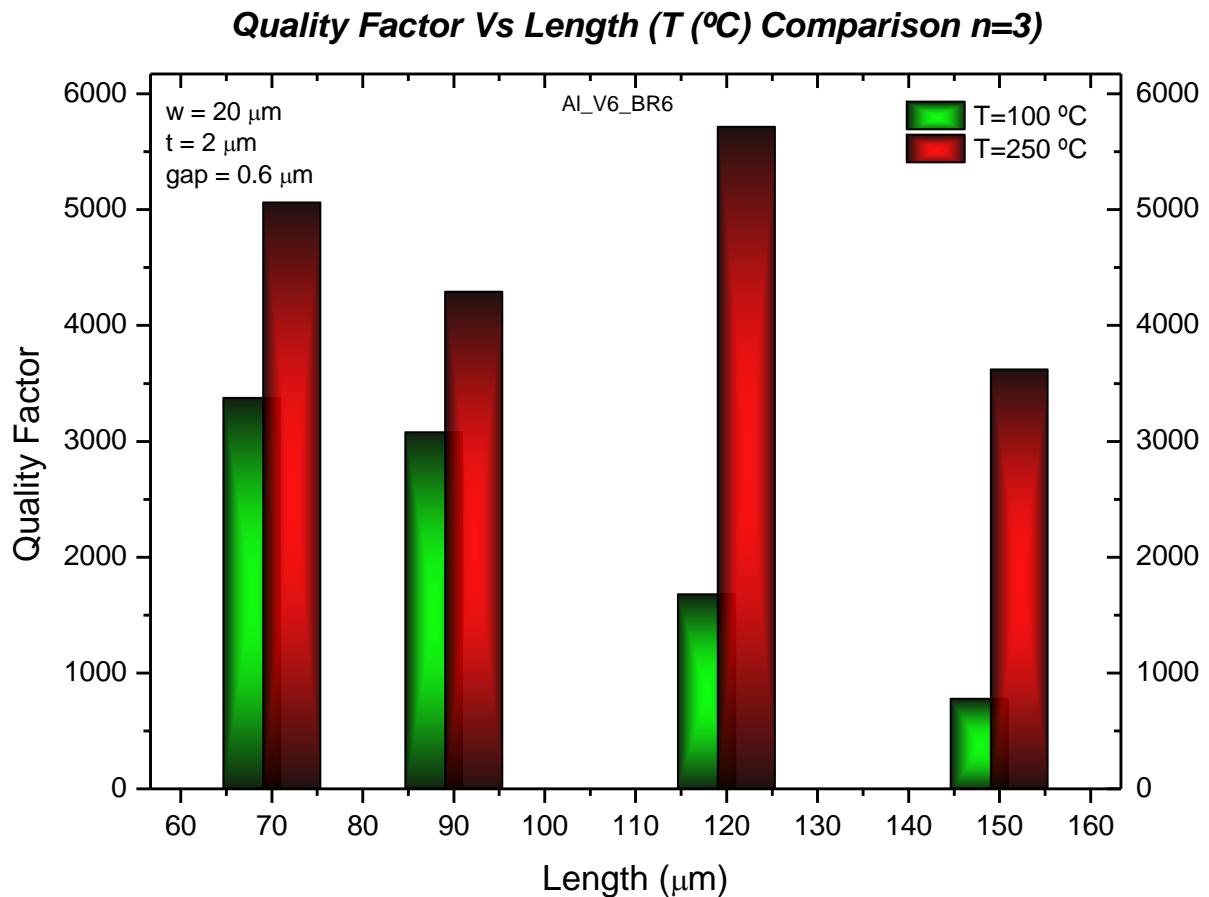
The experimental results for the third vibrational mode represented in Graphic 19 seem to indicate that the longer structures such as the 120 μm and 150 μm bridges tend to increase their Q-factors significantly even considering that their initial values were not that high.

For this vibrational mode the shorter structures were unmeasurable, so it was impossible to compare them with the previous results.

When analyzing the results from Graphic 13, it was discussed a possible threshold limit where the Q-factor of a given structure, typically a higher Q-factor, will decrease for lower annealing temperatures and increase significantly for higher ones. In that results, the threshold limit considered was $Q=1000$.

By looking at the results of Graphic 19, the 70 μm and 90 μm bridges possess Q-factor values at lower annealing temperatures higher than 3000, but a significant increase of those values is not present (if compared with the increases in the 120 μm and 150 μm bridges), similar to the results from Graphic 13.

This may indicate that, for higher modes, that threshold limit would be higher too, but further measurements should be done in order to confirm or not the presence of this limit.

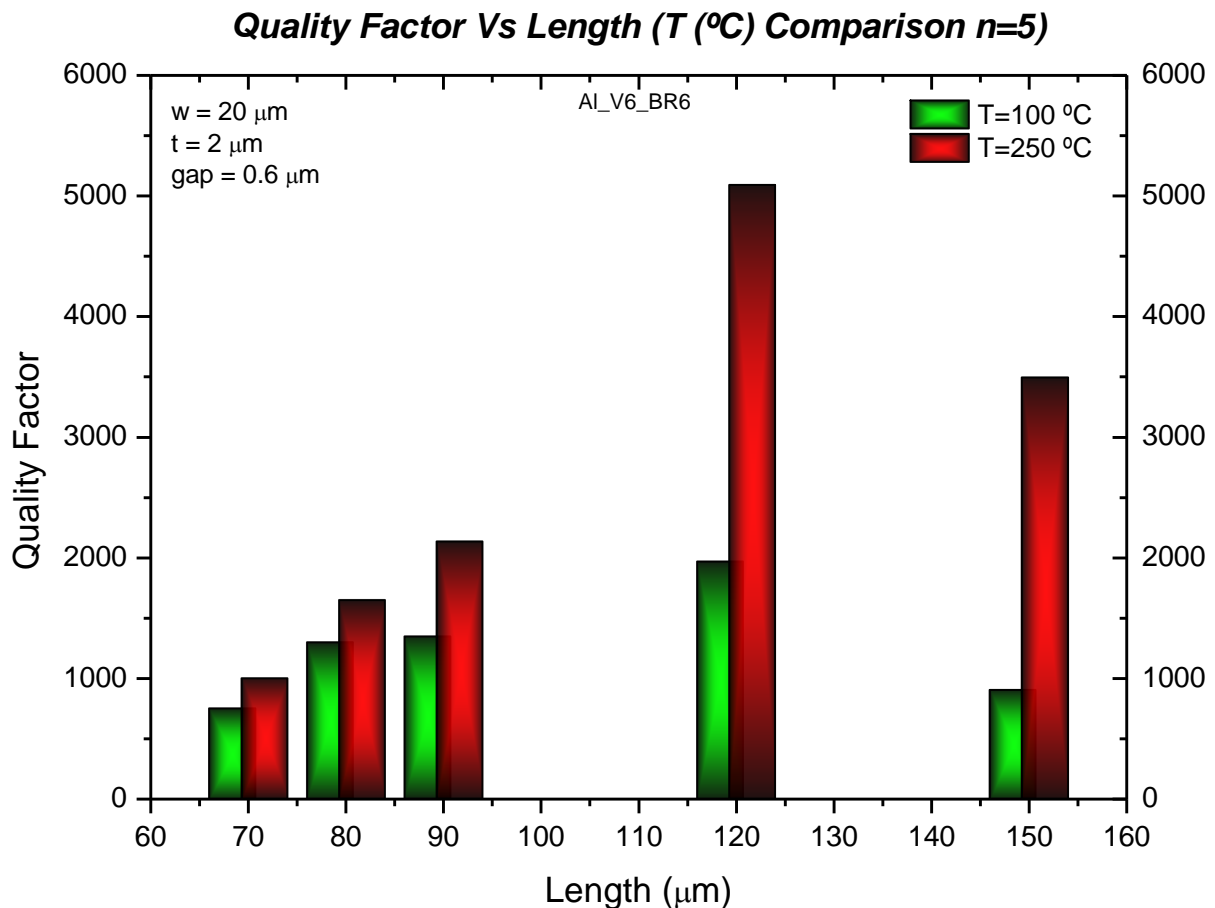


Graphic 19 - Annealing Temperature comparison of the Quality Factor as a function of Length for the third vibrational mode

The results from Graphic 20 representing the fifth vibrational mode of the same device are quite similar to the third vibrational mode.

One characteristic that seems to be common for the majority of the results, disregarding the results for the fundamental mode of this device which demonstrate similar improvements of the Q-factors for all of the structures lengths, is that the longer structures present higher increases in their Q-factors after being submitted to annealing temperatures up to $250\text{ }^{\circ}\text{C}$, whether their values at lower temperatures are $Q \approx 500$ or $Q \approx 2000$, despite the need to perform more experiments to validate if this is an acceptable conclusion.

One other aspect to have in mind is that the exposure of the structures to temperature tend to affect the general aspect of the resonance peaks causing some nonlinearities and, since the peaks are fitted to a Lorentzian curve, may lead to some discrepancies in the actual Q-factors of the structures.



Graphic 20 - Annealing Temperature comparison of the Quality Factor as a function of Length for the fifth vibrational mode

All of these results show that the Q-factors of the tested structures improved, regardless of their length and vibrational mode, when annealed at temperatures up to 250 $^{\circ}\text{C}$, thus confirming that annealing is a valid external technique that can be used to improve the Q-factor of any given MEMS resonator.

The reason why Q-factors increase when exposed to high temperatures is attributed to the characteristics of the devices at room temperature, where certain conditions such as the presence of water molecules which creates hydration in the surface of the structures, along with surface residues that occur during the process of fabrication, affect the way the devices operate, by lowering their Q-factors.

By annealing those devices water dehydrates, and the fabrication residues ashes out, thus improving the mentioned conditions [37].

It can be assumed that water adsorbed on the surface of the structures is one of the sources of surface dissipations, so the way to remove that adsorbed water is to bake the samples [38] in order to improve their Q-factors.

These annealing experiments can also be improved, since there were several factors that possibly affected the final results, hence the need of further measurements.

For instance, the devices were submitted to heat in a heating oven at atmospheric pressure, and then transported to the vacuum chamber shown in Figure 17, to extract the resonance peaks and correspondent Q-factors.

Since it was established that external factors such as hydration or fabrication defects affect the Q-factor, one can also suppose that dirt particles present in the surrounding air could also affect the structures, so the best solution will probably be to anneal the devices directly in the vacuum chamber to reduce to the maximum the surface dissipations.

Also, since the devices were extremely hot when removed from the oven, a period of cooling during 10 minutes was necessary, that could also bring the Q-factor values down. A setup that will allow for peak extractions while the devices are being annealed could also be advantageous.

4.4. Aging of MEMS

It is known that Si based MEMS are extremely attractive in a technological point of view due to the potential for reduced size, cost, power consumption and IC integration. The stability of the F_{res} of these devices over time is a main aspect to enable their use as a frequency reference, since it depends on the quality of the package environment [39].

Despite the size advantages of using MEMS resonators as a novel alternative there is still a concern regarding the increase of aging effects that derive from mass loading, package leaks or stress fatiguing [40].

Any given device such as these can present defects that will affect their mechanical properties and aging behavior, which can be introduced via RIE, annealing, dicing or wire bonding. Since MEMS systems can be applied to several fields such as aerospace, automotive or watch industry as mentioned before, it is imperative that the structure present high reliability, which induces a high demand in quality control and failure analysis [41].

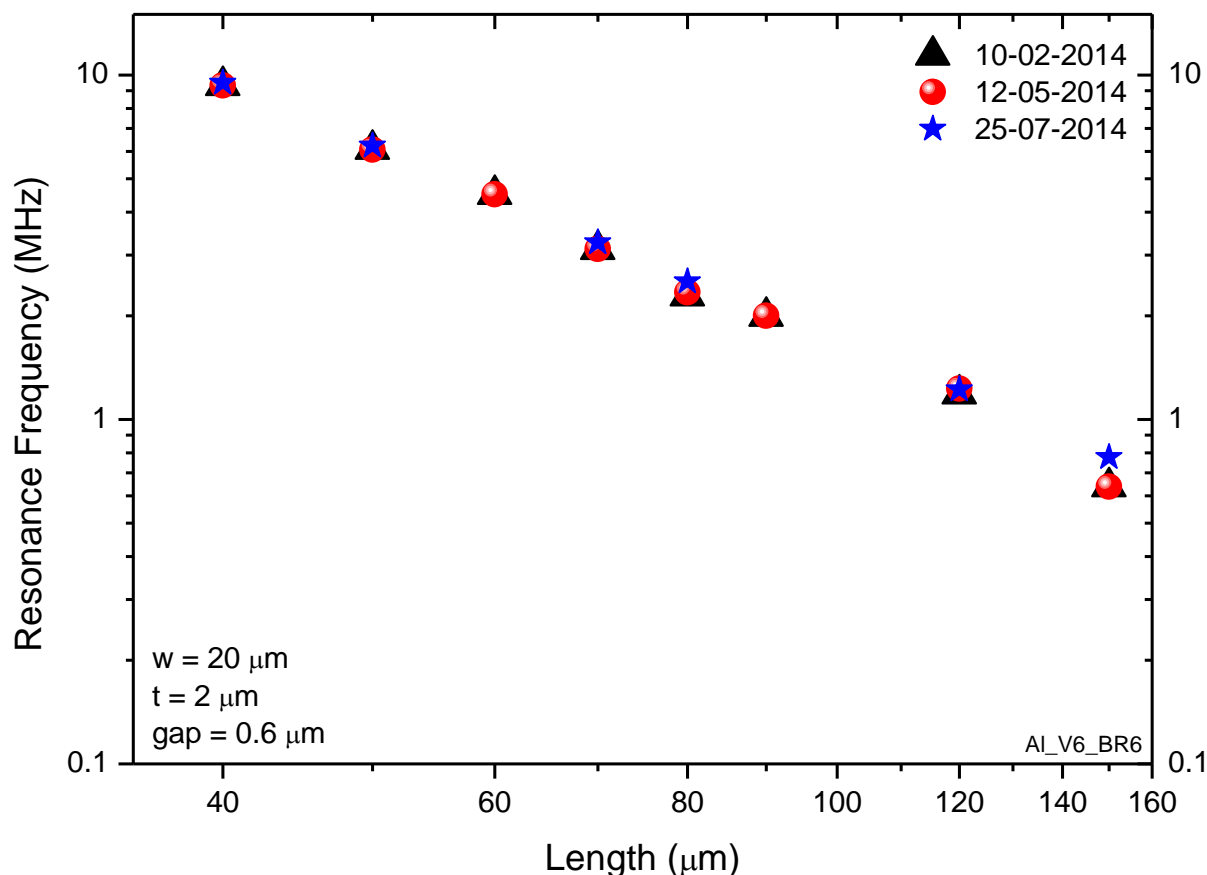
Typically, when these devices are used for applications such as radio communications for cell phones for instance, long-term frequency stability is essential and depends on the application to which they are being used [40], so it is important to study the devices previously. This consists on operating the devices during large periods of time, sometimes over a year, to verify if there are no major shifts in their frequency.

If these MEMS devices are to be used for biological applications, such as point-of-care diagnostics, it may also be important to test them during short periods of time, for several cycles. If it is a device to be used for this application, it will probably be used quit fast, and then turned off, several times, meaning it would not be operating during long periods.

The device used in Graphics 16 and 17 was measured for several experiments in this work, during a period of several months. In between those measurements, the F_{res} of the structures were measured three times, as it can be seen on Graphic 21.

By comparing their values, it is demonstrated that the structures do not present major shifts in their intrinsic F_{res} , during a period of around 5 months. These values correspond to measurements in vacuum.

Resonance Frequency Vs Length over time



Graphic 21 - Demonstration of the Resonance Frequency as a function of the Length of the structures for a period of around 5 months

During these measurements, the Q-factors of the structures were also extracted, as it can be seen on Graphic 22.

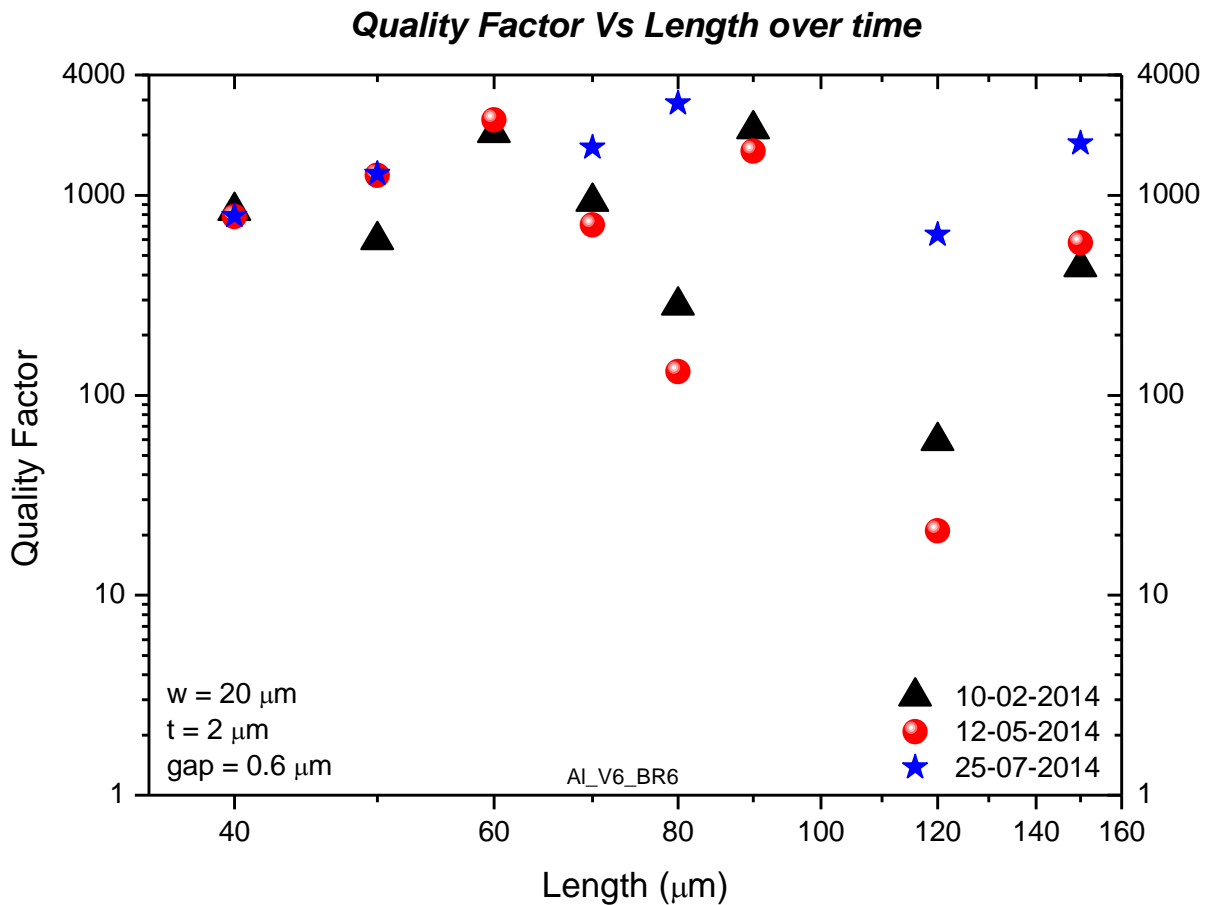
Most of the structures are still measurable after that period of 5 months, and for the majority of them, the Q-factors are relatively comparable. When these measurements were performed, the goal was not to compare them, just simply to see if they were still functioning so, small differences in the applied voltages can be verified, which may affect the extracted Q-factors, hence the differences in results for some of the structures. Despite that, the main reason why the Q-factors are significantly higher in the last measurement is that it was performed after the annealing process so, besides the increase of the Q-factors when temperature is applied, the structures can maintain those values for quite some time, since the last measurements were performed about a month and a half after the annealing process.

That being said, one other reason why there are visible differences in the Q-factors of some structures, can be attributed to the laser beam directed to them, which is positioned by the user, so it lacks precision, since in one measurement the laser can be pointed to one specific area, and in other measurement, it can be slightly shifted, deflecting in a different area of the structure.

The resonance peaks despite being in the same frequency position, can be interpreted by the network analyzer with a different geometry, generating a different Q-factor.

Despite that, the main focus here should be that the structures are still operational after a relatively long period of time.

Additional measurements can be done to future structures for longer periods of time and with this specific intent, to verify how long they will withstand maintaining fairly useful Q-factor values, along with minor shifts in their F_{res} .



Graphic 22 - Demonstration of the Quality Factor as a function of the Length of the structures for a period of around 5 months

Chapter 5 – MEMS Dissipation in air

5.1. Introduction

During the development of MEMS devices, it is of great importance to estimate the damping characteristics caused by several dissipative media in which these structures can operate.

This is an essential analysis since these characteristics will determine the dynamic performance of the system [42] [43].

Due to the fact that the process involving the supply of energy to microsystems presents challenges and it is a hard working operation, it is imperative to minimize the fraction of energy that is lost. In order to minimize these effects it is also important to take into account that most of microsensors or actuators use resonant vibration to enhance its sensitivity and the amplitude of their movement.

Several factors can be considered the cause for these damping effects, such as internal friction of the system, the support loss, airflow force in free space, and also squeeze force [43], depending on the media and the geometry of the structures.

Some MEMS devices are meant to operate in air, which can lead to some performance issues, where air damping is considered the most problematic energy loss mechanism [44].

Air damping can be defined as the influence of air in a given oscillating device that can reduce or prevent their oscillations. The excess of this effect can determine the performance of the components of a MEMS device [44].

It is well known that gravity and inertia that affect a given machine are proportional to the cube of their length, and viscous force is directly related to the square of the length [45]. The effect of these surface forces mentioned above can be considered negligible for a typical size machine, but that changes when the size of the structures becomes smaller, increasing the importance of that effect, due to an increase of the surface to volume ratio [46].

This effect leads to a situation where the motion of small size parts in a MEMS device becomes impaired due to the surrounding air, acting as a counter reactive force [45].

5.2. Pressure Characterization

As it was mentioned before, the Q-factor of a given MEMS device is dominated by energy losses. In order to obtain higher Q-factors and to avoid damping effects, these devices are typically operated at low pressures.

Some devices can have very high Q-factors in vacuum. When it is not possible or it is not the purpose of a certain project to operate the structures in vacuum, they must vibrate in certain gases such as air at different variable pressures that can vary from atmospheric to low vacuum [47].

Atmospheric pressure is a very important regime to operate MEMS structures for several applications, because some of them do not operate in the best conditions in vacuum environments. Since the damping effects of the gas or liquid media influences the Q-factor of a MEMS device, it is

important to study such alterations due to different media, when using these structures for biosensing [6].

When a vibrating structure interacts with the surrounding media, dissipation occurs which brings the Q-factor down.

Factors such as the gap between the gate and the bridge, or the fluid or gas pressure, can influence its motion that can range from continuum flow, transition flow or molecular flow [6] [47], depending on the specificities of the structures.

The fluid characteristics can be determined by the dimensionless parameter known as the Knudsen number, represented in Equation 13.

$$Kn = \frac{\lambda}{L}$$

Equation 13 - Knudsen number Equation [6] [47]

Where:

- λ – mean free path of the gas molecule
- L – solid body characteristic dimension

The Knudsen number is very small when considering a continuum flow and fairly big in the case of molecular flow [47], due to the increase of λ .

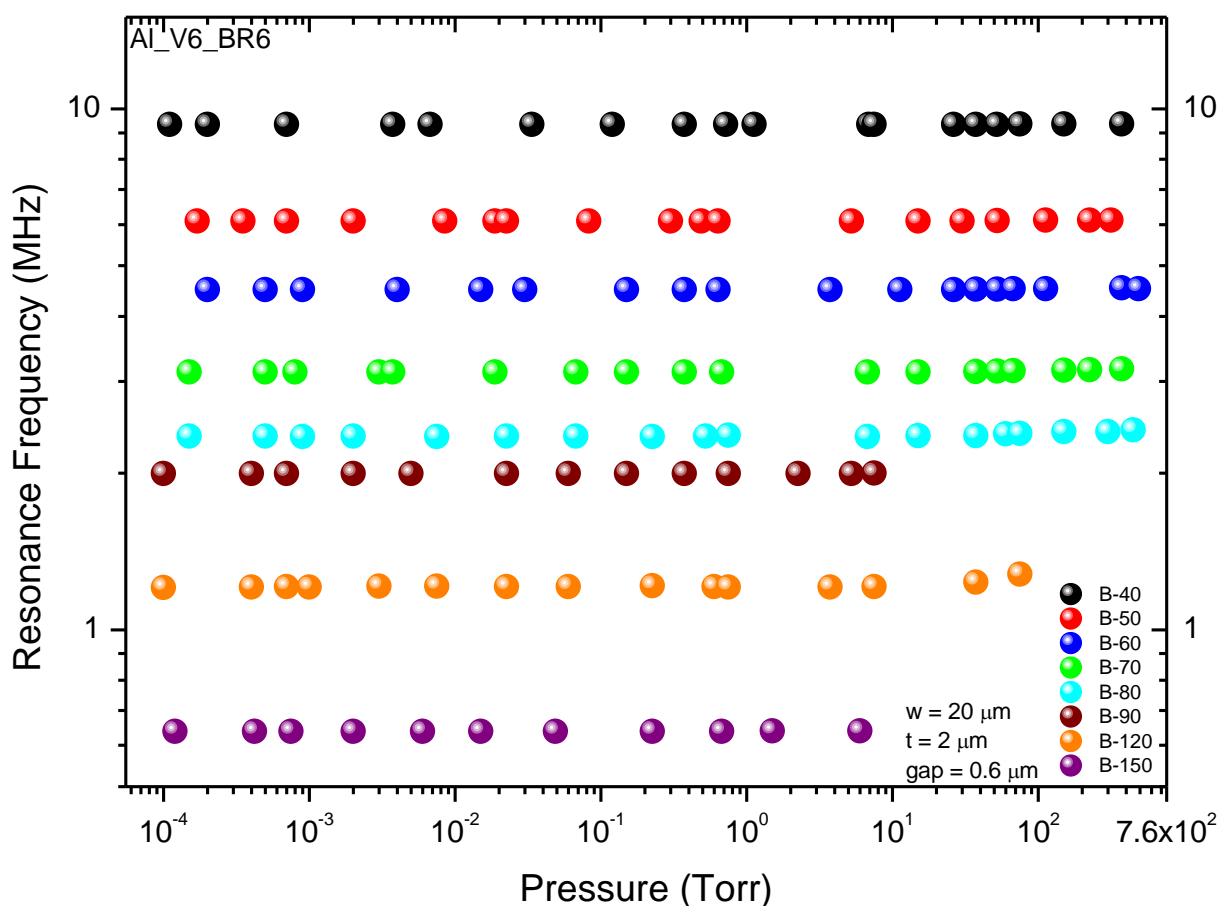
With this in mind, several measurements involving pressure were made, using the vacuum chamber in Figure 17.

The device used for this experiment contained bridge like structures with 40 μm to 200 μm in length, 10 μm of width and 2 μm of thickness. The gap between the bridges and the gates is 0.6 μm , and the sacrificial layer used in the microfabrication process was Al, which was one of the devices already characterized in Graphic 1.

This device was exposed to pressure from a range of 10^{-4} Torr to atmospheric pressure (760 Torr) at constant AC and DC voltages with the intent of determine the critical pressure (P_c), which is the pressure at which the Q-factor of the structure begins to degrade. At first, only the fundamental modes were measured when actuated at different pressures.

Regarding the F_{res} of the structures, Graphic 23 shows that there are no major shifts in any of the bridges even though some of the structures became unmeasurable before the pressure reached atmospheric values.

Resonance Frequency Vs Pressure

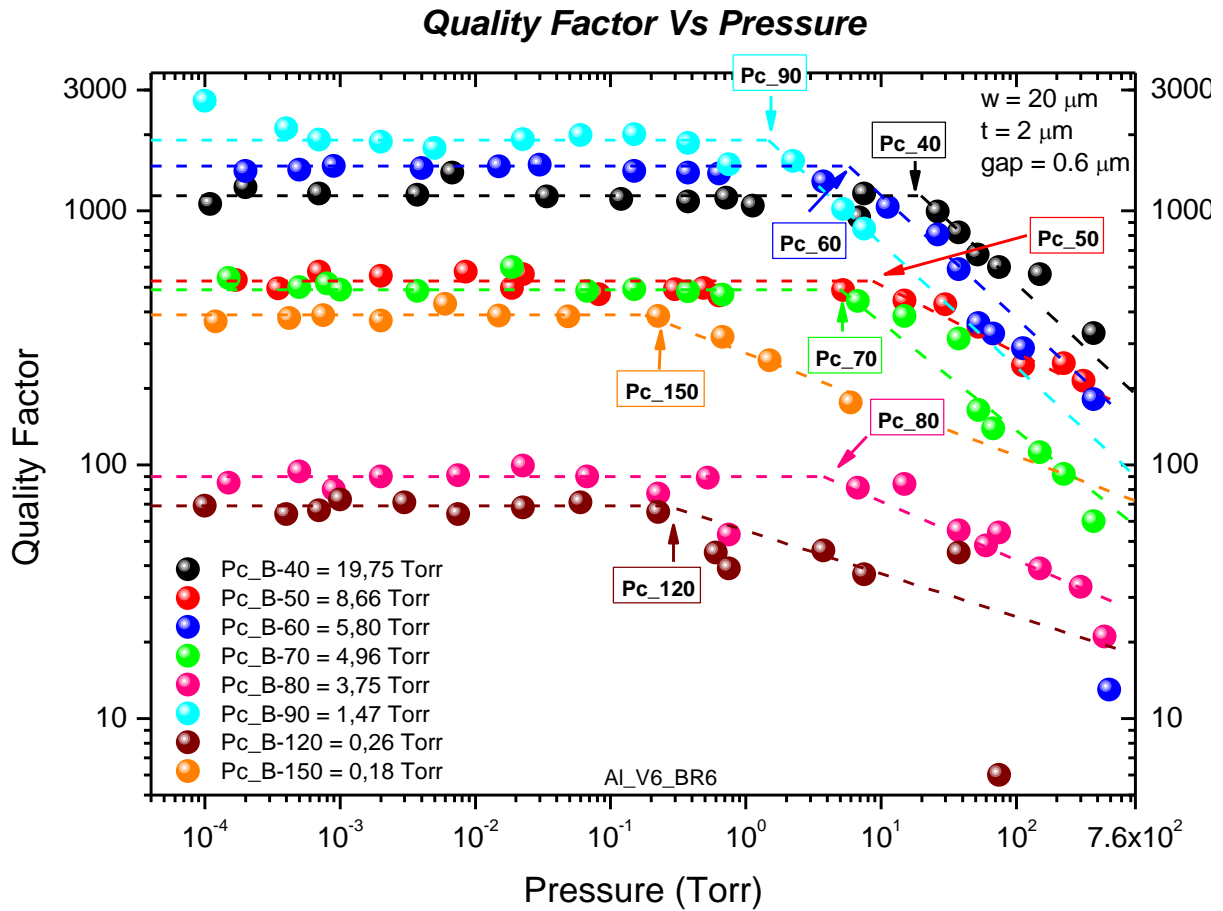


Graphic 23 - Resonance Frequency as a function of Pressure. $E = 150 \text{ GPa}$; $\rho = 2330 \text{ Kg/m}^3$

In order to understand the differences in flow regimes and to extract the P_c values, the Q-factors of the structures were plotted as a function of the pressure, represented in Graphic 24.

Regarding the $120 \mu\text{m}$ structure, the Q-factor values are quite random as pressure approaches atmospheric values. These results for this particular structure should be removed from the representation, but since the P_c is quite clear, it helps to maintain the results, to verify the differences of P_c with the size of the different structures.

For the lower pressure values there are no major Q-factor shifts corresponding to an air flow continuum like regime, where the Q-factors are dominated by intrinsic losses (TED, anchors, etc) as referred in Equation 5, demonstrating that the Q-factor value is the sum of their intrinsic and extrinsic values, since the damping from the medium is considered negligible [6] [47].



Graphic 24 - Quality Factor as a function of Pressure. $E = 150 \text{ GPa}$; $\rho = 2330 \text{ Kg/m}^3$

As it can be seen above, the critical pressure for the fundamental modes of the measured structures, range from 0.18 to 19.75 Torr.

Then, it seems that the Q-factors follow different power laws for different size structures.

For example, for the 50 μm , 80 μm , 120 μm and 150 μm length bridges the Q-factor appears to follows a power law $Q \propto P^{-1/2}$ corresponding to a viscous flow regime. For other structures like 40 μm , 60 μm , 70 μm and 90 μm in length, the Q-factors appear to depend inversely of the pressure, and the power law $Q \propto P^{-1}$ seems to be followed, corresponding to a free molecular flow regime due to momentum exchange with the individual gas molecules [6] [47]. The reason why the structures that present a free molecular flow regime and not a viscous flow regime is that it was not possible to measure at much higher pressures , otherwise it would be visible a change from the molecular flow to the viscous flow. The results also confirm that Q-factors are pressure dependent.

These results are supported by the theoretical Equations 14 for the viscous flow regime and 15 for the free molecular flow regime.

$$Q_{vis} \approx \frac{m_0}{6\pi\mu a^2} \sqrt{\frac{2RT\mu\omega_0}{MP}}$$

Equation 14 - Theoretical calculation of Q-factor in viscous flow regime [6]

Where:

- m_0 – Mass [Kg]
- μ – Viscosity of the fluid [$Kg/m \cdot s$]
- a – characteristic linear dimension
- R – Ideal gas constant
- T – temperature [K]
- ω_0 – Angular Resonance Frequency [rad/s]
- M – Molecular mass of the gas medium [u]
- P – Pressure [Pa]

$$Q_{FMF} = \left(\frac{\pi}{2}\right)^{\frac{3}{2}} \rho_r h \frac{\omega}{2\pi} \sqrt{\frac{RT}{M} \frac{1}{P}}$$

Equation 15 - Theoretical calculation of Q-factor in the free molecular flow regime [6]

Where:

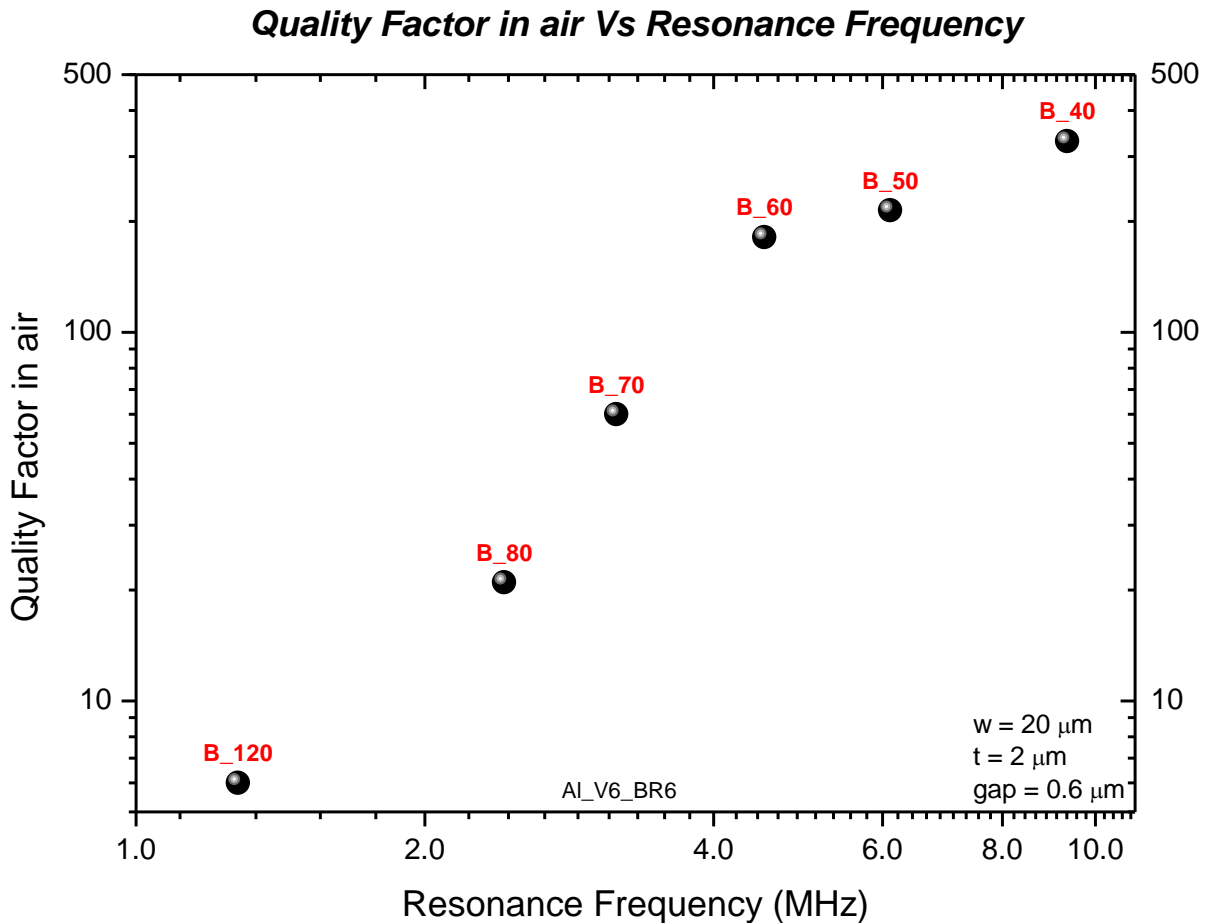
- ρ_r – Mass density [Kg/m^2]
- h – Thickness [m]
- ω – Angular Resonance Frequency [rad/s]

Graphic 24 also demonstrates that the structures with lower intrinsic Q-factors are typically more difficult to measure as the pressure approaches atmospheric values, since the resonance peaks become very unstable and the Q-factors are very small.

In some cases, those values are unmeasurable even before the pressure reaches atmospheric values.

The same measurements were made for the third and fifth vibrational modes of the structures above, with similar results regarding the F_{res} of the structures which presents no relevant frequency shifts, and also with the same behavior for the air flow regimes.

In Graphic 25 the relation between the Q-factors of the structures that are measurable at atmospheric pressure is represented as a function of their F_{res} .



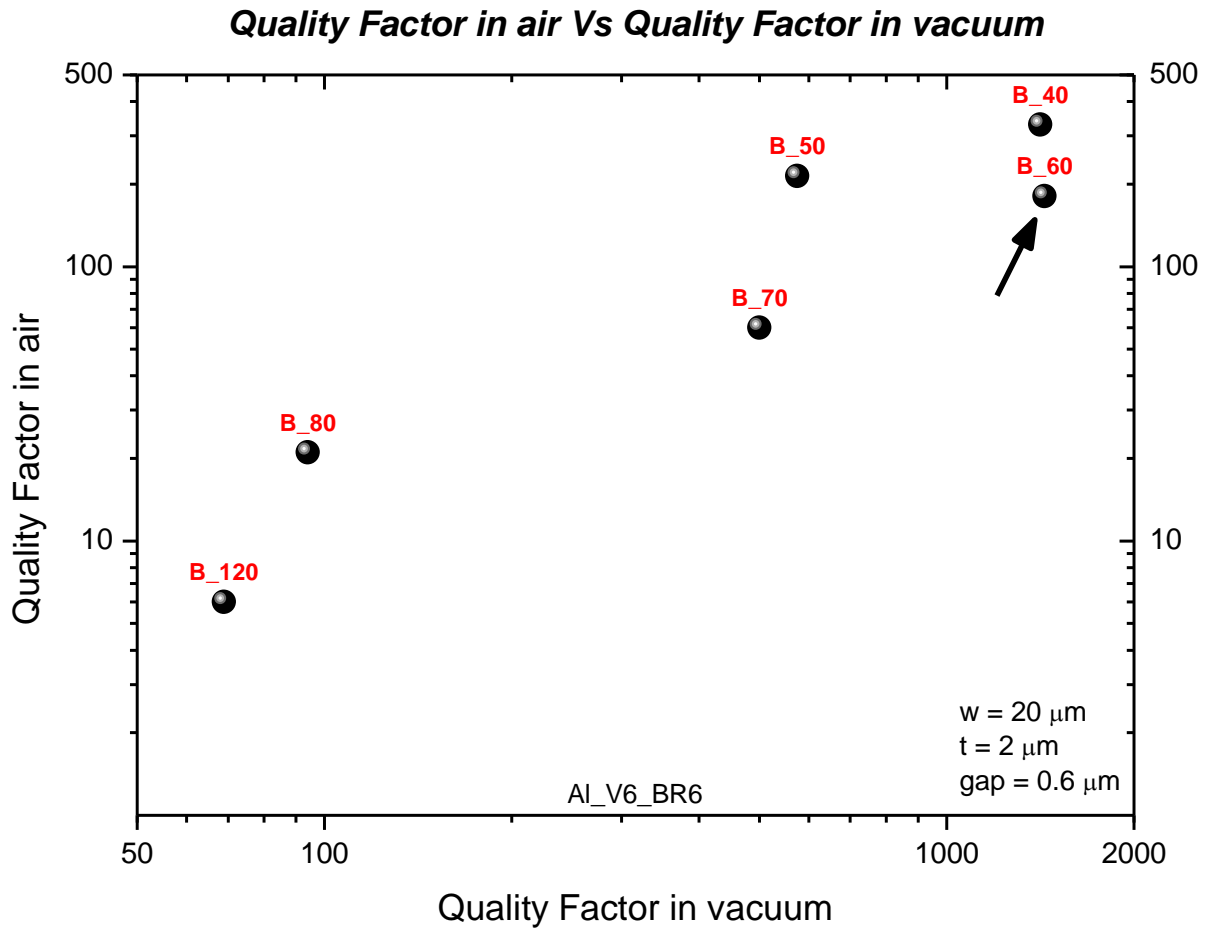
Graphic 25 - Quality Factors measured in atmospheric pressure as a function of their Resonance Frequency

An interesting result appears, showing that despite their Q-factor values in vacuum, those values in air appear to depend on the length of the structures, as longer structures with lower frequency peaks present lower Q-factors in air and shorter structures with higher frequency peaks maintain their Q-factors in higher values.

For example, the 60 μm bridge has an intrinsic Q-factor higher than the 40 μm and 50 μm bridges. That changes when the structures are exposed to atmospheric pressure, since the Q-factor of the 60 μm bridge will be lower than the Q-factors in air of the 40 μm and 50 μm bridges, and the overall Q-factors will be consecutively higher as the length of the structures decreases, as it can be seen on Graphic 25.

If these results are confirmed, one could say that the Q-factor of a given structure in atmospheric pressure is not random, and it is possible to estimate their values from their intrinsic values, in vacuum. Also, it is once more clear that shorter structures are typically more advantageous in order to obtain higher Q-factors for different dissipative media. For future and different experiments it could be advantageous to fabricate longer structures, and these results could be important in order to achieve higher Q-factors in dissipative media for those structures.

Graphic 26 demonstrates the relation between the Q-factor of the structures measured in air and their intrinsic Q-factors.



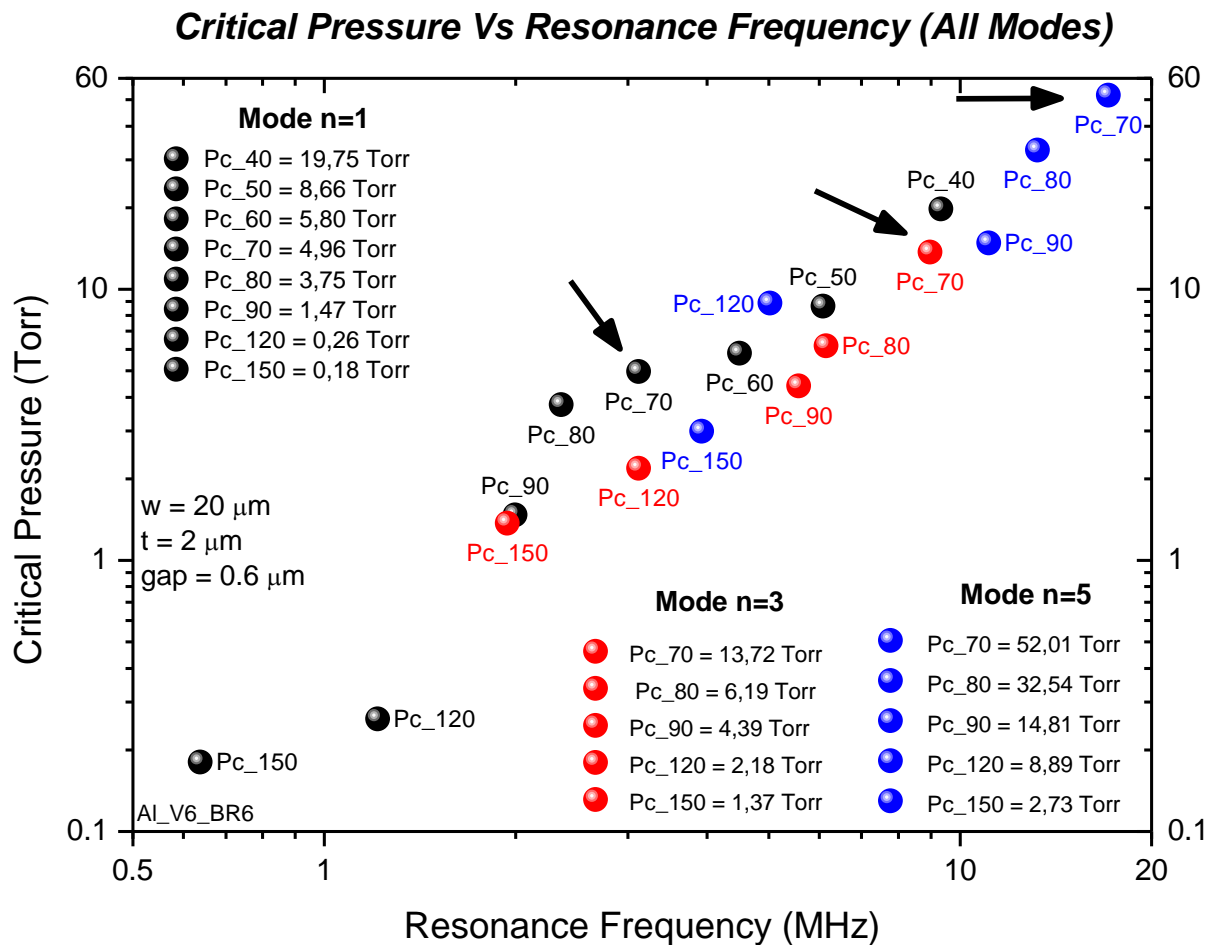
Graphic 26 - Quality Factors measured in air as a function of the Quality Factors measured in vacuum

This representation corroborates and visually demonstrates the results discussed above, where the 60 μm bridge (black arrow) has a higher Q-factor than the 40 μm and 50 μm bridges when measured in vacuum (vertical shift) but it will decrease to lower values than the two mentioned bridges when measured in an air environment (horizontal shift).

As we know from Equation 5, the Q-factors can be calculated by the sum of their energy losses.

For the case of the 60 μm bridge, it has smaller intrinsic dissipation than the 40 μm and 50 μm bridges, meaning it will have a higher Q-factor in vacuum. When the extrinsic contributions of the Q-factor are added, at atmospheric pressure, the total Q-factor of the 60 μm will be lower since it has higher extrinsic dissipation.

In Graphic 27 are shown the correspondent values of the critical pressures for the three measurable vibrational modes as a function of the resonance frequencies of each structure.



Graphic 27 - Critical Pressures as a function of the Resonance Frequency for all of the vibrational modes

By analyzing Graphic 27, it is visible that the shorter structures present higher P_C and the higher vibrational modes of the structures have higher values of P_C when compared to the fundamental mode. It is also clear that the F_{res} is a major factor in these measurements, since any given structures with similar F_{res} will have comparable values of P_C , regardless of the vibrational mode. For instance, a very long bridge actuated in a very high vibrational mode, will have similar F_{res} of a fundamental vibrational mode of a shorter structure, therefore their P_C will be close.

Despite the third and fifth vibrational modes of the 50, 40 and 60 μm bridges were unmeasurable, which will have theoretically higher P_C , it is possible to compare those pressures for the shorter structure where all of their modes were measurable, fundamental, third and fifth, which is the 70 μm bridge (black arrows).

For the fundamental mode the P_C of this bridge is 4.96 Torr, increasing to 13.72 Torr in the third mode, and reaching 52.01 Torr in the fifth mode. As opposed to that, the longer structure does not have such an abrupt increase of the P_C , as it can be seen for the 150 μm bridge, where the fundamental mode has a P_C of 0.18 Torr, the third vibrational mode of 1.37 Torr and the fifth vibrational mode of 2.73 Torr.

This makes sense because the F_{res} for the vibrational modes of a shorter structure are much close together than in a longer structure, when considering Equation 1 and how the vibrational modes are theoretically calculated.

One can conclude that the shorter the structure and the higher the vibrational mode, the critical pressure will be higher, meaning that the Q-factor of that supposed structure will only start to degrade at pressures much closer to atmospheric values, which will be an advantage either for measurements at atmospheric pressure and consequently for measurements in a fluidic dissipative media.

5.3. Squeeze Film Damping

The effect of surface forces such as the damping force of the surrounding air is considered negligible for machines with typical dimensions, but can play a significant role in micro sized devices. The importance of this effect becomes more evident as this devices decrease in their size, so it is safe to say that in a MEMS device, the motion of small parts can be significantly affected by the surrounding air, since that air presents itself as a counter reactive force on the moving of the plates [45].

When present, squeeze film damping is the type of fluid damping effect that has the most significant effect, which is caused by the squeezing of the fluid flow between the bridge and the fixed substrate [47].

For the case of two parallel plates as it can be seen on Figure 22, the resistive force of the bridge vibrating against the gate is caused by damping pressure between those two plates.

There are two components that characterize the damping pressure that are the component that causes the viscous flow of air when air is squeeze out of or sucked between the two plates, which is referred to as the viscous damping force, which dominates when the structure oscillates with a low frequency or vibrates at a low speed, meaning that the gas film in not totally compressed, and the one that causes compression of the air film, named elastic damping force that dominates when the structure vibrates at high frequencies or moves at high speeds, causing the gas film to be compressed but does not escape [45].

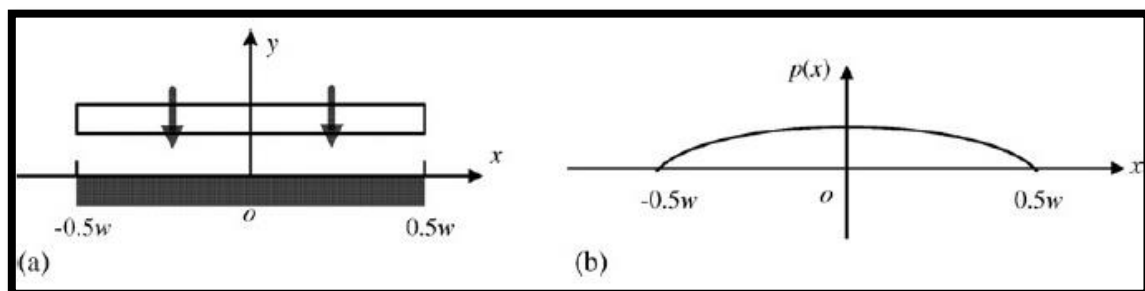


Figure 23 - Squeeze film air damping; a) cross-sectional view; b) the damping pressure [45]

For MEMS devices with moving plates against trapped films, squeeze film air damping becomes a problem, since that mechanism will dominate the damping which will consequently affect the systems frequency response [45].

The geometric specificities of the structures used for these tests, such as its length width or thickness will affect the presence or not of squeeze film damping, since large areas geometries will affect and induce shifts in the F_{res} of the structures, as it can be seen on [6], where there are shown measurements of several disks similar to Figure 3, with diameters ranging from 50 to 350 μm , where it is shown that for larger dimensions of the structures, the relative shift of the frequency of vibration will be higher.

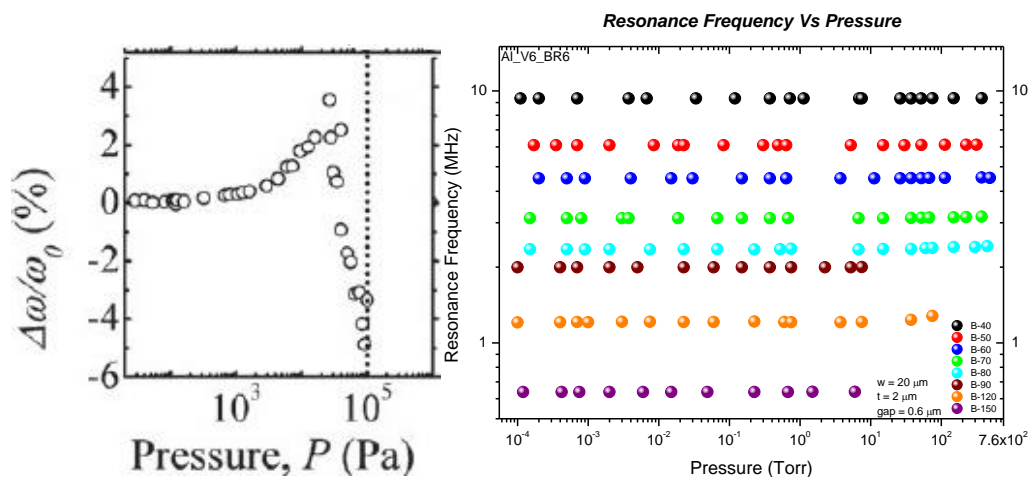
Also the reduction of the squeeze film thickness, meaning the layer of air trapped between the bridge and the gate, could affect this damping effect [6], since those gaps present in the measured structures are relatively small.

Another example from the same source [6] shows the shifts in the frequencies for different vibrational modes of a given structure, demonstrating the presence of squeeze film damping, more emphasized for lower vibrational modes.

In this source, it is shown that as the pressure increases there is an upward and a downward variation of the F_{res} , which results in mass loading on the plate. For lower pressures that mass effect becomes negligible inducing a convergence of the F_{res} to its intrinsic values. For this case, there is a visible increase of the F_{res} above its intrinsic value, which is associated with formation of a gas film that will act like a spring, adding stiffness to the plate [6].

With this information, and by analyzing the device discussed in Chapter 5.2, it is visible that there are no major shifts in the F_{res} of all of the structures, so one can conclude that for this case, the measured structures present no squeeze film damping.

Graphic 28 shows an example of a structure with squeeze film damping on the left, and it is clear that the structures measured in this experiment on the right (already represented in Graphic 23), do not follow the same behavior, thus confirming the previous conclusion.



Graphic 28 - Example of Resonance Frequency shifts as a function of Pressure with squeeze film damping [6] (left) and Resonance Frequency as a function of Pressure for the measured structures with no squeeze film damping (right)

Chapter 6 – MEMS Dissipation in water

6.1. Introduction

In order to be viable to operate MEMS as biological or chemical sensor, there is a need to create a means of *Fres* detection in a fluidic environment.

This is an extremely difficult detection in aqueous media since large energy dissipations lead to considerable degradation of the Q-factor of the structures in use, which consequently induce an increase of the minimum detectable mass needed to detect biological structures that require aqueous environments [1].

Despite MEMS devices are well studied in vacuum and air, when testing these structures in dissipative media such as water, some challenges and situations present themselves, like in the case of electrolysis and also electrode charge screening. These are problems that should be avoided due to the fact that they can cause bubbles on the structures, which can lead to defects or other type of damages to the systems [48].

Another common problem that can be encountered when using aqueous media is water-related stiction, which can occur during manufacturing, as well as during the operation of the device when in contact with the fluid used. If these MEMS devices are covered with thin oxide layers due to the lack of surface treatment, that surface will be hydrophilic which is susceptible to large water induced capillary forces that will act in the majority of the contact area [49].

With this information in mind, several devices containing various structures with different lengths were measured, using DI water as a dissipative media.

6.2. Experimental Setup

In order to measure the devices used in this work in a wet dissipative medium, the *Fres* of the structures was measured by submersing them in DI water. To do this, several modifications had to be made to the chip-chip carrier set.

As mentioned before the chips are connected to the chip carrier using Al wires, which have the function of conducting AC and DC voltages to the structures.

To enable the possibility of measurements in this medium, the wires must be protected to avoid the contact with the fluid. This can be done using an epoxy gel or, as it was used for these experiments, Elastosil E41, RTV-1 Silicone rubber, from Wacker Silicones.

This synthetic compound was applied using BD 3 ml syringes and 20 ga x 12 mm (LS20) Luer Stubs blunt needles, under an Olympus SZ-STB1 optical microscope. The protection of the wires with Silicone will also create a well that will maintain the drop of water on top of the device to be electrostatically actuated.

The DI water is applied using micropipettes, and its volume can range from 20 μ l to 50 μ l, depending on the shape of the Silicone well, which could have slightly higher walls, depending on the

amount of Silicone applied, since sometimes when this compound is applied on top of the Al wires it will not flow evenly between those wires leaving some of them exposed, forcing the user to apply extra amounts of Silicone to cover all of the exposed wires. When they are completely covered, the devices are left in air for some time, so the Silicone can have time to dry, thus protecting the wires.

Figure 23 shows de final aspect of some devices after the Silicone is applied and dried.

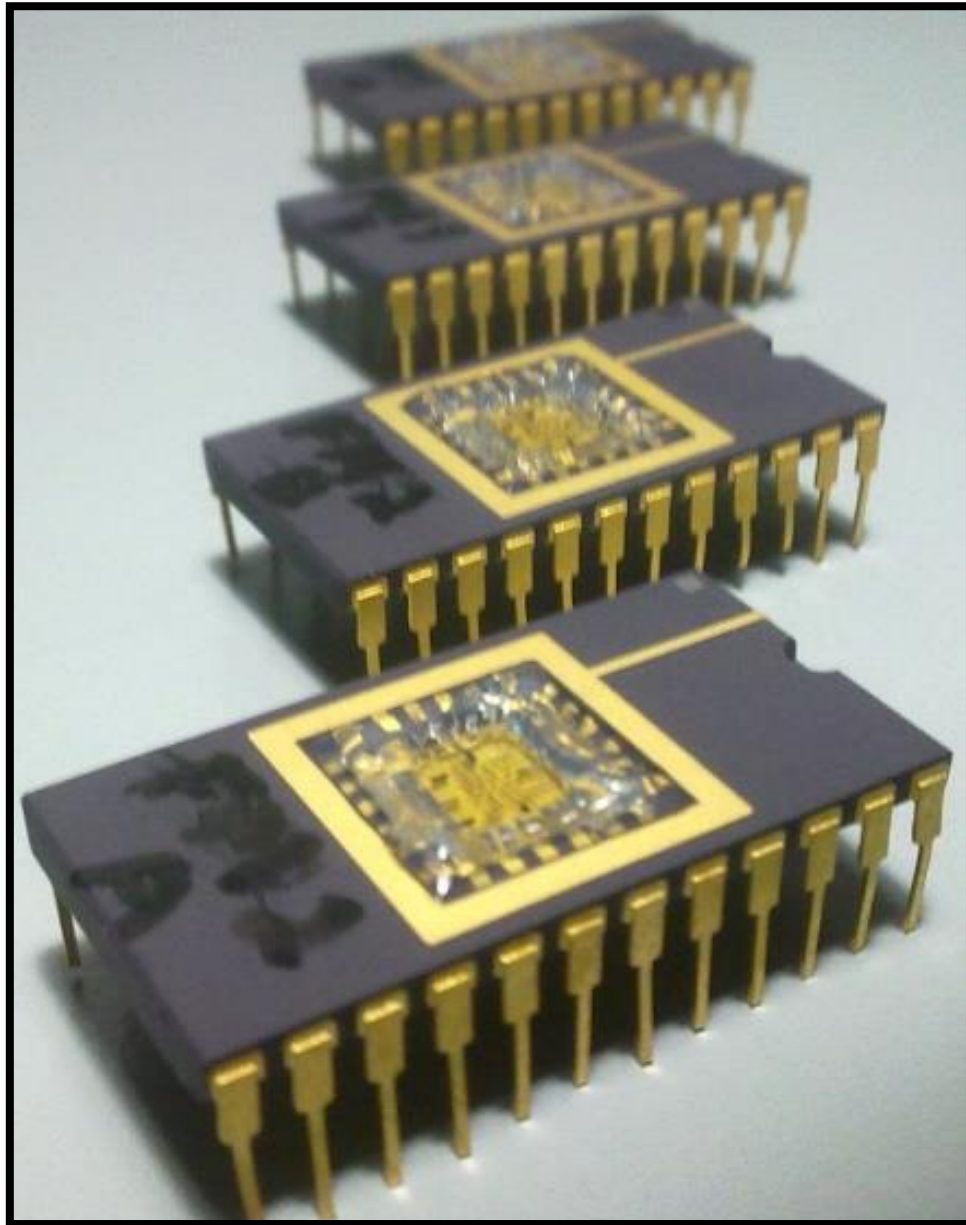


Figure 24 - Wire bonded devices protected with Silicone

After this step, the chip carrier is inserted in the socket of the vacuum chamber shown in Figure 17, the lid remains open and DI water is added. The idea is to measure the F_{res} of the structures the same way it is measured in vacuum and explained in Chapter 3.1, but in this case the laser goes through the DI water drop and then is deflected to the photodetector, demonstrated here on Figure 24.

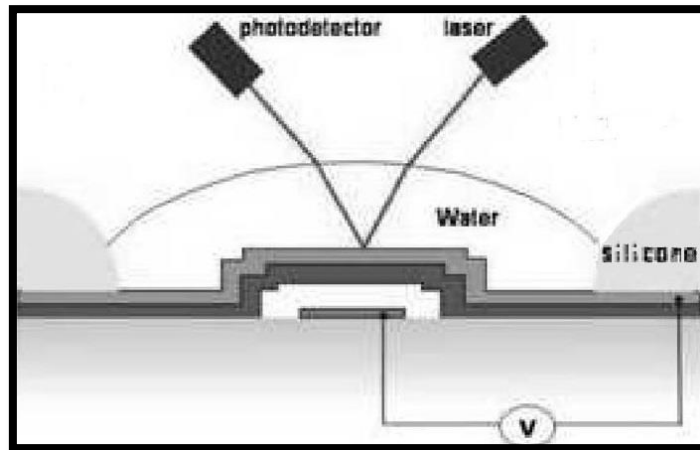


Figure 25 - Schematic illustration of the resonance frequency measurements in DI water [1]

In Figure 25 it is shown a real image of how a drop of DI water will stay imprisoned in the Silicone well, when the chip carrier is placed on the socket. The volume of water inserted will vary with the shape of the Silicon well and the die itself, or even to aid in the deflection of the laser beam to the photodetector.

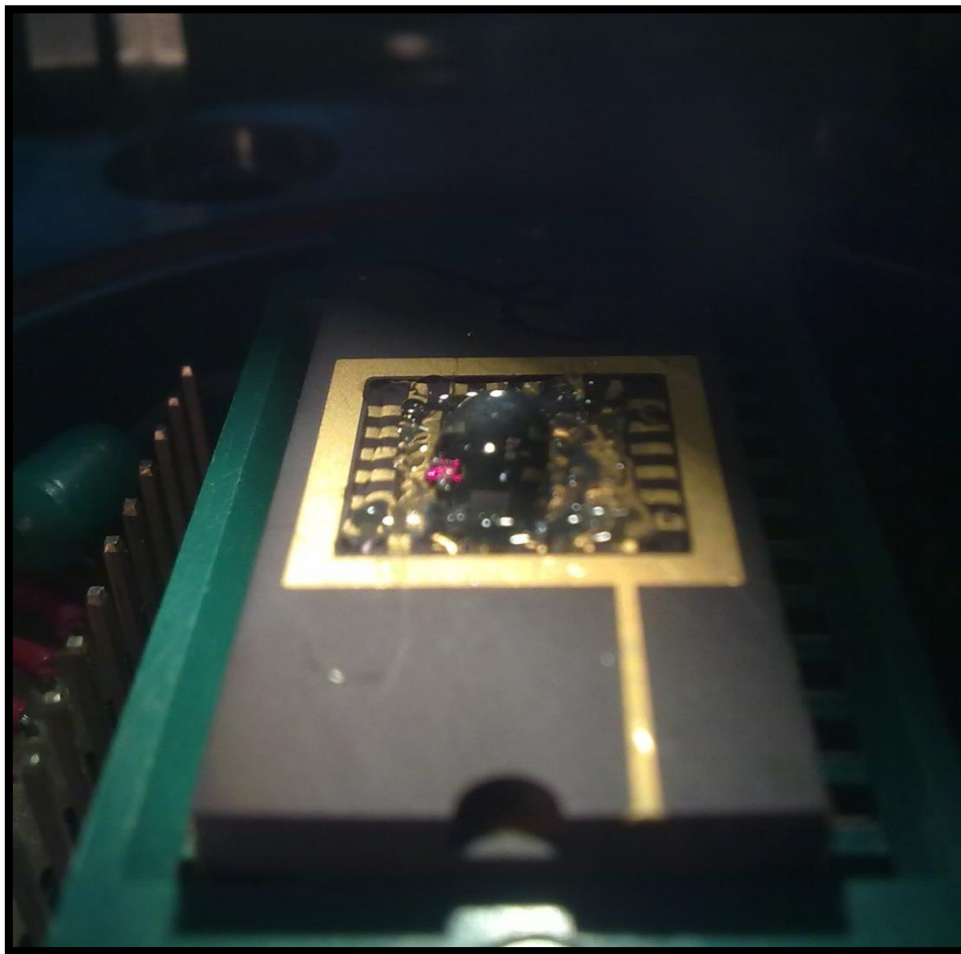


Figure 26 - DI water drop trapped on Silicone well

One of the problems that appeared when performing the deposition of Silicone in the devices that were used for the experiments discussed in Chapters 3, 4 and 5 was that in the masks used in their fabrication process, the main structures were too close to the extremities of the dies, *ergo* very close to the pads were the Al wires connect to the dies, as it can be seen on Figure 26.

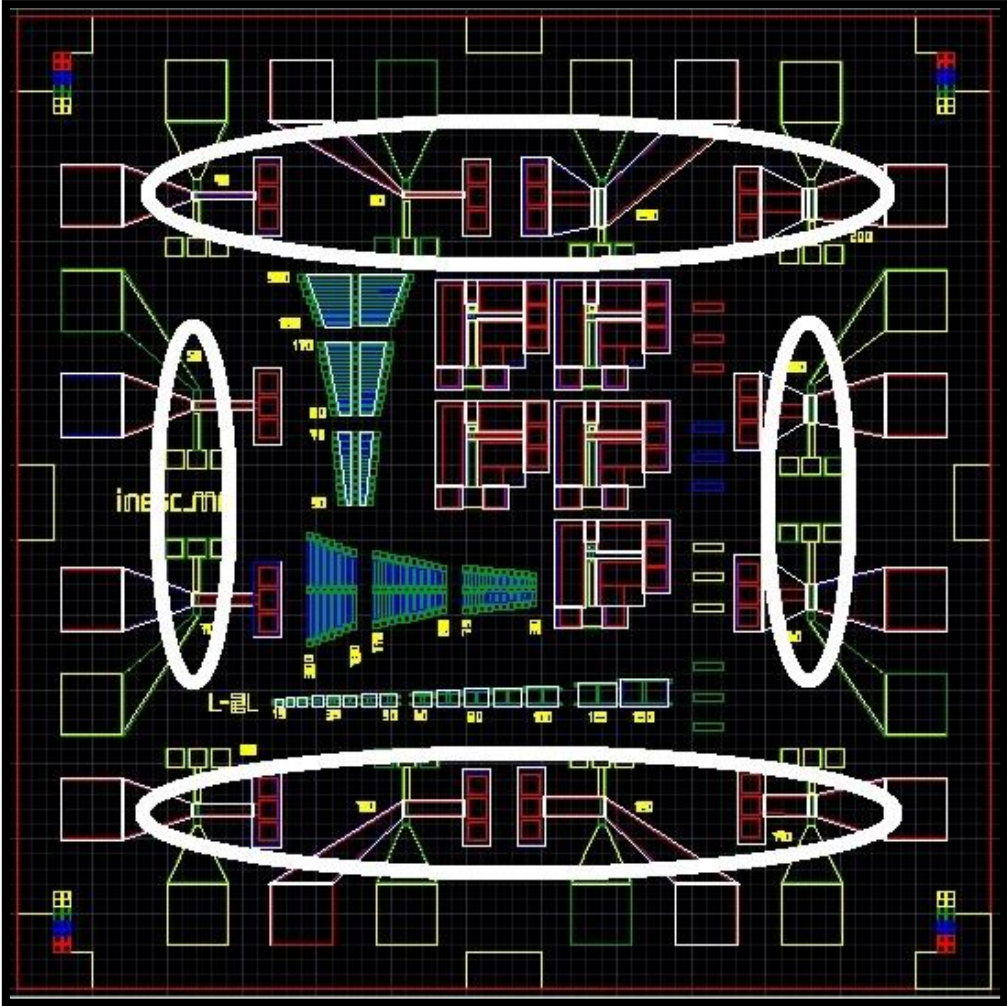


Figure 27 - Example of mask with the main structures close to the edges of the die

This means that when the Silicone is added to protect the wires, sometimes it flows on top of the structures.

This is a problem since if the amount of Silicone is too small, it would sit on top of the wires, and does not flow evenly to cover the entire length of the wires, and if is too much it covers the wires but continues to flow until it covers the structures itself, leaving the device unusable.

Even if the structures manage to stay free from being covered, another problem arises during the measurement.

Despite being transparent, the several layer of Silicone applied will deflect the laser beam when it is pointed to a given structure that is very close to the edge of this protective layer, meaning

that the photodetector becomes out of range from the laser deflection on the structure, as it can be seen on Figure 27.

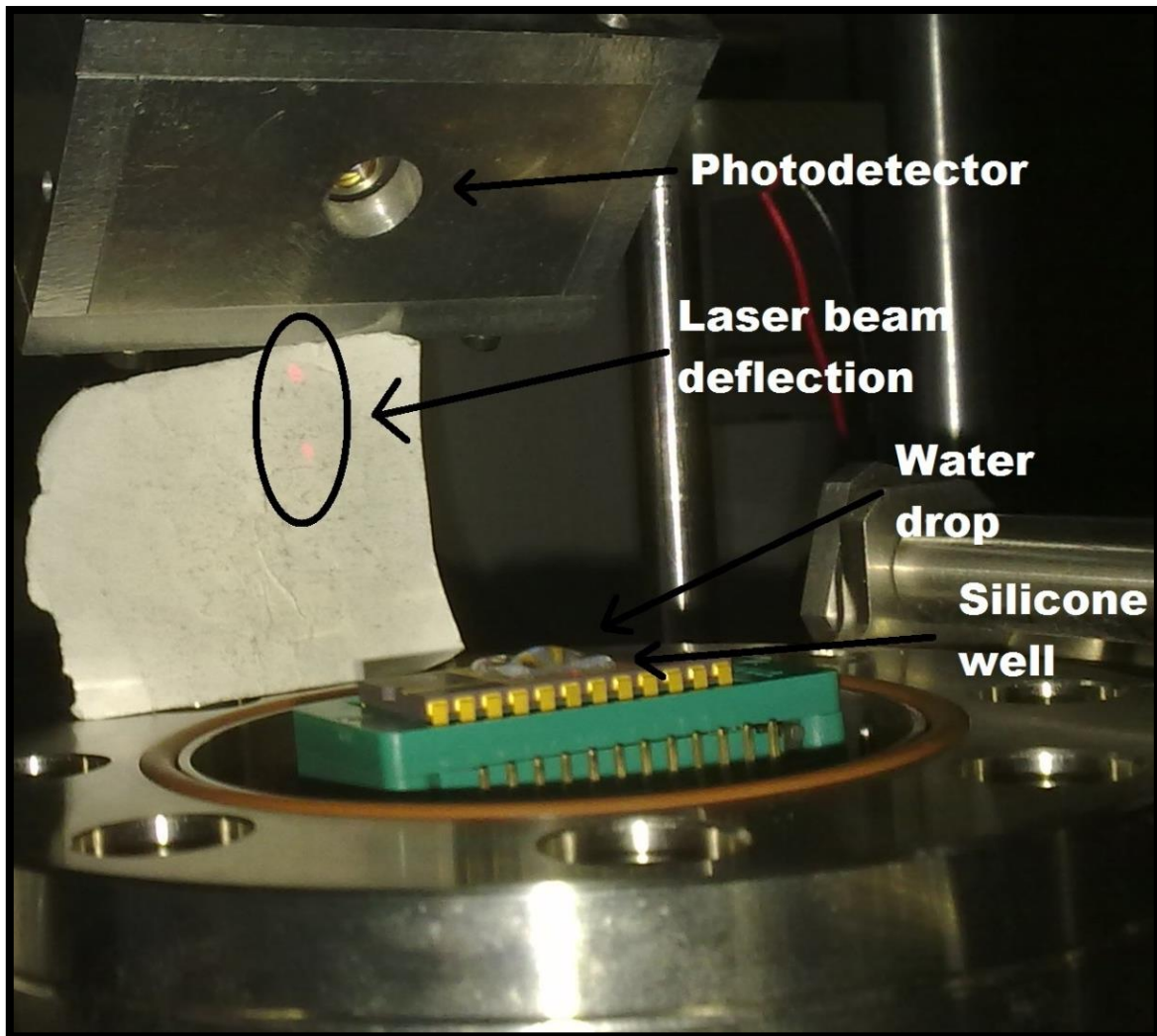


Figure 28 - Laser deflection due to proximity of the Silicone wall to the structures

Both the laser and the photodetector can be adjusted to ideal setups, depending on the positions of the structures that are being measured, but even in their maximum displacement some of the structures may continue to be unmeasurable.

This could be solve of course by dismounting the laser and photodetector, and removing their supports, replacing them by others that will provide an ideal setup for water measurements, but this would imply that those supports needed to be replace every time that typical vacuum measurements were necessary to perform.

Another solution was to design different masks that had the main structures closer to the center of the dies, as far away from the contact pads as possible.

With this in mind, the masks used to fabricate the devices demonstrated in the fabrication process of Chapter 2.1 were designed, as shown in Figure 28.

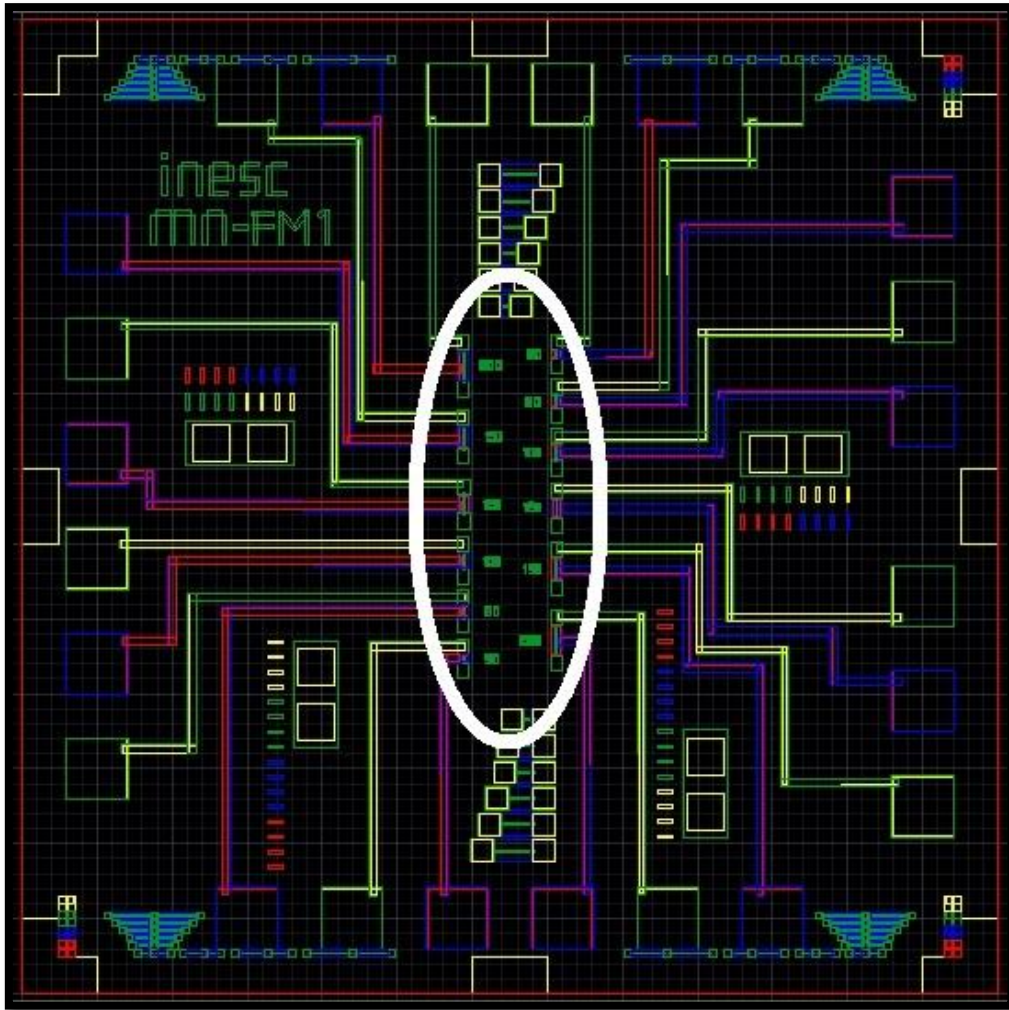


Figure 29 - Example of mask with the main structures closer to the center of the die

As mentioned before, these structures were electrostatically actuated. The voltages applied to them in an aqueous environment can be considered comparable to those requires for air or vacuum environments.

Typically, the most used values are 0.5 V of AC, and 1 V of DC voltages. Despite that, in some cases those voltages need to be increased to enable the visualization of a given frequency peak. The maximum values that they can reach are 1.26 V of AC and 5 V of DC. In the case of the DC voltages, if higher values are reached, electrolysis can be observed via bubble formation, which may lead to an irreversible mechanical damage of the structures.

By applying a given specific voltage in a certain structure in DI water and in air, the electrostatic force applied will be much higher in the first case, since the relative permittivity of the DI water is 100 times higher than in air.

Given that, the lower voltages applied in a structure submerged in DI water will be enough to actuate it, due to the higher magnitude of the electrostatic force in water. Also, higher voltages could be applied to the structures, if the electrodes were passivated with an insulator [1] [48].

At the end of the measurements, the devices need to be washed, to remove the DI water especially if different tests need to be done immediately.

In order to do this, the devices can be washed with IPA, then DI water and dried carefully with a compressed air gun [1].

This washing method worked for some of the devices used in this work, mainly the ones with a thickness of 2 μm and a gap of 0.6 μm , without destroying any structure.

That was not the case for the devices used here containing structures with a thickness of 0.9 μm and gaps of 1 μm . Since they are not so strong, this washing method proves to be destructive even when carefully controlling the compressed air gun, because the majority of the structures will be broken.

To prevent this, other methods can be used. For these experiments, the solution was to completely submerge the chip-chip carrier set on IPA for 2 minutes, with the DI water used for the measurements still on the chip, while slightly manually agitating with circular movements. Then, the devices were removed from the solution, and left naturally dry in air.

This procedure is a little longer, but the structures will remain unharmed. The edges of the chip carrier can be immediately dried carefully with cleaning paper. This washing method is viable since the surface tension of IPA is very close to the one from n-hexane, already discussed on Table 5, used for the release of the structures at the end of the microfabrication process, so the structures will remain intact.

One could also use the mentioned n-hexane to remove the DI water from the chip, by performing the same method discussed earlier, but adding the additional step of submerging the device on n-hexane after the submersion on IPA.

This will be a faster method, since this solution will evaporate quite fast, but unnecessary since it is an expensive solution and a considerable volume of it is needed to totally cover the chip and chip carrier, otherwise the wire bonding should be removed to extract the chip from the chip carrier in order to use a smaller amount of n-hexane. In conclusion, it is sufficient to use just IPA and let the devices dry in air, for structures that are more fragile.

6.3. Water Characterization

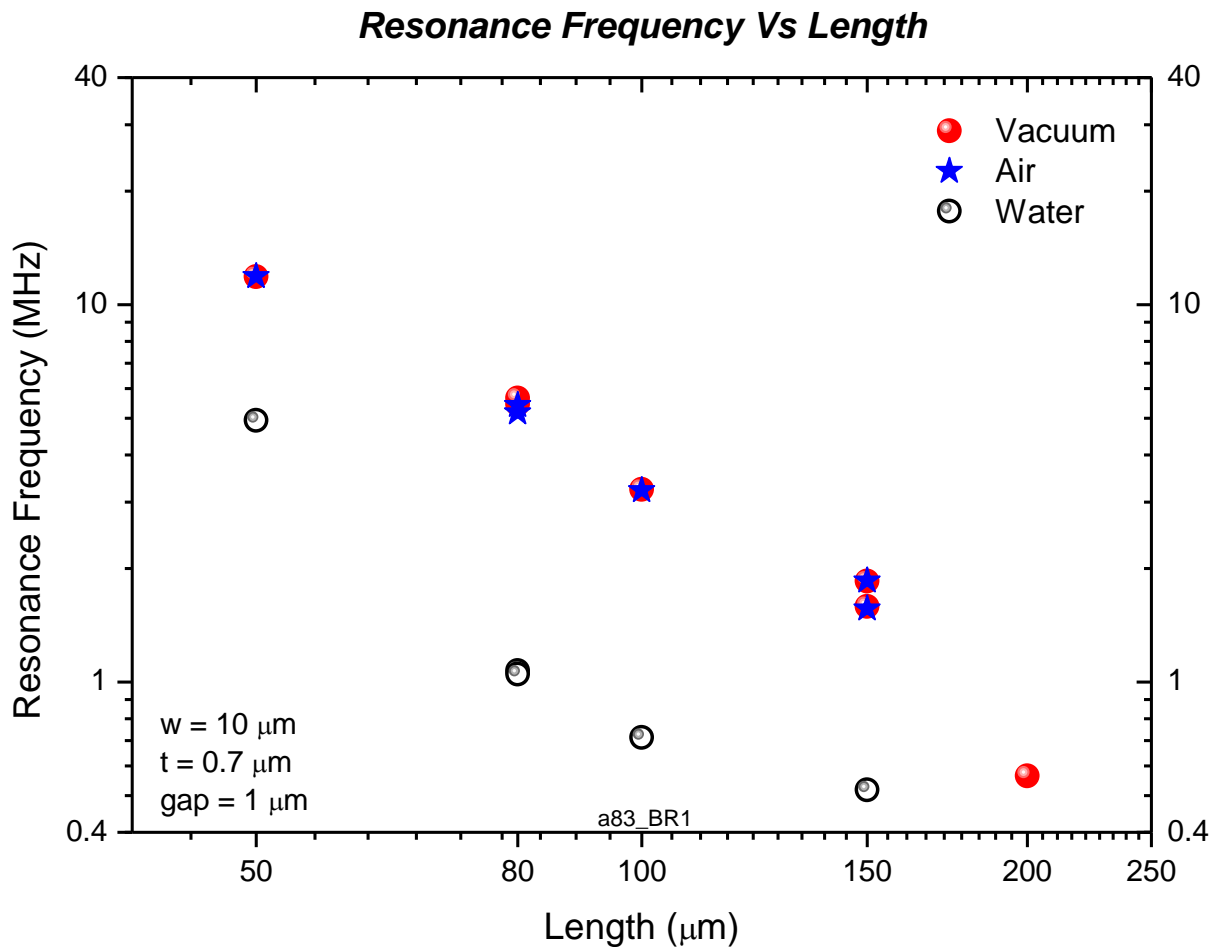
Several devices were measured under the conditions previously mentioned, using water as a dissipative medium.

It is important to mention that, due to the difficulty of measuring the resonance of MEMS structures in such medium, only in a few structures it was possible to extract valid information such as F_{res} or the respective Q-factors.

A previously fabricated device used for different experiments was made available to be the first one tested in a fluidic environment for this work, with bridge like structures that range from 50 μm to 200 μm in length, 10 μm of width, 0.7 μm of thickness, with a gap between the structures and the gates of 1 μm .

These structures were measured both in vacuum and in air, and then after going to the process discussed in Chapter 6.2, they were measured in a fluidic environment with DI water.

Graphic 29 shows the F_{res} of the measurable structures, when affected by the different dissipative media.



Graphic 29 - Resonance Frequency as a Function of the Length of the structures for the different dissipative media

The preliminary measurements shown in Graphic 29, demonstrate the F_{res} of some vibrational modes of the structures that were still in working conditions, measured in the different dissipative media.

This device was just quickly swept, to determine if operational structures were present, with no intent to assess different vibrational modes, in a random manner.

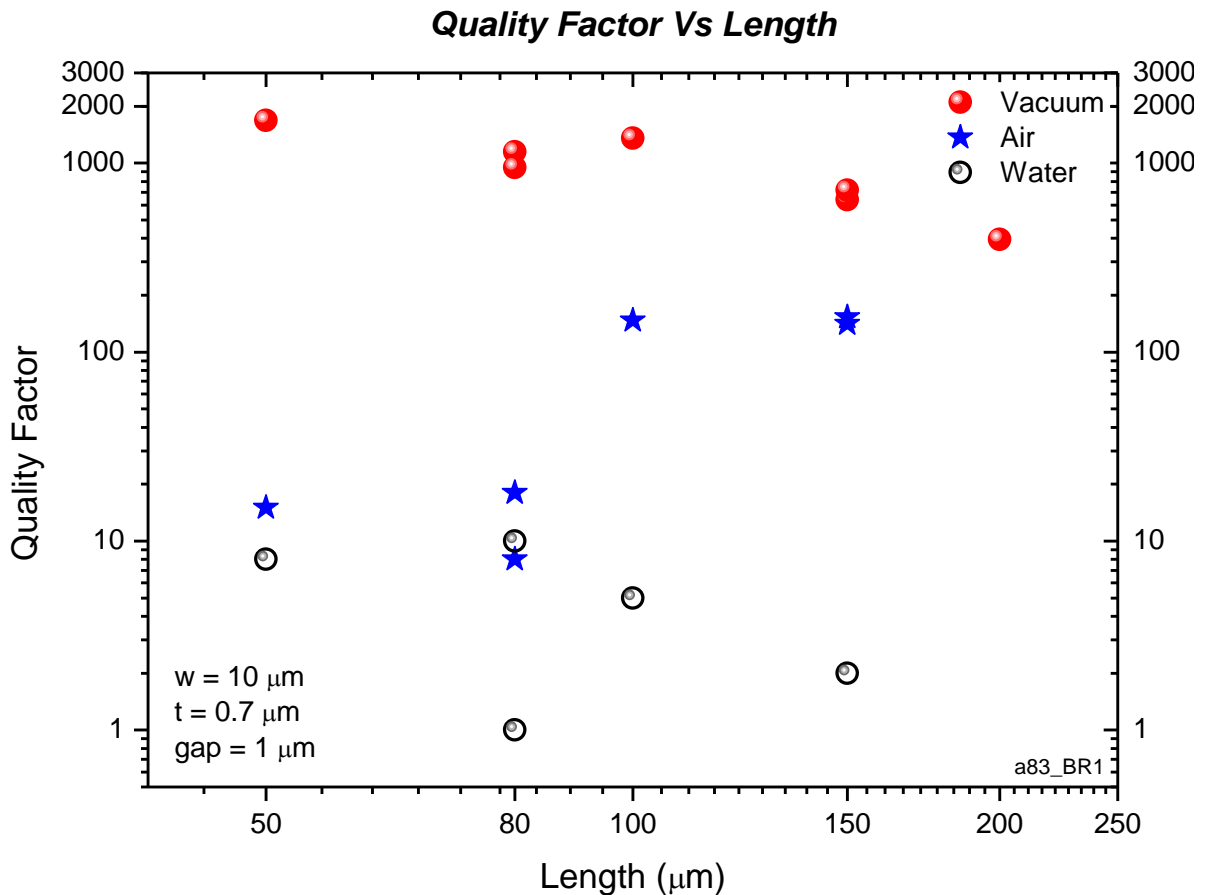
Due to that there is no possibility to compare, in the majority of the operating structures, if for example a given higher vibrational mode works better in DI water then a structure in a lower vibrational mode.

That is the reason why some structures were measured in a higher mode in vacuum, and then in a lower mode in water.

Since these structures present buckling, it is not possible to use Equation 1 to estimate the dependence of the F_{res} with the length. Several models are known to estimate those values, as it can be seen on [50] [51] [52] [53] [54].

It is visible that for the structures immersed in DI water, there is a shift of the F_{res} to lower values. That shift increases as the density of the fluid rises, and is relatively small when comparing the results in air and in vacuum [1] [48].

Since the density of water is much higher than the density of air, the shift is also higher, as it can be seen on Graphic 29.



Graphic 30 - Quality Factor as a Function of the Length of the structures for the different dissipative media

As the F_{res} shifts to lower values, so do the Q-factors of the structures decrease as the environment changes from vacuum, to air and then DI water.

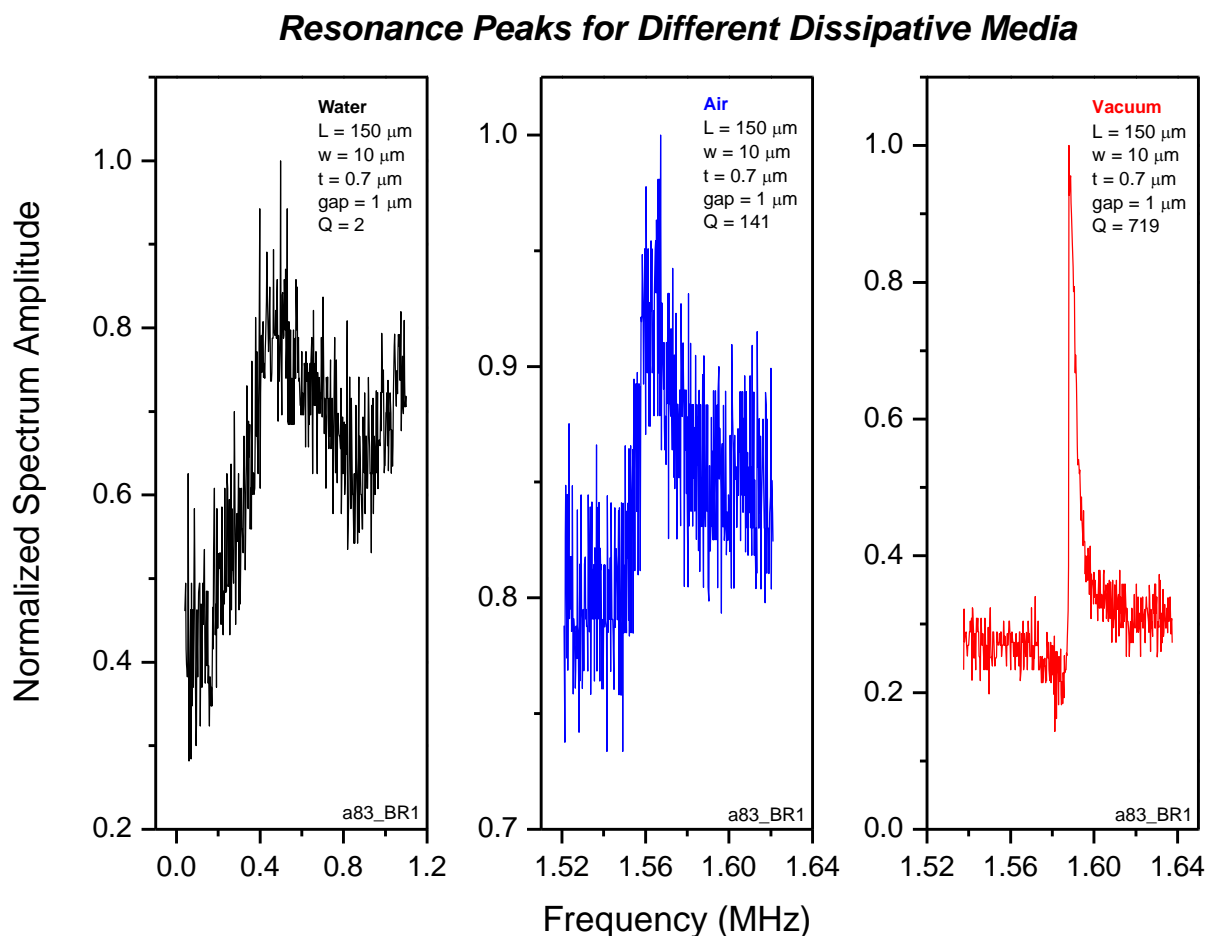
It is clear on Graphic 30 that there are three distinct levels of Q-factor separated due to the respective environment at which they were extracted.

The higher values represented as red dots are related to the Q-factors extracted in vacuum, and revolve around ≈ 1000 , and the higher value is $Q_{vacuum} = 1649$. The second level of Q-factors represented by the blue stars, are related to the measurements where the environment is air, and their values go around ≈ 100 , being the highest value $Q_{air} = 153$. For the lowest level of values represented by the hollow black dots, indicate the Q-factors of the structures when immersed in DI water, with values of ≈ 10 , where the highest value is 10.

For this particular set of structures, high values of voltages were used when measuring them in vacuum and air environments, mainly for the shorter ones, where DC voltages up to 60 V were applied, since the frequency peaks were unmeasurable at lower voltages. For the longer structures, voltages up to 10 V were used.

In the aqueous dissipative media, the voltage values used were the maximum values already discussed at the end of Chapter 6.2, 1.26 V of AC and 5 V of DC voltages.

In Graphic 31 it is demonstrated that for a particular structure, the way the F_{res} shifts to lower values when submitting it to different environments. As mentioned before, that shift is relatively small when compared with the values for the resonance peak in an aqueous environment.



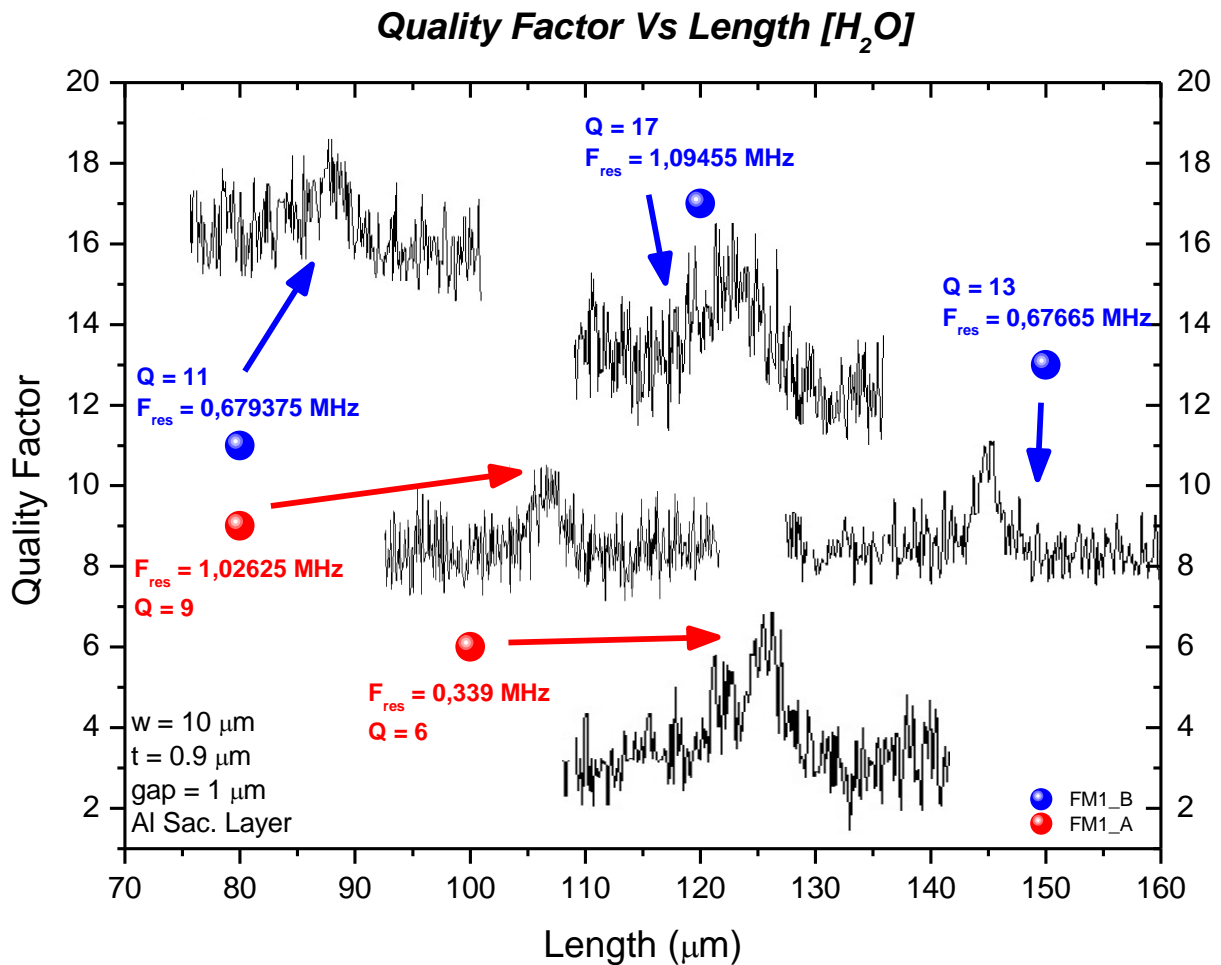
Graphic 31 - Representation of the Frequency peaks of a 150 μm bridge, at different dissipative media

Graphic 31 also confirms that beyond the shift of the F_{res} to lower values, The Q-factors of the 150 μm structure for the different media also decreases. Despite the shift of the F_{res} from vacuum to air is very small when compared to the shift in water, the Q-factor decreases significantly for every change in the environment, starting from $Q_{\text{vacuum}} = 719$ in vacuum, degrading to $Q_{\text{air}} = 141$ in air and being extremely low in water with a value of $Q_{\text{water}} = 2$.

The devices previously used for the voltage bias measurements, and fabricated using the mask from Figure 28 with the structures at the center, were also tested under a fluidic environment.

These measurements were merely focused on resonance peaks detection in water, so measurements in air were not performed, just in vacuum to validate if some of the structures were functional. The F_{res} of these structures in vacuum is represented in Graphic 4, also showing several vibrational modes for most of the bridges.

In Graphic 5 are represented their respective Q-factors in vacuum. The structures were then measured in an aqueous environment, along with another device from the same run, and their Q-factors were extracted as it can be seen on Graphic 32.



Graphic 32 - Representation of the Quality Factors as a function of the length of the structures, in an aqueous environment, with the correspondent frequency peaks

It is extremely hard to measure a given structure in this type of environment, as it was mentioned before.

For the results above, from the 24 available structures, combining the two devices from Graphic 32, 16 were operational at vacuum. From those, only 5 structures were measurable in this fluidic medium, two from one device and three from the other.

Their Q-factors in vacuum varied from ≈ 50 to ≈ 2000 , where the lowest value was $Q = 41$ and the highest $Q = 1981$. In DI water, those values decrease significantly, ranging from $Q \approx 2$ to $Q \approx 20$,

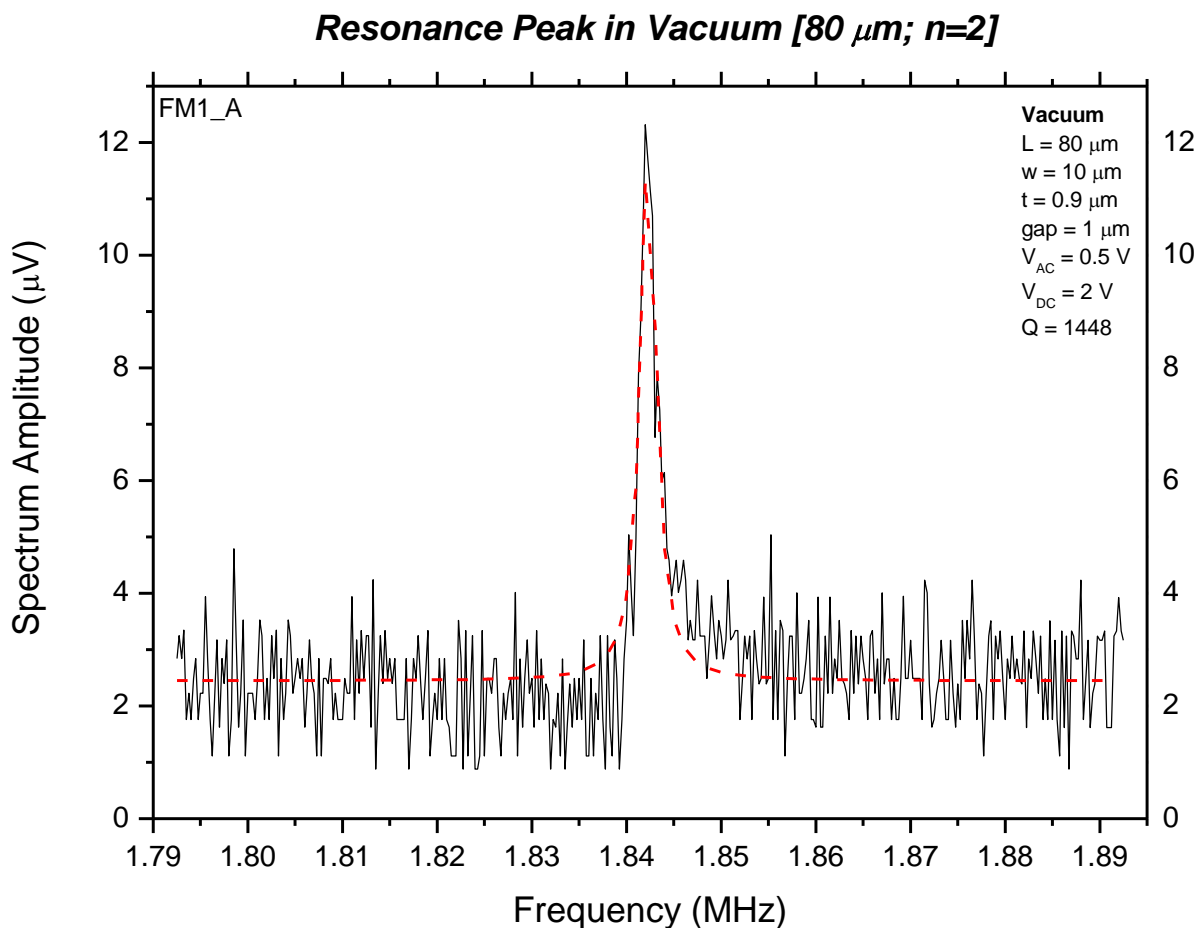
where the lowest value was $Q = 2$ and the highest $Q = 17$. This last value was the highest Q-factor achieved in this work, for the aqueous environment experiments.

The applied voltages were low as it was mentioned before for aqueous media. The applied AC voltages were $0.6 \text{ V} \leq AC \leq 1 \text{ V}$ and the applied DC voltages $0.5 \text{ V} \leq DC \leq 3 \text{ V}$.

The very low Q-factors extracted in this media imply that the FWHM of the resonance peaks are extremely high meaning that the peaks are quite wide.

As Graphic 33 demonstrates, for this specific structure in a vacuum environment, the resonance peak was extracted with a window range of $\approx 100 \text{ kHz}$, and the FWHM of the peak itself is quite narrow when compared with the window range, with a value of roughly 5 kHz . Practically speaking, this is a very straightforward peak to visualize, especially if it has large amplitude, $\approx 8 \mu\text{V}$ in this case.

With a frequency sweep of 1 MHz for instance and with the correct voltages, a very sharp peak will appear on the network analyzer, easily distinguishable.



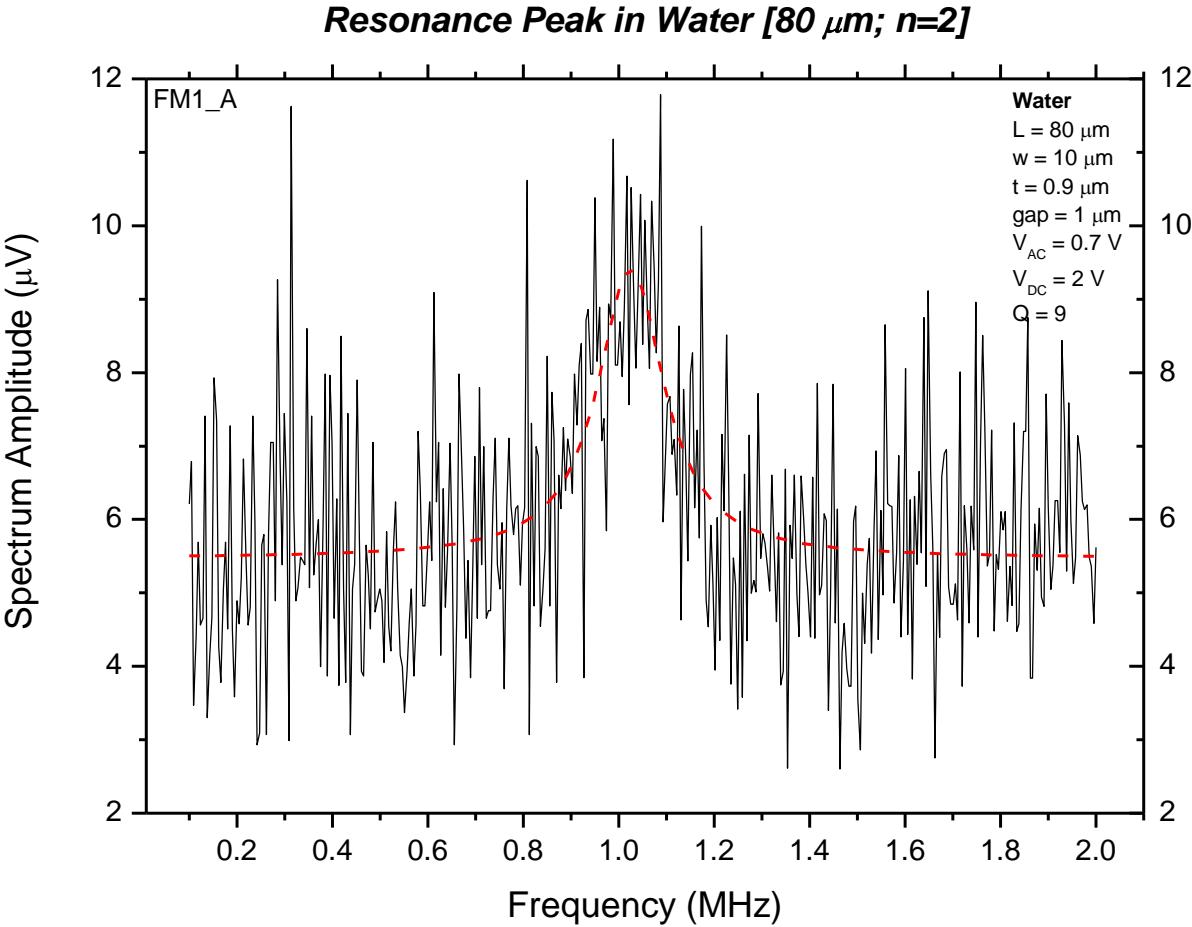
Graphic 33 - Representation of the Resonance Peak of an 80 μm bridge in Vacuum

Graphic 34 demonstrates the same structure, when measured immersed in DI water. The frequency window range is, in this case, $\approx 2 \text{ MHz}$, while the FWHM is $\approx 400 \text{ kHz}$, leading to a very low Q-factor value.

Both of these values are much higher when compared with the measurement in vacuum, along with the smaller amplitude of the peak, which is roughly half of the result in vacuum, $\approx 4\mu\text{V}$. All these facts make the visualization of a resonance peak in an aqueous environment very hard to visualize.

For instance, for the same frequency sweep of 1MHz, the resonance peak, if present, will be indistinguishable from all of the noise peaks, in the network analyzer.

By using the Equations 1 and 2, it is possible to estimate where the resonance peaks should be, but they can easily be mistaken by noise, or can be assumed that the structures are not operational.



Graphic 34 - Representation of the Resonance Peak of an 80 μm bridge in Water

Chapter 7 – Conclusion

7.1. Main Results

This work was done in collaboration with INESC-MN. It was focused on the operability of MEMS devices in liquid media. The first steps consisted on the vacuum characterization of several preexisting devices in order to gain some practice for further measurements. Later, several devices were also fabricated by the author of this work, consisting on hydrogenated amorphous silicon microbridges on glass substrates with lengths between 40 μm and 200 μm in length, at temperatures below 200 ° C.

Their resonance frequencies were optically detected and the correspondent quality factors were extracted, by fitting the resonance peaks to a Lorentzian curve. In these earlier measurements, the highest quality factor achieved was close to 3000. Higher vibrational modes were also measured and characterized.

Since MEMS resonator require the application of AC and DC voltages to be actuated, a voltage bias sweep procedure was performed to verify how different voltages can affect a given structure and to characterize their nonlinearities and mechanical or electrical effects. It was visible that different size structures can be affected by different effects, or even both on the same structure. In this work, most of the measured structures withstand DC voltages up to 30 V without any distortions in their resonance peaks.

The ability to improve the Q-factors of MEMS resonators by subjecting them to post-fabrication high temperatures was also tested. This much ignored Q-factor temperature dependence revealed very interesting and conclusive results in the author's opinion since all of the structures submitted to *annealing* improved their Q-factors regardless of their size, vibrational mode or intrinsic Q-factor, though some ideas and properties were left unconfirmed.

The highest Q-factor achieved in this experiment was $Q = 5715$. This increase is also definitive as it was discussed in Chapter 4.4 since the structures maintained the higher values achieved after the *annealing* experiment, for almost two months, when the last measurements were made. A possible threshold limit was also discussed at which the structures with Q-factor above that limit will increase much more, after an abrupt decrease at lower *annealing* temperatures.

The behavior of MEMS resonators at higher pressures from vacuum to atmospheric was also discussed. The structures are able to relatively maintain their resonance frequencies in the whole range of pressures, which means that they do not present squeeze film damping.

Regarding their Q-factors, they will go through free molecular and viscous flow regimes and their critical pressures where the Q-factors begin to degrade, were extracted, The highest critical point measured was $P_c = 52.01$ Torr and the highest Q-factor at atmospheric pressure was $Q = 490$. It became clear that the resonance frequency is extremely important, so it is useful to use shorter structures actuated at their higher vibrational modes, in order to have critical pressures very close to atmospheric values.

The devices were then measured in liquid media, using DI water. Some problems appeared as the preexisting devices were not prepared to be measured in water. The structures in those devices were too close to the edge of the dies, so when silicone was added to cover the wire bonding it flowed on top of the structures, destroying them.

So, the author designed new AutoCad masks where the structures were placed on the center of the dies, diminishing the amount of unmeasurable structures.

Despite the difficulty of extracting frequency peaks in this dissipative medium, some Q-factors were extracted. The highest value achieved was 17, for a 120 μm length bridge.

7.2. Future Perspectives

The next step of this work should aim to the integration of MEMS resonators with microfluidic systems for liquid detection since biomolecules thrive in these environments.

Simpler resonance frequency detection apparatus should also be discussed to decrease user errors due to equipment that was not initially designed for this type of measurements.

Another important step to make is the functionalization of the resonators surface to enable the detection of analyte biomolecules, to successfully fabricate a label-free detection device.

Appendix A

A. Runsheet Example

RunSheet – Bridges

Responsible: Guilherme Figueiredo

Sample ID: FM1

FM2

STEP 1: Substrate preparation

Date:

Operator: Guilherme Figueiredo

Machine: Wet Bench (Ultrasounds)

Conditions: Clean for 30 minutes in Alconox solution with ultrasounds+65°C;

Clean with DI water and blow dry with compressed air gun.

Number of Samples: 2.

STEP 2: Deposition in Nordiko 7000

Date:

Operator: Fernando Silva

Pre-Treatment: No

Material:

TiW – 1000 A

Recipe:

TiW 1000 A Low power

Conditions:

N = 10 sccm

Ar = 50 sccm

P (W) = 0.5 kW

Chamber pressure during deposition: P (Torr) = 3 mTorr

STEP 3: Litography DWL

Date:

Operator: José Bernardo/João Mouro

Pre-Treatment: Coating with Photoresist

Coater: 6/2

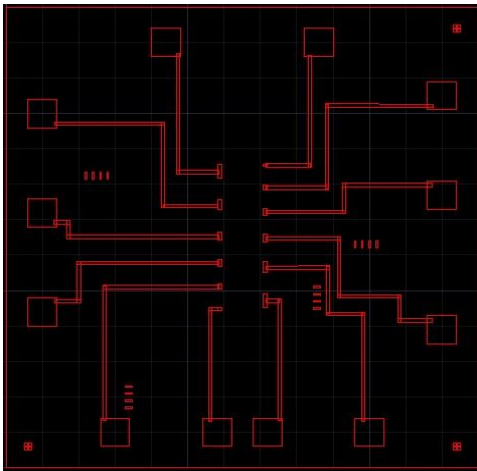
Exposing Conditions:

Map: BRES 6+6

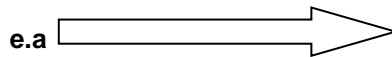
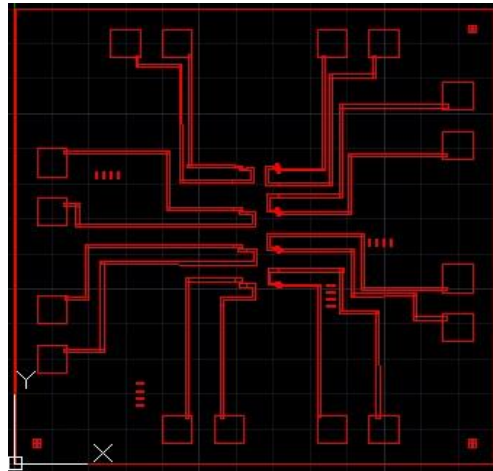
Die Dimensions: [X: 6500.000 Y: 6500.000] μm

Mask:

Directory: H2_FM1_gates



Directory: H2_FM2_gates



Exposing Coordinates (Set 0,0): [5000; 5500] from bottom left corner

Development: Recipe: 6/2

Observations:

1st Layer Mask

STEP 4: Etch LAM (RIE)

Date:

Operator: Virginia Soares/João Mouro

Conditions:

Max time 450 sec if TiW is not removed

Recipe:

SF₆ and CHF₃

Time:

250 sec

Observations:

Microstrip to remove Photoresist + wash with acetone and H₂O after etching

STEP 5: Deposition in Nordiko 7000

Date:

Operator: Fernando Silva/João Mouro

Material:

Al – 1 μm

Conditions:

Recipe: Al 1 μm

Ar = 50 sccm

P (W) = 2kW

P (Torr) = 3 mTorr

STEP 6: Litography DWL

Date:

Operator: José Bernardo/João Mouro

Pre-Treatment: Coating with Photoresist

Coater: 6/2

Exposing Conditions:

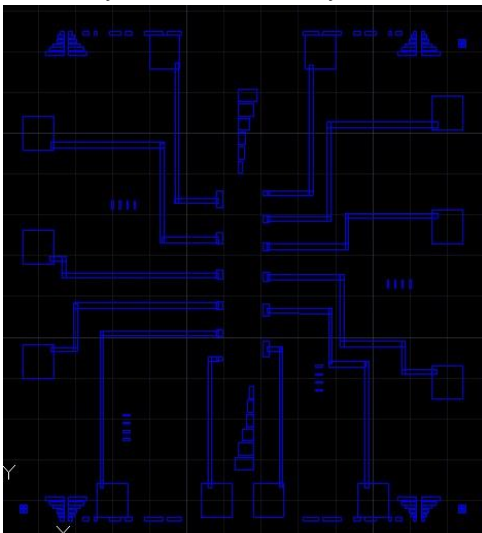
Map: BRES 6+6

Die Dimensions: [X: 6500.000 Y: 6500.000] μm

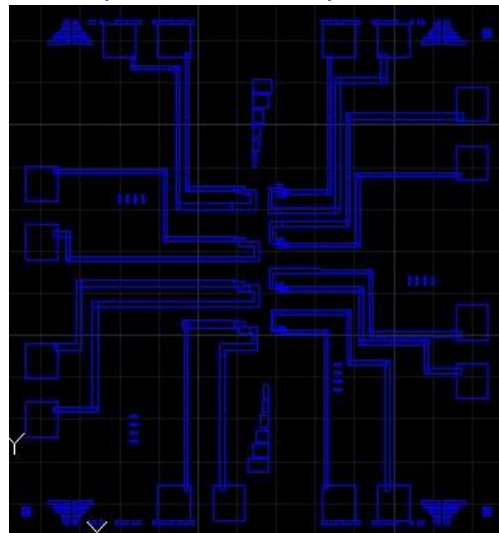
Alignment Marks: [X=300, Y=300; X=6200, Y=300] μm ; [X=6200, Y=6200] μm

Mask:

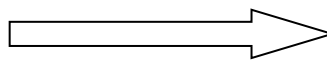
Directory: H2_FM1_sac_layer



Directory: H2_FM2_sac_layer



e.a



Development: Recipe: 6/2

Observations:

2nd Layer Mask

STEP 7: Etch (Wet etch)

Date:

Operator: Guilherme Figueiredo

Conditions:

Al etchant (Acid)

Development:

Time: 10-15min (visual inspection)

Observations:

- Change samples to H₂O (Tina); Dry with air gun
- Remove Photoresist with Microstrip; Wash with Acetone and H₂O; Dry

STEP 8: RF-PE-CVD Deposition

Date:

Operator: João Mouro

Pre-Treatment: No

Conditions:

Low stress n⁺ - a-Si:H (73% H₂)

P (Torr) = 0,5 Torr

P_{plasma} (W) = 25 W

T_{subs} = 175 °C

SiH₄ = 7 sccm

H₂ = 23 sccm

PH₃/H₂ = 35 sccm

Deposition Time (Structural Layer) = 1 hour

Observations:

Structural Layer:

Thickness: 0.9 μm

STEP 9: Deposition in Nordiko 7000 – TiW 1000 A

Date:

Operator: Fernando Silva

Pre-Treatment: No

Material:

TiW - 1000 A

Recipe:

TiW 1000 A Low power

Conditions:

N = 10 sccm

Ar = 50 sccm

P (W) = 0.5 kW

Chamber pressure during deposition: P (Torr) = 3 mTorr

STEP 10: Litography DWL

Date:

Operator: José Bernardo/João Mouro

Pre-Treatment: Coating with Photoresist

Coater: 6/2

Exposing Conditions:

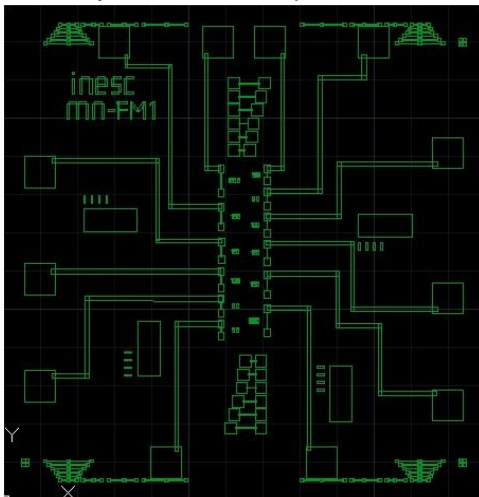
Map: BRES 6+6

Die Dimensions: [X: 6500.000 Y: 6500.000] μm

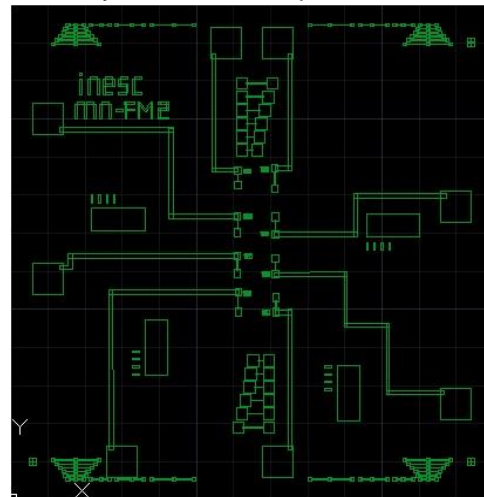
Alignment Marks: [X=300, Y=400; X=6200, Y=400] μm ; [X=6200, Y=6100] μm

Mask:

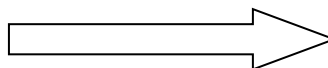
Directory: H2_FM1_BR_pads



Directory: H2_FM2_BR_pads



e.a



Development: Recipe: 6/2

Observations:

3rd Layer Mask

STEP 11: Etch LAM (RIE)**Date:****Operator:** Virginia Soares**Recipe:**SF₆ and CHF₃**Time:**

300 seconds; Max Time: 450 sec

Observations:

Two etch process were made, since the material was not totally removed;

First etch – 300 seconds; Seconds etch – 150 seconds;

Microstrip to remove Photoresist, wash with acetone and H₂O after etching.**STEP 12: Coating with Photoresist****Date:****Operator:** José Bernardo**Coater:** 6/2**Observations:**

This layer of Photoresist functions as a protective layer, so the structures will not be destroyed during the cutting.

STEP 13: Cut Dies**Date:****Operator:** Virginia Soares**Machine:**

Disco DAD 321

Recipe:

6.5 x 6.5 mm cuts (2 samples)

Observations:

2-3min in UV after cutting.

STEP 14: Wet Etch

Date:

Operator: Guilherme Figueiredo

Pre Treatment:

Remove Photoresist with Microstrip.

Wash with Acetone and Water.

Liquids:

Al etchant

Time: 3 hours

H₂O

Time: 3 min

IPA

Time: 3 min

n-Hexane

Time: 3 min



Decrease of the
Surface
Tension

Observations:

Removal of the sacrificial layer (Release of the structures).

Only release a few dies at the time (ex: 3 from each sample). If something goes wrong and the dies are lost, there are still several dies left to continue the work, instead of starting the microfabrication process again.

STEP 15: Wire Bonding

Date:

Operator: Fernando Silva

Observations:

Process Time: _____ days

Bibliography

- [1] T. Adrega, V. Chu and J. P. Conde, "Resonance of electrostatically actuated thin-film amorphous silicon microelectromechanical systems microresonators in aqueous solutions: Effect of solution conductivity and viscosity," *Journal of Applied Physics*, 2007.
- [2] E. Timurdogan, B. E. Alaca, I. H. Kavakli and H. Urey, "MEMS biosensor for detection of Hepatitis A and C viruses in serum, Biosensors and Bioelectronics," *Biosensors and Bioelectronics*, pp. 189-194, 2011.
- [3] K. M. Hansen and T. Thundat, "Microcantilever biosensors," *Methods*, pp. 57-64, 2005.
- [4] B. Bhushan, Springer Handbook of Nanotechnology, 1st ed., Springer, 2004.
- [5] T. Hsu, MEMS and Microsystems, 2nd ed., Wiley, 2008.
- [6] A. Gualdino, V. Chu and J. P. Conde, "Pressure effects on the dynamic properties of hydrogenated amorphous silicon disk resonators," *Journal of Micromechanics and Microengineering*, vol. 22, 2012.
- [7] J. Gaspar, V. Chu and J. P. Conde, "Amorphous silicon electrostatic microresonators with high quality factors," vol. 84, no. 4, 2004.
- [8] N. Maluf, An Introduction to Microelectromechanical Systems Engineering, 1st ed., Artech House, 2000.
- [9] J. W. Judy, "Microelectromechanical systems (MEMS): fabrication, design and Applications," vol. 10, pp. 1115-1134, 2001.
- [10] M. Younis, MEMS Linear and Nonlinear Statics and Dynamics, 1st ed., Springer, 2011.
- [11] V. P. Adiga, R. D. Alba, I. R. Storch, P. A. Yu, B. Ilic, R. A. Barton, S. Lee, J. Hone, P. L. McEuen, J. M. Parpia and H. G. Craighead, "Simultaneous electrical and optical readout of graphene-coated high Q silicon nitride resonators," vol. 103, 2013.
- [12] J. Mouro, A. Gualdino, V. Chu, Senior Member, IEEE and J. P. Conde, "Tunable Properties of Hydrogenated Amorphous/Nanocrystalline Silicon Thin-Films for Enhanced MEMS Resonators Performance," vol. 23, no. 3, 2014.
- [13] S. M. Spearing, "Materials Issues in Microelectromechanical Systems (MEMS)," Acta mater, 2000.
- [14] N. Maluf and K. Williams, An Introduction to Microelectromechanical Systems Engineering, 2nd ed., Artech House, 2004.
- [15] R. A. Street, "Amorphous Silicon Electronics," *MRS Bulletin*, vol. 17, no. 11, pp. 70-76, 1992.
- [16] W. S. Wong, S. E. Ready, J.-P. Lu and R. A. Street, "Hydrogenated Amorphous Silicon Thin-Film Transistor Arrays Fabricated by Digital Lithography," vol. 24, no. 9, 2003.
- [17] R. A. Street, Hydrogenated Amorphous Silicon, 1st ed., Cambridge University Press, 1991.
- [18] J. Gaspar, V. Chu, Member, IEEE and J. P. Conde, "Electrostatic Microresonators From Doped Hydrogenated Amorphous and Nanocrystalline Silicon Thin Films," *Journal of Microelectromechanical Systems*, vol. 14, no. 5, 2005.
- [19] W. H. Ko, "Trends and frontiers of MEMS," *Sensors and Actuators A*, vol. 136, pp. 62-67, 2007.
- [20] J. Mouro, A. Gualdino, V. Chu and J. P. Conde, "Microstructure factor and mechanical and electronic properties of hydrogenated amorphous and nanocrystalline silicon thin-films for microelectromechanical systems applications," *Journal of Applied Physics*, vol. 114, no. 184905, 2013.
- [21] S. B. Patil, V. Chu and J. P. Conde, "Mass Sensing using an Amorphous Silicon MEMS resonator," *Procedia Chemistry*, vol. 1, pp. 1063-1066, 2009.

- [22] J. Lu, T. Ikehara, Y. Zhang, T. Mihara, T. Itoh and R. Maeda, "High Quality Factor Silicon Cantilever Driven by PZT Actuator for Resonant Based Mass Detection," in *DTIP of MEMS and MOEMS*, 9-11 April, 2008.
- [23] M. A. Hopcroft, B. Kim, S. Chandorkar, R. Melamud, M. Agarwal, C. M. Jha, G. Bahl, J. Salvia, H. Mehta, H. K. Lee, R. N. Candler and T. W. Kenny, "Using the temperature dependence of resonator quality factor as a thermometer," *Applied Physics Letters*, vol. 91, 2007.
- [24] G. Q. Wu, D. H. Xu, B. Xiong and Y. L. Wang, "Effect of air damping on quality factor of bulk mode microresonators, Microelectronic Engineering," *Microelectronic Engineering*, vol. 103, pp. 86-91, 2012.
- [25] G. De Pasquale and A. Som, "Dynamic identification of electrostatically actuated MEMS in the frequency domain," *Mechanical Systems and Signal Processing*, vol. 24, pp. 1621-1633, 2010.
- [26] C. Rembe, R. Kant and R. S. Muller, "Optical Measurement Methods to Study Dynamic Behavior in MEMS," Berkeley.
- [27] P. Krehl, S. Engemann, C. Rembe and E. P. Hofer, "High-speed visualization, a powerful diagnostic tool for microactuators - retrospect and prospect," *Microsystem Technologies*, vol. 5, pp. 113-132.
- [28] J. P. Zhao, H. L. Chen, J. M. Huang and A. Q. Liu, "A study of dynamic characteristics and simulation of MEMS torsional micromirrors," *Sensors and Actuators A*, vol. 120, pp. 199-210, 2004.
- [29] H. M. Quakad and M. I. Younis, "The dynamic behavior of MEMS arch resonators actuated electrically," *International Journal of Non-Linear Mechanics*, vol. 45, pp. 704-713, 2010.
- [30] S. Ghionea, D. Hull and K. Williams, "Characterization techniques for a MEMS electric-field sensor in vacuum," *Journal of Electrostatics*, vol. 71, pp. 1076-1082, 2013.
- [31] J. Gaspar, V. Chu and J. P. Conde, "Electrostatically actuated thin-film amorphous silicon microbridge resonators," *Journal of Applied Physics*, vol. 97, 2005.
- [32] J. Gaspar, V. Chu and J. P. Conde, "High-Q thin-film silicon resonators processed at temperatures below 110°C on glass and plastic substrates," in *17th IEEE International Conference on MEMS*, 2004.
- [33] D. K. Agrawal, J. Woodhouse, A. A. Seshia, Member and IEEE, "Modeling Nonlinearities in MEMS Oscillators," *IEEE Transactions on Ultrasonics, Ferroelectrics and Frequency Control*, vol. 60, no. 8, 2013.
- [34] M. Agarwal, K. K. Park, R. N. Candler, B. Kim, M. A. Hopcroft, S. A. Chandorkar, C. M. Jha, T. W. Kenny and B. Murmann, "Nonlinear Characterization of Electrostatic MEMS Resonators," Stanford, California, USA, 2006.
- [35] K. Bongsang, Member, IEEE, M. A. Hopcroft, R. N. Candler, Member, IEEE, C. M. Jha, Student Member, ASME, M. Agarwal, Member, IEEE, R. Melamud, S. A. Chandorkar, G. Yama and T. W. Kenny, "Temperature Dependence of Quality Factor in MEMS Resonators," *Journal of Microelectromechanical Systems*, vol. 17, no. 3, 2008.
- [36] M. A. Hopcroft, R. Melamud, R. N. Candler, W.-T. Park, B. Kim, G. Yama, A. Partridge, M. Lutz and T. W. Kenny, "Active temperature compensation for micromachined resonators," in *Solid-State Sensor, Actuator and Microsystems Workshop*, Hilton Head Island, South Carolina, 2004.
- [37] M. J. Ahamed, D. Senkal and A. M. Shkel, "Effect of Annealing on Mechanical Quality Factor of Fused Quartz Hemispherical Resonator," Irvine, CA, USA, 2014.
- [38] V. P. Mitrofanov and K. V. Tokmakov, "Effect of heating on dissipation of mechanical energy in fused silica fibers," *Physics Letters A*, no. 308, pp. 212-218, 2003.
- [39] K. Bongsang, R. N. Candler, M. A. Hopcroft, M. Agarwal, W.-T. Park and T. W. Kenny, "Frequency stability of wafer-scale film encapsulated silicon based MEMS resonators," *Sensors and Actuators A*, vol. 136, pp. 125-131, 2007.

- [40] T. O. Rocheleau, T. L. Naing and C. T.-C. Nguyen, "Long-Term Stability of a Hermetically Packaged MEMS Disk Oscillator," IEEE, Berkeley, USA, 2013.
- [41] A. Neels, G. Bourban, H. Shea, A. Schifferle, E. Mazza and A. Dommann, "Aging of MEMS - Correlation of Mechanical and Structural Properties," in *Euroensors XXIII Conference*, Lausanne, Switzerland, 2009.
- [42] M. Imboden, O. A. Williams and P. Mohanty, "Observation of Nonlinear Dissipation in Piezoresistive Diamond Nanomechanical Resonators by Heterodyne Down-Mixing," *Nano Letters*, vol. 13, pp. 4014-4019, 2013.
- [43] H. Hosaka, K. Itao and S. Kuroda, "Damping characteristics of beam-shaped micro-oscillators," *Sensors and Actuators A*, vol. 49, pp. 87-95, 1995.
- [44] S. Gorelick, J. R. Dekker, M. Leivo and U. Kantojärvi, "Air Damping of Oscillating MEMS Structures: Modeling and Comparison with Experiment," in *COMSOL Conference*, Rotterdam, 2012.
- [45] M. Bao and H. Yang, "Squeeze film air damping in MEMS," *Sensors and Actuators A*, vol. 136, pp. 3-27, 2007.
- [46] L. Dong, B. Liu, H. Yan, X. Wang and L. Sun, "The Effects of Air Damping on MEMS Wine-Glass Resonator," *Integrated Ferroelectrics: An International Journal*, vol. 137, no. 1, pp. 37-45, 2012.
- [47] A. K. Pandey, R. Pratap and F. S. Chau, "Effect of Pressure on Fluid Damping in MEMS Torsional Resonators with Flow Ranging from Continuum to Molecular Regime," *Experimental Mechanics*, vol. 48, pp. 91-106, 2008.
- [48] T. Adrega, V. Chu and J. P. Conde, "Electrostatically actuated resonance of amorphous silicon microresonators in water," *Applied Physics Letters*, vol. 89, 2006.
- [49] M. Scherge, X. Li and J. A. Schaefer, "The effect of water on friction of MEMS," *Tribology Letters*, vol. 6, pp. 215-220, 1998.
- [50] G.-F. Wang and X.-Q. Feng, "Timoshenko beam model for buckling and vibration of nanowires with surface effects," *Journal of Physics D: Applied Physics*, vol. 42, no. -, p. 5, 2009.
- [51] D. R. Southworth, L. M. Bellan, Y. Linzon, H. G. Craighead and J. M. Parpia, "Stress-based vapor sensing using resonant microbridges," *Applied Physics Letters*, vol. 96, 2010.
- [52] A. H. Nayfeh and S. A. Emam, "Exact solution and stability of postbuckling configurations of beams," *Nonlinear Dyn*, vol. 54, pp. 395-408, 2008.
- [53] A. H. Nayfeh, W. Kreider and T. J. Anderson, "Investigation of Natural Frequencies and Mode Shapes of Buckled Beams," *AIAA Journal*, vol. 33, no. 6, pp. 1121-1126, 1995.
- [54] A. Bokaian, "Natural Frequencies of beams under compressive axial loads," *Journal of Sound and Vibration*, vol. 126, no. 1, pp. 49-65, 1988.